

KfK 3408
Oktober 1982

**Extraction of Eigenfrequencies,
Mode Shapes and
Critical Damping Ratios of
HDR Core Barrel Mockup from
Step Relaxation Response
Signals Measured in the
Snapback Test Series V59**

F. Eberle, J. Kadlec
Institut für Reaktorentwicklung

Kernforschungszentrum Karlsruhe

KERNFORSCHUNGSZENTRUM KARLSRUHE
Institut für Reaktorentwicklung

KFK 3408

Extraction of Eigenfrequencies, Mode Shapes and
Critical Damping Ratios of HDR Core Barrel Mockup
from Step Relaxation Response Signals
Measured in the Snapback Test Series V59

by

F. Eberle and J. Kadlec

Kernforschungszentrum Karlsruhe GmbH, Karlsruhe

Als Manuskript vervielfältigt
Für diesen Bericht behalten wir uns alle Rechte vor

Kernforschungszentrum Karlsruhe GmbH
ISSN 0303-4003

Summary

The report deals with the experimental analysis of the core barrel mockup installed in the reactor pressure vessel of the HDR-facility at Karlstein on the river Main. The eigenfrequencies, the mode shapes and the damping ratios of the core barrel were extracted from the set of simultaneously measured relaxation response signals. The response was achieved via a snapback process, e.g. sudden release of the core barrel previously loaded with a concentrated load by means of a hydraulic deflection device. For the extraction of modal characteristics from the transient acceleration and displacement signals the computer code EVA, especially developed for this purpose, was used.

A total number of 76 eigenmodes was identified - 32 eigenmodes of the core barrel/water charge coupled system and 44 eigenmodes of the core barrel without water charge. Several of these eigenmodes are multiple modes (preferably doublets) with equal axial and circumferential order but different eigenfrequencies, damping ratios and orientations in space. The smallest identified eigenfrequency difference of one doublet illustrating the good resolution capability of the procedure equals 1.5 %.

The procedure does not impose any restrictions on the nature of the transient excitation and, therefore can be used in such application tasks where conventional procedures of experimental modal analysis are not practicable, e.g. under hostile environmental conditions and in badly accessible systems. Experience acquired shows that the procedure can be well applied also in case of slightly non-linear systems.

The experimental setup used, the mathematical background of the computer code EVA as well as the results obtained are described in detail.

Extraktion der Eigenfrequenzen, der Eigenschwingungsformen und der Dämpfungsquotienten des HDR-Modellkernbehälters aus den abklingenden Sprungantwortsignalen der Snapback-Versuchsreihe V59

Zusammenfassung

Der Bericht befaßt sich mit der experimentellen Modalanalyse eines im Reaktordruckgefäß der HDR-Anlage in Karlstein am Main installierten Modellkernbehälters. Die Eigenfrequenzen, die Eigenschwingungsformen und die Dämpfungsquotienten des Kernbehälters wurden aus einem Satz simultan gemessener Sprungantwortsignale extrahiert. Die Erzeugung der Sprungantwort erfolgte mit einer hydraulischen Snapback-Vorrichtung, die es ermöglichte, den Kernbehälter örtlich vorzuspannen und plötzlich zu entlasten. Für die Extraktion der modalen Kennwerte aus den transienten Beschleunigungs- und Wegsignalen wurde das Rechenprogramm EVA entwickelt und eingesetzt.

Insgesamt wurden 76 Eigenschwingungsmodes des Kernbehälters identifiziert; davon entfallen 32 auf das gekoppelte System Kernbehälter-Wasservorlage und 44 auf den Kernbehälter ohne Wasservorlage. Einige davon sind mehrfache Modes (überwiegend Dubletts) mit gleicher Axial- und Umfangsordnung, aber unterschiedlicher Eigenfrequenz, Dämpfung und Orientierung im Raum. Der kleinste identifizierte Frequenzabstand eines Dubletts, der die gute Frequenzauflösung des Verfahrens illustriert, beträgt 1,5 %.

Das Verfahren stellt keine Bedingungen an die Art der Erzeugung der transienten Antwort und kann deshalb auch dann eingesetzt werden, wenn konventionelle Verfahren nur bedingt einsetzbar sind, wie z.B. in hostilen Bedingungen und bei schlecht zugänglichen Systemen. Die gewonnenen Erfahrungen zeigen, daß das Verfahren auch bei leicht nichtlinearen Systemen zum Einsatz kommen kann.

Der bei der Snapback-Versuchsreihe V59 benutzte Versuchsaufbau, die mathematischen Grundlagen des Rechenprogrammes EVA und die gewonnenen Resultate sind detailliert beschrieben.

<u>Contents</u>	Page
1. Introduction	1
2. Experimental setup	2
3. Theoretical model	5
4. Computer code EVA	8
4.1 Subroutine EIGEST	10
4.2 Subroutine EIGVAL	17
4.3 Subroutines AMPLIT1 and AMPLIT2	24
4.4 Auxiliary subroutines	27
5. Experimental results	32
5.1 Snapback tests V59.1.4 and V59.3.4	32
5.2 Snapback tests V59.2.3 and V59.4.3	36
6. Concluding remarks	39
References	40
Appendix	42
A.1 Derivation of the theoretical mean spectral density function $SD(\omega)$	42
A.2 Derivation of Eq. (4.44)	46
Tables and figures	48 through 84

1. Introduction

In 1980, a series of 3 blowdown and 13 snapback experiments were performed at the HDR experimental facility at Karlstein/Main [1,2]. The common objective of these experimental series has been the verification of the coupled fluid-structure interaction codes currently being developed to assess the dynamic response of the PWR- core barrel in the hypothetical loss-of-coolant accident (LOCA). A brief review of the codes developed and of the preliminary results of the blowdown experiments is given in [1]. The preliminary results of the snapback experiments are summarized in [2,3].

In the loss-of-coolant accident, the hypothetical rupture of the main coolant duct causes the development of an asymmetrical pressure field in the reactor pressure vessel, resulting in the transient dynamic response of the core barrel. In the experimental series [1], the blowdown was initiated by the rupture of a specifically designed rupture disc located on one nozzle of the reactor pressure vessel. The resulting transient response of the core barrel mockup was measured by several accelerometers and displacement transducers and compared with the corresponding theoretical predictions. This comparison represents one part of the planned code verification. Contrary to this type of experiment, the dynamic response studied within the framework of the snapback test series was caused by an abrupt release of the core barrel mockup, previously displaced by concentrated loading. This yielded the following two data sets which are comparable with the theoretical predictions:

1. Set of time history plots describing the dynamic response of the core barrel mockup to the given step relaxation type of loading.
2. Set of natural frequencies and of the corresponding mode shapes of the core barrel mockup.

Evaluation work concerning the first data set is under way and will be reported elsewhere (e.g. in [4, 13]); the objective of this report is the presentation of the second data set. An additional task is the evaluation of the critical damping ratios which are difficult to predict theoretically.

The report is divided into six sections. In the following Section 2 a brief description will be given of the experimental facility used to perform the snapback test series (designated HDR experimental series V 59). Section 3 will summarize the assumptions made in the theoretical model describing the relaxation response of a coupled fluid-structure system. Section 4 will cover the theoretical background of the computer code EVA. The purpose of this code is the extraction of natural frequencies, mode shapes and critical damping ratios of linear systems from the relaxation response signals. Signals of this type were obtained also in the test series V 59. Some typical plots of the measured accelerations and displacements, their Fourier-transformes as well as the extracted natural frequencies, mode shapes and critical damping ratios of the HDR core barrel mockup will be presented in Section 5, which contains also a comparison of these data with the corresponding theoretical predictions obtained with the computer codes CYLDY3 [5] and FLUX2 [6]. Section 6 will contain the conclusions as well as the recommendations for future work. Some mathematical formulas belonging to the theoretical background of the EVA-code will be derived in the Appendix.

2. Experimental setup

The HDR experimental facility in which the snapback experiments were performed comprises among others the reactor pressure vessel, the core barrel mockup and two hydraulic deflection devices for generation of the transient dynamic response (Fig. 1). The pressure vessel is approx. 11 m high and has an inside diameter of nearly 3 m. The cylindrical shell of the core barrel is 7570 mm long (high); its inside diameter is 2614 mm and its wall thickness 23 mm. The mass of the mass ring bolted onto the bottom of the shell equals 13500 kg.

The hydraulic deflection devices are shown separately on the right side of Fig. 1. They are both capable of producing a quasistatical concentrated loading of the core barrel, which can be suddenly released upon breaking of the break bolt. The upper, lighter device, capable of producing the maximum pull of 150 kN, was used to excite the vibration shell modes of the core barrel. This device can be operated under blowdown conditions with an initial temperature of 310^o C and an initial pressure of 110 bar. The lower, heavier device, capable of generating the maximum push of 750 kN, was used

to excite the bending modes of the core barrel. The nominal operating conditions for this device are 20° C and 20 bar. The rupture disc device indicated on the left side of Fig. 1 was used in the blowdown test series mentioned in the Introduction.

Nine inductive displacement transducers, 26 piezoresistive and nine piezoelectric accelerometers were used to measure the dynamic response of the core barrel; the corresponding locations are indicated in the centre of Fig. 1 (the measurement of strain, absolute and differential pressures, temperature etc., also performed in the test series V 59, is not treated in this report). The piezoelectric accelerometers and the inductive displacement transducers, which were used also in the blowdown test series, were qualified to operate under blowdown conditions. The corresponding qualification tests including among others the investigation of the corresponding performance and environmental characteristics (sensitivity, frequency response function, etc.), are described in [7]. The piezoresistive accelerometers (type GA-813 of Kulite) which are not protected against the influence of pressurized water were installed in the protective housings especially designed for this purpose (see Fig. 2).

All the transducers used were individually calibrated in the laboratory before and after the test series. The typical frequency response behaviour of one accelerometer, type GA-813, obtained in the calibration series is illustrated in Figs. 3 and 4. The upper diagram of Fig. 3 shows the modulus $|H(f)|$ and the lower the phase $\varphi(f)$ of the frequency response function (symbol f indicating the frequency). The diagram of the modulus reveals negligible deviations from an ideal horizontal line indicating nearly zero amplitude distortion of the measured acceleration in the whole usable frequency range between 0 and 500 Hz. The diagram of the phase can be approximated by a skew line indicating the constant time delay of approx. 334 msec in the whole frequency range. This is caused by an output filter of the carrier frequency amplifier (type VD6 of Elan, carrier frequency 5000 Hz) completing the measuring chain, and is not characteristic of the accelerometer. The upper diagram (A) in Fig. 4 shows the normalized deviation $(|H(f)| - E)/E$ from the sensitivity E , obtained from the upper diagram in Fig. 3. It indicates that this deviation is, in general, smaller than $\pm 0.6\%$. The lower plot (B) in Fig. 4 shows a similar deviation curve of the same transducer, installed in the protective housing. Intercomparison of the two diagrams (A) and (B) reveals an insignificant ($\leq 1\%$) increase in the deviation caused by trans-

ducer installation in the protective housing. A still smaller influence of the protective housing is apparent from the diagram of the phase distortion $\varphi(f)$ (not reproduced here).

Each transducer installed inside of the reactor pressure vessel was provided with an approx. 20 m long waterproof cable and connected to the corresponding amplifier by a 70 m long connecting cable. Amplified output signals were recorded in the PCM code on analog magnetic tapes and subsequently copied in IBM compatible format on digital tapes. For the evaluation of the registered signals an IBM 3033 computer system was used (further details see Section 4).

Typical time history plots of the transient response signals measured in one experiment of the snapback test series are presented in Fig. 5 (the individual snapback tests are discussed in more detail in Section 5; the particular test No. V 59.3.4 was performed with the 150 kN deflection device and no water charge in the reactor pressure vessel). The upper plot shows the time history of acceleration $a(t)$ measured in the lower third of the core barrel shell (location KS 1204 at $\psi = 110^\circ$, $H = 4250$ mm). The second plot illustrates the transient displacement $y(t)$ measured in the vicinity of the deflection device (location KS 1008 at $\psi = 90^\circ$, $H = 8410$ mm). The transient strain response $\epsilon(t)$ plotted in the lowest diagram of Fig. 5 was measured near the upper edge of the core barrel (location KI 3261; the corresponding strain gauge was installed in the vertical direction on the inner surface of the core barrel at $\psi = 90^\circ$, $H = 9465$ mm). A common feature of all three signals plotted is the nearly random structure and relatively slow decrease of intensity with time. The first phenomenon characterizes the simultaneous contribution by several vibration modes; the second the small values of the corresponding damping ratios. Extraction of the natural frequencies, the corresponding mode shapes and damping ratios from such signals is the aim of the computer code EVA; it will be described in Section 4.

3. Theoretical model

Fluid-structure interaction phenomena observed in the light water reactor systems as well as the problems arising by the development of the corresponding theoretical models all are described in detail in [8]. It is shown that the existing models are preferably linear; the establishment of their limitations as well as the development of non-linear models are considered to be the research goal of the future. The traditional formulation of the linear fluid-structure interaction problem applied to a thin-walled shell submerged in a non-viscous fluid is presented in [9]. The dynamic behaviour of this coupled mechanical system is governed by the following system of four linear differential equations

$$L_{11} u + L_{12} v + L_{13} w = X_1 \quad , \quad (3.1)$$

$$L_{21} u + L_{22} v + L_{23} w = X_2 \quad , \quad (3.2)$$

$$L_{31} u + L_{32} v + L_{33} w = X_3 \quad , \quad (3.3)$$

and

$$\nabla^2 \varphi - \frac{1}{c_0^2} \frac{\partial^2 \varphi}{\partial t^2} = 0 \quad , \quad (3.4)$$

and by the system of suitable boundary and initial conditions. The first three equations describe the response of the shell, the last the response of the fluid. The symbols u , v and w indicate the components of the displacement of the shell in the axial, circumferential and radial directions, respectively; X_1 , X_2 and X_3 are the corresponding components of the dynamic force, L_{11} through L_{33} denote the linear differential operators of the shell, φ the velocity potential of the fluid, ∇^2 the Laplace operator and c_0 the sound velocity. The terms on the right side of Eqs. (3.1) through (3.3) in the case of a non-disturbed problem are described by equations

$$X_1 = -m \frac{\partial^2 u}{\partial t^2} \quad (3.5)$$

$$X_2 = - m^o \frac{\partial^2 v}{\partial t^2} \quad (3.6)$$

and

$$X_3 = - m^o \frac{\partial^2 w}{\partial t^2} + \Delta p \quad (3.7)$$

where Δp indicates the pressure difference, induced in the fluid and acting on the unit area of the control surface of the shell and m^o denotes the corresponding mass of the shell. The first quantity is described by the following equation, obtained as a result of linearization of integral Cauchy-Lagrange

$$\Delta p = \rho_{out} \frac{\partial \varphi_{out}}{\partial t} - \rho_{in} \frac{\partial \varphi_{in}}{\partial t} \quad (3.8)$$

The indices out and in refer to the outside and inside surfaces of the shell, respectively; ρ denotes the density of the fluid. An other condition which must be satisfied on the fluid shell boundary is the compatibility condition

$$\frac{dw}{dt} = - \frac{\partial \varphi}{\partial n} \quad (3.9)$$

where n indicates the inside normal to the control surface. Additional restrictions are defined by usual boundary conditions of the shell as well as by conditions valid on the outside boundary of the fluid.

Let us suppose that the linear mechanical system described above has N degrees of freedom. In [10] it is shown that the free vibration response of such a system can be described by a superposition of $2N$ exponentially decaying terms according to equation

$$S(t) = \sum_{j=1}^{2N} K_j \exp(\lambda_j t), \quad (3.10)$$

where λ_j denotes the conjugate complex roots of the corresponding characteristic equation and K_j indicates the modal amplitudes which are continuous functions of the coordinates. A modified Eq. (3.10) is used as a basis for the computer code EVA.

4. Computer Code EVA

This code was developed to extract the eigenvalues λ_n and the initial values C_{rn} from the set of R input signals of the type

$$X_r(t) = \sum_{n=1}^{2N} C_{rn} \exp(\lambda_n t), \quad (4.1)$$

$r = 1, 2, \dots, R$. Eq. (4.1) is formally identical with Eq. (3.10) describing the free relaxation response of the core barrel. However, it can represent the free relaxation response of any other linear, linearly damped physical system described by $2N$ conjugate complex eigenvalues λ_n and $2RN$ conjugate complex initial values C_{rn} .

The set of eigenvalues λ_n contains N conjugate complex pairs $\alpha_n \pm i\Omega_n$ in accordance with equations

$$\lambda_n = \alpha_n + i\Omega_n \quad (4.2)$$

for $n = 1, 2, \dots, N$ and

$$\lambda_n = \lambda_{N+m} = \alpha_m - i\Omega_m \quad (4.3)$$

for $n = N+m = N+1, N+2, \dots, 2N$

where α_n and Ω_n are defined only for $n = 1, 2, \dots, N$.

They are both real numbers; the first characterizes the damping (in some exceptional cases the excitation) and the second the natural angular frequency of the n -th mode of the physical system under investigation.

The set of $2RN$ initial values C_{rn} comprises RN conjugate complex pairs $\text{Re} \{ C_{rn} \} \pm i \text{Im} \{ C_{rn} \}$ with a real part $\text{Re} \{ C_{rn} \}$ and an imaginary part $\text{Im} \{ C_{rn} \}$. Each set of R initial values C_{rn} belonging to one fixed index n constitutes a one-column matrix \underline{C}_n directly proportional to the n -th mode shape. Similarly, each set of $2N$ initial values C_{rm} belonging to one fixed index r constitutes a one-row matrix \underline{C}_r . The complete set of $2RN$ values C_{rn} constitutes a $R \times 2N$ matrix \underline{C} .¹⁾

1) The bar under the symbol indicates the one-row matrix or the one-column matrix (in some publications called "vectors"); two bars indicate the $n \times m$ matrix.

Each signal set is generally evaluated in five evaluation steps:

- a) The first is the signal conditioning step. It consists of digital filtering usually combined with the reduction of the data sample and with the application of additional damping, if necessary.
- b) In the second evaluation step the complete set of $2N$ eigenvalues λ_n is extracted.
- c) In the third evaluation step the complete set of $2N$ vectors C_{rn} is extracted.
- d) The next evaluation step is the control step. It uses both sets of modal values λ_n and C_{rn} extracted in the previous steps and synthesizes the input signals in accordance with Eq. (4.1). The synthesized signals are compared with the original input signals; the degree of mutual agreement obtained is used to judge the quality of the achieved identification of the physical system being studied.
- e) The task of the last evaluation step is the identification of the azimuthal order of the identified modes (optionally), the printing of the modal data and the plotting of the mode shapes. For this purpose the complex mode shapes are previously reduced to real ones.

The majority of evaluation steps are performed in the frequency domain; for the corresponding transformation the FFT-routine $\overline{[11]}$ (Fast Fourier Transform) is used. The finite Fourier transform of Eq. (4.1) reads

$$\hat{X}_r(\omega, T_m) = \int_0^{T_m} X_r(t) e^{-i\omega t} dt = \sum_{n=1}^{2N} \frac{C_{rn}}{i\omega - \lambda_n} \left(1 - e^{(\lambda_n - i\omega)T_m} \right) \quad (4.4)$$

where T_m denotes the finite length of the time interval of the response signal $x_r(t)$. This finite length is due to the finite block size used in the FFT-routine and to the actual finite length of the response signal. It follows from Eq. (4.4) that the finite value of T_m causes an error equal to $\exp [(\lambda_n - i\omega) T_m]$, which reduces to zero for $T_m \rightarrow \infty$. There are two approaches to reducing this error which are implemented in the EVA code:

- a) The first approach supposes $\exp [(\lambda_n - i\omega) T_m] = 0$ and reduces the error via multiplication of the input signal $x_r(t)$ by an additional damping function $\exp (-\alpha_0 t)$ prior to its transformation into the frequency domain. The subroutine EIGEST based on this approach uses the value of the additional damping coefficient $\alpha_0 = 5/T_m$. It turns out that this choice reduces the error above to less than 1%.
- b) Another approach used in the subroutine EIGVAL uses Eq. (4.4) in its complete form so that additional damping of the input signals is not necessary.

The input signal $x_r(t)$ is transmitted to the computer as a series of $J + 1$ discrete values x_{rj} ($j = 0, 1, \dots, J$); the mutual distance between two neighboring values on the time axis equals $\Delta t = T_m / J$. The FFT subroutine produces the Fourier transform values \hat{x}_{rk} in $K + 1$ equidistantly spaced frequency points ω_k

$$\hat{x}_{rk} = \hat{X}_r(\omega_k); \quad (4.5)$$

$$\Delta\omega = \omega_{k+1} - \omega_k = \pi / T_m, \quad k = 0, 1, \dots, K.$$

The set of Fourier transform values \hat{x}_{rk} is used as a basic data set in all extraction subroutines.

4.1 Subroutine EIGEST

The subroutine EIGEST extracts the eigenvalues λ_n from one "mean" spectral density function $SDM(\omega_k)$ representing the whole set of R input signals ($R(K + 1)$ Fourier transform values \hat{x}_{rk}) according to equation

$$SDM(\omega = \omega_k) = \frac{SD(\omega_k)}{\sum_{k=0}^K SD(\omega_k)} \quad (4.6)$$

where

$$SD(\omega = \omega_k) = \frac{1}{R} \sum_{r=1}^R \hat{x}_{rk} \overline{\hat{x}_{rk}} g_r \quad (4.7)$$

$\overline{\hat{x}}_{rk}$ denotes the conjugate complex value of \hat{x}_{rk} ; g_r denotes the weighting factor of the r-th input signal. The weighting factor g_r is used to facilitate the evaluation of different types of input signals (for instance acceleration signals together with displacement signals). In these cases, g_r must be chosen in such a way as to get the contributions (terms) in Eq. (4.7) of the same order. When all signals are of the same type, $g_r \equiv 1$. The sum

$$\sum_{k=0}^K SD(\omega_k)$$

in the denominator is used only for the purpose of normalizing and can therefore be omitted in the following text. In this sense, $SDM(\omega)$ will be systematically replaced by $SD(\omega)$.

For the extraction of eigenvalues $\lambda_n = \alpha_n \pm i\Omega_n$ from the experimental mean spectral density function $SD(\omega_k)$ the theoretical model of the latter is needed. For this application, the following expression is derived in Appendix A 1

$$SD(\omega) = \sum_{n=1}^N \frac{A_n + B_n(\Omega_n - \omega)}{\alpha_n^2 + (\Omega_n - \omega)^2} + \frac{A_n + B_n(\Omega_n + \omega)}{\alpha_n^2 + (\Omega_n + \omega)^2} \quad (4.8)$$

The derivation of Eq. (4.8) is based on the supposition $\exp[(\lambda_n - i\omega)T_m] = 0$ as already indicated in the preface to this chapter. Insertion of $\omega = \omega_k$ into Eq. (4.8) yields the "model" mean spectral density function which contains $4N$ unknown quantities A_n , B_n , α_n and Ω_n . Two of these quantities (α_n and Ω_n) make part of the wanted eigenvalues λ_n ; the other two (A_n and B_n) are auxiliary quantities which are essential for the estimation of α_n and Ω_n , but not for the estimation of \underline{c}_n .

Owing to the nonlinear character of Eq. (4.8), an immediate extraction of A_n , B_n , α_n and Ω_n is a little bit cumbersome. A substantial amelioration can be achieved when some transformations of variables are performed in advance. As explained in more detail further below, only one term of Eq. (4.8), namely

$$f_n(\omega_k) = \frac{A_n + B_n(\Omega_n - \omega_k)}{\alpha_n^2 + (\Omega_n - \omega_k)^2} \quad (4.9)$$

is used to extract the four unknown quantities A_n , B_n , α_n and Ω_n . The expression on the right side of Eq. (4.9) is set equal to the corresponding portion $f_{\text{exp}}(\omega_k)$ of the mean spectral density function $SD(\omega_k)$ to which the frequency window searching for the quantities A_n , B_n , α_n and Ω_n is applied. This window has the center frequency ω_s and L discrete frequency values on each side. For fixed ω_s , the relation between ω_s and ω_k is given by equation

$$\omega_k = \omega_s + \omega_k' \quad (4.10)$$

containing a new variable ω_k' , which indicates the distance between the window center frequency ω_s and the old variable ω_k . A similar transformation is used also for the eigenvalue Ω_n , namely

$$\Omega_n = \omega_s + \Omega_n' \quad (4.11)$$

Both transformations offer some advantages in numerical calculations. Using Eqs. (4.10) and (4.11), Eq. (4.9) can be rewritten in the form

$$f_{\text{exp}}(\omega_k) = f_{\text{exp}}(\omega_s + \omega_k') = \frac{A_n + B_n(\Omega_n' - \omega_k')}{\alpha_n^2 + (\Omega_n' - \omega_k')^2} \quad (4.12)$$

Instead of A_n , B_n , α_n and Ω_n' , new variables a_0 , a_1 , a_2 and b_1 are introduced according to equations

$$a_0 = \frac{\alpha_n^2 + \Omega_n'^2}{A_n + B_n \Omega_n'} \quad (4.13)$$

$$a_1 = \frac{-2\Omega_n'}{A_n + B_n \Omega_n'}$$

$$a_2 = \frac{1}{A_n + B_n \Omega_n'}$$

$$b_1 = \frac{B_n}{A_n + B_n \Omega_n'}$$

The old variables can be obtained by means of the inverse transformation

$$A_n = \frac{1}{a_2} + \frac{b_1 a_1}{2a_2^2}$$

$$B_n = \frac{b_1}{a_2}$$

$$\alpha_n = -\sqrt{\frac{a_0}{a_2} - \left(\frac{a_1}{2a_2}\right)^2}$$

$$\Omega_n' = -\frac{a_1}{2a_2}$$

(4.14)

Substitution of these quantities into Eq. (4.12) yields

$$f_{\text{exp}}(\omega_k' + \omega_s) = \frac{1 - b_1 \omega_k'}{a_0 + a_1 \omega_k' + a_2 \omega_k'^2} \quad (4.15)$$

The expression on the right side of Eq. (4.15) is a rational function of ω_k' containing unknown coefficients a_0 , a_1 , a_2 and b_1 in the polynomials. Two complementary procedures are used for their extraction. They search for the corresponding peak of the measured spectral density function $SD(\omega_k')$ and approximate the contribution of the n -th mode by the model function Eq. (4.15). The iteration procedure used to make the fit can be derived in a similar way as shown in [12]. Its main steps can be summarized as follows:

a) modified error function

$$\epsilon_{k,s}' = f_{\text{exp}}(\omega_k' + \omega_s)(a_0 + a_1 \omega_k' + a_2 \omega_k'^2) + b_1 \omega_k' - 1 \quad (4.16)$$

is introduced for use in the least square criterion. This function is based on the difference between the experimental spectral density function $f_{\text{exp}}(\omega_k' + \omega_s)$ and its approximation according to Eq. (4.15). It can be written in the following matrix form

$$\epsilon_{k,s}' = \underline{V}_{k,s}^T \underline{A}_s - 1 \quad (4.17)$$

with the matrices

$$\underline{V}_{k,s} = \begin{pmatrix} f(\omega_k' + \omega_s) \\ f(\omega_k' + \omega_s) \omega_k' \\ f(\omega_k' + \omega_s) \omega_k'^2 \\ \omega_k' \end{pmatrix} \quad (4.18)$$

and

$$\underline{A}_s = \begin{pmatrix} a_0 \\ a_1 \\ a_2 \\ b_1 \end{pmatrix} ; \quad (4.19)$$

$\underline{v}_{k,s}^T$ denotes the transposed matrix of $\underline{v}_{k,s}$.

b) Application of the least square criterion reads

$$\sum_{k=-L}^L \epsilon_{k,s}^2 g_{k,s}^2 \rightarrow \min \quad (4.20)$$

where $g_{k,s}$ denotes the weighting factor defined by

$$g_{k,s}^2 = \frac{f_{\exp}^2 (\omega_k' + \omega_s)}{|1 - b_1' \omega_k'|^2} \quad (4.21)$$

Eq. (4.20) leads to Eq. (4.22) allowing to estimate all four elements of the matrix \underline{A}_s

$$\underline{B}_s \underline{A}_s = \underline{Y}_s \quad (4.22)$$

The matrices \underline{B}_s and \underline{Y}_s are defined by the equations

$$\underline{B}_s = \sum_{k=-L}^L g_{k,s}^2 (\underline{v}_{k,s} \underline{v}_{k,s}^T) \quad (4.23)$$

and

$$\underline{Y}_s = \sum_{k=-L}^L g_{k,s}^2 \underline{v}_{k,s} \quad (4.24)$$

c) While derivating Eq. (4.22) it is necessary to suppose that the coefficient b_1 included in $g_{k,s}$ according to Eq. (4.21) is known. This requirement can be satisfied when the iteration procedure indicated below is used for the successive estimation of b_1 . This procedure starts with the value $b_1 = 0$. The new estimate of b_1 obtained from Eq. (4.22) is included in Eq. (4.21) and this two-step process is repeated until stable estimates of b_1 are obtained.

The iteration loop described above produces for each value of ω_s four elements of the matrix $A_{k,s}$. The task of the second iteration procedure, which is superimposed to the first, is to find the eigenvalues Ω_n and α_n . The main steps of the second procedure can be summarized as follows:

a) The procedure is applied to a preselected frequency interval

$\omega_{\text{start}} \leq \omega_s \leq \omega_{\text{end}}$. It is started at $\omega_s = \omega_{\text{start}}$ and uses Eqs. (4.22) and (4.14) to get the corresponding four estimates $A(\omega_{\text{start}})$, $\alpha(\omega_{\text{start}})$, $\Omega'(\omega_{\text{start}})$ and $B(\omega_{\text{start}})$.

b) The procedure skips to the next higher discrete value of ω_s and calculates the corresponding estimates $A(\omega_s)$, $\alpha(\omega_s)$, $\Omega'(\omega_s)$ and $B(\omega_s)$. These estimates together with those from the preceding step are subjected to acceptance testing including the application of the following seven acceptance criteria, applicable for any arbitrary values of ω_s from the frequency interval $\omega_{\text{start}} \leq \omega_s \leq \omega_{\text{end}}$:

$$\left. \begin{aligned}
 &\omega_{s-1} \leq \Omega(\omega_{s-1}) \\
 &\Omega(\omega_s) < \omega_s \\
 &|\Omega(\omega_s) - \Omega(\omega_{s-1})| < \omega_s - \omega_{s-1} \\
 &\alpha(\omega_{s-1}) > 0 \\
 &\alpha(\omega_s) > 0 \\
 &\frac{A(\omega_{s-1})}{\alpha(\omega_{s-1})} > \epsilon \\
 &\frac{A(\omega_s)}{\alpha(\omega_s)} > \epsilon
 \end{aligned} \right\} (4.25)$$

where ϵ denotes the preselected error value.

c) When at least one of these seven criteria is not fulfilled, step b) is repeated with the next higher value of ω_s .

d) When all seven criteria (4.25) are fulfilled, the following mean values are accepted as estimates of Ω_1 , α_1 , A_1 and B_1

$$\left. \begin{aligned} \Omega_{n=1} &= \frac{\Omega(\omega_{s-1}) + \Omega(\omega_s)}{2} \\ \alpha_{n=1} &= \frac{\alpha(\omega_{s-1}) + \alpha(\omega_s)}{2} \\ A_{n=1} &= \frac{A(\omega_{s-1}) + A(\omega_s)}{2} \\ B_{n=1} &= \frac{B(\omega_{s-1}) + B(\omega_s)}{2} \end{aligned} \right\} (4.26)$$

These values are stored in the computer memory and the procedure returns to step b) to proceed in the calculations with the next higher value of ω_s .

The foregoing steps b), c) and d) are repeated until $\omega_s = \omega_{\text{end}}$ is reached. The eigenvalues found are assigned as $\Omega_{n=2}$, $\Omega_{n=3}$, and so on.

4.2 Subroutine EIGVAL

Similarly to the EIGEST subroutine the searching loop uses the frequency window with the center frequency ω_s and L discrete frequency values on each side. In this frequency window the following weighting factor is calculated

$$G_{rs} = g_r \sum_{l=-L'}^{L'} \bar{\hat{x}}_r (\omega_s + l \Delta\omega) \quad (4.27)$$

The integer $L' < L$ determines the frequency step $\Delta\omega' = L' \Delta\omega$ used in the searching loop as indicated further below. In $2L + 1$ discrete frequency values of the window the following weighted spectral density function $SW(\omega_s, \omega_k)$ is defined

$$SW(\omega_s, \omega_k) = \sum_{r=1}^R G_{rs} \hat{x}_r(\omega_k) \quad (4.28)$$

Substitution of $\hat{x}_r(\omega, T_m)$ from Eq. (4.4) into Eq. (4.28) yields for $\omega = \omega_k$

$$\begin{aligned} SW(\omega_s, \omega_k) &= \sum_{r=1}^R G_{rs} \sum_{n=1}^{2N} \frac{C_{rn}}{i\omega_k - \lambda_n} \left[1 - e^{(\lambda_n - i\omega_k)T_m} \right] \\ &= \sum_{n=1}^{2N} \frac{Z_{sn}}{i\omega_k - \lambda_n} \left[1 - e^{(\lambda_n - i\omega_k)T_m} \right] \end{aligned} \quad (4.29)$$

where

$$Z_{sn} = \sum_{r=1}^R G_{rs} C_{rn} \quad (4.30)$$

In analogy to the preceding paragraph we introduce ω_k^i in accordance with Eq. (4.10) and

$$\lambda_n^i = \lambda_n - i\omega_s \quad (4.31)$$

for $n = 1, 2, \dots, 2N$. It should be noticed here that the new quantities λ_n^i do not form the conjugate complex pairs as do the eigenvalues λ_n . Substitution of ω_k and λ_n from Eqs. (4.10) and (4.30) into Eq. (4.28) yields

$$\begin{aligned}
 SW(\omega_s, \omega_k) &= \sum_{n=1}^{2N} \frac{Z_{sn}}{i\omega'_k - \lambda'_n} \left[1 - e^{(\lambda'_n - i\omega'_k) T_m} \right] \\
 &= \sum_{n=1}^{2N} \left\{ \frac{Z_{sn}}{i\omega'_k - \lambda'_n} - \frac{Z'_{sn} e^{-i\omega'_k T_m}}{i\omega'_k - \lambda'_n} \right\} \quad (4.32)
 \end{aligned}$$

where

$$Z'_{sn} = Z_{sn} e^{\lambda'_n T_m}$$

Let us suppose that the frequency window $\langle \omega_{s-L}, \omega_{s+L} \rangle$ contains no more than a small number $N' < N$ of eigenmodes satisfying the inequality

$$\omega_{s-L} < \Omega_{n'=1} < \Omega_{n'=2} < \dots < \Omega_{n'} < \omega_{s+L}$$

as well as the requirement

$$SW(\omega_s, \omega_k) = \sum_{n'=1}^{N'} \left[\frac{Z_{sn'}}{i\omega'_k - \lambda'_{n'}} - \frac{Z'_{sn'} e^{-i\omega'_k T_m}}{i\omega'_k - \lambda'_{n'}} \right] \quad (4.33)$$

Eq. (4.33) assumes that the contribution of all remaining $N - N'$ eigenmodes to the weighted spectral density function may be neglected in the frequency window $\langle \omega_{s-L}, \omega_{s+L} \rangle$. The right side of Eq. (4.33) can be written as a sum of two partial fractions in the form

$$SW(\omega_s, \omega_k) = \frac{q(\omega'_k)}{p(\omega'_k)} - \frac{q'(\omega'_k)}{p(\omega'_k)} \quad (4.34)$$

with

$$q(\omega'_k) = \sum_{n'=1}^{N'} Z_{sn'} \prod_{m \neq n'}^{N'} (i\omega'_k - \lambda'_m) \quad (4.35)$$

$$q'(\omega'_k) = e^{i\omega'_k T_m} \sum_{n'=1}^{N'} Z'_{sn'} \prod_{m \neq n'}^{N'} (i\omega'_k - \lambda'_m) \quad (4.36)$$

and

$$p(\omega'_k) = \prod_{n'=1}^{N'} (i\omega'_k - \lambda'_{n'}) \quad (4.37)$$

Eq. (4.34) is used as a basis to define the error

$$\epsilon_{s,k} = SW_{\text{exp}}(\omega_s, \omega_k) \frac{p(\omega'_k)}{q(o)} - \frac{q(\omega'_k)}{q(o)} + \frac{q'(\omega'_k)}{q(o)} \quad (4.38)$$

which will be used in the least square criterion further below. It contains the weighted spectral density function $SW_{\text{exp}}(\omega_s, \omega_k)$ obtained directly from the input signals. The partial fractions on the right side of Eq. (4.38) can be written in the form of polynomials

$$\frac{q(\omega'_k)}{q(o)} = 1 + b_1 i\omega'_k + b_2 (i\omega'_k)^2 \dots b_{N'-1} (i\omega'_k)^{N'-1} \quad (4.39)$$

$$\frac{q'(\omega'_k)}{q(o)} = \left[b'_0 + b'_1 i\omega'_k + b'_2 (i\omega'_k)^2 \dots + b'_{N'-1} (i\omega'_k)^{N'-1} \right] e^{i\omega'_k T_m} \quad (4.40)$$

and

$$\frac{\dot{p}(\omega'_k)}{q(o)} = a_0 + a_1 i\omega'_k + a_2 (i\omega'_k)^2 \dots a_{N'} (i\omega'_k)^{N'} \quad (4.41)$$

It should be noted here that the coefficients $b_1, \dots, b_{N'-1}$; $b'_0, b'_1, \dots, b'_{N'-1}$ and $a_0, a_1, \dots, a_{N'}$ are not identical with those included in Eq. (4.15).

The set of linear equations necessary to estimate these coefficients can be obtained by minimization of the integral square of the weighted error according to the equation

$$\sum_{k=s-L}^{s+L} |g_{s,k}|^2 |\epsilon_{s,k}|^2 \longrightarrow \min \quad (4.42)$$

containing the weight (not identical with the weight defined by Eq. (4.21))

$$|g_{s,k}|^2 = |SW_{\text{exp}}(\omega_s, \omega_k)|^2 \quad (4.43)$$

The set of partial derivations implied by Eq. (4.42) yields (see Appendix A2)

$$\underline{Q}_s \underline{Y}_s = \underline{P}_s \quad (4.44)$$

containing the matrix \underline{Y}_s of the unknown coefficients (dimension $3N' \times 1$)

$$\underline{Y}_s = \left\{ \begin{array}{c} a_0 \\ a_1 \\ \cdot \\ \cdot \\ a_{N'} \\ b_1 \\ \cdot \\ \cdot \\ b_{N'-1} \\ b'_0 \\ b'_1 \\ \cdot \\ \cdot \\ b'_{N'-1} \end{array} \right\} \quad (4.45)$$

The matrix \underline{P}_s (dimension $3N' \times 1$) is defined by equation

$$\underline{P}_s = \sum_{k=s-L}^{s+L} |g_{s,k}|^2 \underline{V}_{s,k} \quad (4.46)$$

with

$$\underline{V}_{s,k} = \left\{ \begin{array}{l} SW_{exp}(\omega_s, \omega_k) \\ SW_{exp}(\omega_s, \omega_k) i\omega'_k \\ \vdots \\ SW_{exp}(\omega_s, \omega_k) (i\omega'_k)^{N'-1} \\ i\omega'_k \\ \vdots \\ (i\omega'_k)^{N'-1} \\ e^{-i\omega'_k T_m} \\ e^{-i\omega'_k T_m} i\omega'_k \\ \vdots \\ e^{-i\omega'_k T_m} (i\omega'_k)^{N'-1} \end{array} \right\} \quad (4.47)$$

Again, the matrix $\underline{V}_{s,k}$ is not identical with the similarly denoted matrix in the preceding paragraph. The matrix \underline{Q}_s (dimension $3N' \times 3N'$) is defined by equation

$$\underline{Q}_s = \sum_{k=s-L}^{s+L} |g_{s,k}|^2 \underline{V}_{s,k} \underline{V}_{s,k}^H \quad (4.48)$$

$\underline{V}_{s,k}^H$ is Hermitian (dimension $1 \times 3N'$) to $\underline{V}_{s,k}$

The solution of Eq. (4.44) gives all unknown $3N'$ coefficients $a_0, \dots, b'_{N'-1}$. First the $N'+1$ coefficients $a_0, a_1, \dots, a_{N'}$ are substituted into Eq. (4.41) to obtain N' roots of the polynomial $p(\omega'_k)$ in accordance with Eq. (4.37). The remaining $2N'-1$ coefficients $b_1, \dots, b_{N'-1}, b'_0, b'_1, \dots, b'_{N'-1}$ are auxiliary quantities not applied further in the analysis.

The searching step described above furnishes one set of N' roots λ_n for every value of the center frequency ω_s (for every frequency window). The performance of the whole searching loop can be summarized as follows: The subroutine starts at the lowest value of the preselected frequency interval $\omega_{start} \leq \omega_s \leq \omega_{end}$, sets $\omega_s = \omega_{start}$ and determines the corresponding set of N' roots λ'_n . The subroutine then skips to the next frequency window with the center frequency $\omega_s = \omega_{start} + L'$ and determines the second set of N' roots $\lambda'_{m'}$. With both sets available, the following operations are performed:

- a) Eq. (4.30) is used to determine $\lambda_{n'} = \lambda'_n + i\omega_s$ (ω_s denotes the center frequency of the first frequency window) and $\lambda_{m'} = \lambda'_{m'} + i\omega_s$ (ω_s denotes the center frequency of the second frequency window).
- b) All values satisfying $\text{Im } \lambda_{n'} < \omega_{start}$, $\text{Im } \lambda_{m'} < \omega_{start}$
 $\text{Im } \lambda_{n'} > \omega_{start} + L'$ and $\text{Im } \lambda_{m'} > \omega_{start} + L'$
 ($\text{Im } \lambda$ denotes the imaginary part of λ) are excluded from the analysis in this step.
- c) Every remaining root $\lambda_{n'}$ from the first step is compared with every remaining root $\lambda_{m'}$ from the second step; the pairs satisfying the condition $|\lambda_{n'} - \lambda_{m'}| = \min$ are chosen as potential eigenvalue candidates.
- d) Mean values $(\lambda_{n'} + \lambda_{m'})/2$ of the chosen pairs satisfying the acceptance criterion $|\lambda_{n'} - \lambda_{m'}|^2 < \Delta\omega^2/2$ are accepted as identified eigenvalues. The remaining pairs which do not satisfy the acceptance criterion are excluded from the analysis in the respective step.

Having stored the accepted eigenvalues the subroutine skips to the next frequency window and the process above is repeated. Searching is stopped when the upper value ω_{end} of the frequency interval $(\omega_{start}, \omega_{end})$ is attained.

The advantage of the subroutine EIGVAL lies in the exploitation of the orthogonality of modes, intensifying contribution of modes actually being identified to the weighted spectral density function. The choice of the input parameters L , L' and N' depends on the density and damping values of the modes in the preselected frequency interval $\langle \omega_{\text{start}}, \omega_{\text{end}} \rangle$, on the filter bandwidth $\Delta\omega$ and on the time duration T_m of the response signals. The choice of the input parameters L and N' is restricted by the condition $2L > 3N'$ resulting from computational considerations. The results of analysis presented further below in Section 5 were obtained with $L' = 1$, $L = 18$ and $N' = 6$.

4.3 Subroutines AMPLIT 1 and AMPLIT 2

When all $2N$ eigenvalues λ_n are known, the complete set of RK Fourier transformed values $\hat{x}_{r,k} = \hat{x}_r(\omega_k)$ is no longer necessary to estimate the remaining unknown $2RN$ initial values C_{rn} . Instead, each subset of $K+1$ values corresponding to a fixed r can be reduced to N smaller groups, each of them being connected with one eigenfrequency value Ω_n . Each group contains $2M$ values $\hat{x}_r(\omega_{n,m})$ ($m = \pm 1, \pm 2, \dots, \pm M$) where M denotes a variable input parameter ($M \geq 2$). One half of these frequency values (those with $m = -M, -M+1, \dots, -1$) are located to the left, the other half ($m = 1, 2, \dots, M$) to the right from Ω_n on the frequency axis. All $2M$ frequency values of one group fill the frequency band

$$\omega_{n,-M}, \omega_{n,-M+1}, \dots, \omega_{n,-1}, \Omega_n, \omega_{n,1}, \omega_{n,2}, \dots, \omega_{n,M},$$

having Ω_n approximately in the center. Substitution of $\omega_{n,m}$ from this set into Eq. (4.4) yields the basic equation of the form

$$\hat{x}_r(\omega_{\eta,m}, T_m) = \sum_{n=1}^{2N} \frac{C_{rn}}{i\omega_{\eta,m} - \lambda_n} \left[1 - e^{(\lambda_n - i\omega_{\eta,m}) T_m} \right] \quad (4.49)$$

where $\omega_{n,m}$ was exchanged for $\omega_{\eta,m}$ to indicate that $\omega_{\eta,m}$ is fixed (η corresponds to n , but does not take part in the summation). The two different approaches mentioned in the introduction to this section are based on two different forms of the basic equation (4.49). One approach utilized in the subroutine AMPLIT 2 is based on Eq. (4.49) in the full form. The other approach utilized in the subroutine AMPLIT 1 neglects the second term in parentheses

yielding the approximation

$$\hat{x}_r(\omega_{\eta,m}) = \sum_{n=1}^{2N} \frac{C_{rn}}{i\omega_{\eta,m} - \lambda_n} \quad (4.50)$$

The system of 4 MN equations represented by Eq. (4.50) can be written in the matrix form

$$\hat{x}_r = \underline{A} \underline{C}_r^T \quad (4.51)$$

where \underline{C}_r^T is a 1x2 N matrix of the unknown initial values C_{rn} and \underline{A} is a 4 MN x 2 N matrix constructed according to the scheme

$$\underline{A} = \begin{pmatrix} \frac{1}{i\omega_{1,-M} - \lambda_1} & \frac{1}{i\omega_{1,-M} - \lambda_2} & \dots & \frac{1}{i\omega_{1,-M} - \lambda_{2N}} \\ \vdots & \vdots & & \vdots \\ \frac{1}{i\omega_{2N,M} - \lambda_1} & \frac{1}{i\omega_{2N,M} - \lambda_2} & \dots & \frac{1}{i\omega_{2N,M} - \lambda_{2N}} \end{pmatrix} \quad (4.52)$$

Eq. (4.52) offers the possibility to formulate the least square error criterion in the form

$$\left\| \hat{x}_r - \underline{A} \underline{C}_r^T \right\|^2 \rightarrow \min \quad (4.53)$$

The set of partial derivations implied in Eq. (4.53) yields the set of linear equations

$$\underline{A}^H \hat{x}_r = \underline{A}^H \underline{A} \underline{C}_r^T \quad (4.54)$$

used to calculate the matrix \underline{C}_r of the unknown quantities C_{rn} .

A similar set of linear equations is also used in the subroutine AMPLIT 2. It is based on Eq. (4.49) written as

$$\hat{x}_r(\omega_{\eta,m}, T_m) = \sum_{n=1}^{2N} \left[\frac{C_{rn}}{i\omega_{\eta,m} - \lambda_n} - \frac{C'_{rn} e^{-i\omega_{\eta,m} T_m}}{i\omega_{\eta,m} - \lambda_n} \right] \quad (4.55)$$

with

$$C'_{rn} = C_{rn} e^{\lambda_n T_m} \quad (4.56)$$

Eq. (4.55) can be rewritten in the matrix form

$$\underline{\hat{x}}_r = \underline{\underline{A}} \underline{\underline{C}}_r^T - \underline{\underline{A}}' \underline{\underline{C}}_r'^T = (\underline{\underline{A}}, -\underline{\underline{A}}') \begin{pmatrix} \underline{\underline{C}}_r^T \\ \underline{\underline{C}}_r'^T \end{pmatrix} \quad (4.57)$$

where $\underline{\underline{A}}$ denotes a $4MN \times 2N$ matrix constructed according to the scheme

$$\underline{\underline{A}}' = \begin{pmatrix} \frac{e^{-i\omega_{1,-M} T_m}}{i\omega_{1,-M} - \lambda_1} & \dots & \frac{e^{-i\omega_{1,-M} T_m}}{i\omega_{1,-M} - \lambda_{2N}} \\ \vdots & & \vdots \\ \frac{e^{-i\omega_{2N,M} T_m}}{i\omega_{2N,M} - \lambda_1} & \dots & \frac{e^{-i\omega_{2N,M} T_m}}{i\omega_{2N,M} - \lambda_{2N}} \end{pmatrix} \quad (4.58)$$

and

$$\underline{\underline{C}}_r' = (C_{r1} e^{\lambda_1 T_m}, C_{r2} e^{\lambda_2 T_m}, \dots, C_{r2N} e^{\lambda_{2N} T_m}) \quad (4.59)$$

The least square error criterion formulated in the form

$$\left\| \hat{\underline{x}}_r - (\underline{A}_r, \underline{A}'_r) \begin{pmatrix} \underline{C}_r^T \\ \underline{C}'_r^T \end{pmatrix} \right\|^2 \rightarrow \min \quad (4.60)$$

yields the system of linear equations

$$(\underline{A}_r, \underline{A}'_r)^H \hat{\underline{x}}_r = (\underline{A}_r, \underline{A}'_r)^H (\underline{A}_r, \underline{A}'_r) \begin{pmatrix} \underline{C}_r^T \\ \underline{C}'_r^T \end{pmatrix} \quad (4.61)$$

used to estimate the unknown initial values C_{rn} and C'_{rn} .

In the computer code EVA the subroutine AMPLIT 1 is used in combination with the subroutine EIGEST, and AMPLIT 2 in combination with EIGVAL. The results of analysis presented in the Section 5 were obtained with AMPLIT 2, $M = 5$.

4.4 Auxiliary subroutines

The computer code EVA is written in PL1-computer language and utilizes the PL-MATH procedures and subroutines described in the procedure library [11]. In addition to these procedures and to the four extraction subroutines treated in the preceding paragraphs of this section, several additional auxiliary subroutines are used. The characteristic features of the most important of these subroutines will be summarized below.

The subroutine DAT3PUT is used to filter and reduce the original input data sets before they are stored in the working area of the computer memory. These operations are characterized by the reduction factor ρ and by the cut-off frequency $f_c = \omega_c / 2\pi$ of the variably programmable digital low-pass filter operating in the following manner: The portion of the original data set consisting of $(K+1)\rho$ individual input data is subdivided into $L = (K+1)/128$ data subsets. Each data subset originally containing 128ρ individual data is completed to give the total number of 256ρ data (by adding 64ρ zeros before and after the original data subset, respectively) and subsequently Fourier-transformed so that a new subset is obtained in the frequency domain,

which contains 128 ρ individual data. The first 128 values of this subset are multiplied by an attenuation function

$$A(\omega) = \frac{1}{\sqrt{1 + \left(\frac{\omega}{\omega_c}\right)^{2\kappa}}} \quad (4.62)$$

(Butterworth filter of order κ) and inverse-transformed into the time domain; this yields a new data subset containing 256 values. The first 64 as well as the last 64 values of this subset are nearly zero; the remaining 128 values located at the centre of the corresponding time interval represent an intermediate result of filtering. Subsequent application of this procedure also to the second, third, a.s.o., until the L-th subset of the original data set and the final superposition of all L portions (including also all near zero values mentioned above) in the time domain yield the filtered version of the original input signal. The corresponding new data sample contains only a ρ^{-1} part of the data, compared with the original data set, which reduces considerably the demands on the computer memory and the computation time. The cut-off frequency $f_c = \omega_c / 2\pi$ is freely programmable within the limits

$$0,2 \leq \frac{2 f_c \rho}{f_s} \leq 0,9 \quad (4.63)$$

where f_s indicates the sampling frequency used for recording the original input signal. The results of analysis presented further below were obtained with $\rho = 5$ and $f_s = 2500$ Hz; the cut-off frequency f_c was varied in accordance with the type of experiment (see Section 5).

The subroutine REKON is used to reconstruct the input signals $x_r(t)$ from the extracted α_n and C_{rn} values according to equation

$$X_r(t) = \sum_{n=1}^N |C_{rn}| e^{-\alpha_n t} \cos(\omega t - \varphi_{rn}), \quad (4.64)$$

where

$$\varphi_{rn} = \text{arctg} \frac{\text{Im } C_{rn}}{\text{Re } C_{rn}} \quad (4.65)$$

The comparison of the original with the reconstructed input signals is used to assess the achieved grade of system identification performed.

The subroutine MODPLT calculates and plots the simplified initial amplitudes C_{rn}^s , defined by the equation

$$C_{rn}^s = |C_{rn}| \cos(\varphi_{rn} - \varphi_{on}) \quad (4.66)$$

φ_{on} indicates the fixed phase value of the simplified n-th mode. The calculation of φ_{on} is based on the requirement

$$\varepsilon_{\varphi} = \sum_{r=1}^R \left[|C_{rn}| \cos(\varphi_{rn} - \varphi_{on}) \right]^2 \rightarrow \max \quad (4.67)$$

implying the equation

$$\begin{aligned} \frac{\partial \varepsilon_{\varphi}}{\partial \varphi_{on}} &= \sum_{r=1}^R 2 |C_{rn}|^2 \cos(\varphi_{rn} - \varphi_{on}) \sin(\varphi_{rn} - \varphi_{on}) \\ &= \sum_{r=1}^R |C_{rn}|^2 \sin(2\varphi_{rn} - 2\varphi_{on}) \quad (4.68) \end{aligned}$$

$$\Rightarrow \sum_{r=1}^R |C_{rn}|^2 (\sin 2\varphi_{rn} \cos 2\varphi_{on} - \cos 2\varphi_{rn} \sin 2\varphi_{on}) = 0$$

Eq. (4.68) immediately yields

$$\varphi_{on} = \frac{1}{2} \text{arc tg} \frac{\sum_{r=1}^R |C_{rn}|^2 \sin 2\varphi_{rn}}{\sum_{r=1}^R |C_{rn}|^2 \cos 2\varphi_{rn}} \quad (4.69)$$

Eq. (4.66) defines the simplified n-th mode shape as a projection of the original n-th mode shape to the plane $\varphi_{on} = \text{const}$. These simplifications are systematically used in the presentation of the extracted mode shapes in Section 5.

In case of response signals measured on one definite circular perimeter of the rotational symmetric shells it is sometimes convenient to approximate the corresponding simplified initial amplitudes C_{rn}^s by an auxiliary harmonic function having a finite number of simple cosine waves on the circular perimeter. The subroutine MODPLT can calculate and plot also such an auxiliary cosine curve. To derive the corresponding equations let us suppose that R' transducers are located in the angular positions $\psi_{r'}$, of the circle, $r' = 1, 2, \dots, R'$. To find the best fit it is necessary to optimize the circumferential order ν of the given mode shape, the amplitude A_ν and the phase ψ_ν of the harmonic function

$$A_\nu \cos(\nu\psi_{r'} - \psi_{\nu 0}) = a_\nu \cos(\nu\psi_{r'}) + b_\nu \sin(\nu\psi_{r'}) , \quad (4.70)$$

which has been chosen to approximate the experimental values $C_{r'n}^s$ (supposing n to be fixed). This optimization problem can be solved in two steps. In the first step the individual pairs of the unknown coefficients a_ν and b_ν related to A_ν and $\psi_{\nu 0}$ via the transformation

$$A_\nu^2 = a_\nu^2 + b_\nu^2 \quad (4.71)$$

and

$$\text{tg} \psi_{\nu 0} = \frac{b_\nu}{a_\nu} \quad (4.72)$$

are calculated for each n , $\nu = 1, 2, \dots, 12$ (the routine shall not be used for $\nu > 12$). In the second step the correlation technique is used to determine the most probable value of the circumferential order ν of the given n -th mode. The least square criterion used in the first step reads

$$\sum_{r'=1}^{R'} \left[C_{r'n}^S - a_\nu \cos(\nu \psi_{r'}) - b_\nu \sin(\nu \psi_{r'}) \right]^2 \rightarrow \min, \quad (4.73)$$

yielding the following system of two equations for two unknown coefficients a_ν and b_ν .

$$\sum_{r'=1}^{R'} C_{r'n}^S \cos(\nu \psi_{r'}) = a_\nu \sum_{r'=1}^{R'} \cos^2(\nu \psi_{r'}) + b_\nu \sum_{r'=1}^{R'} \cos(\nu \psi_{r'}) \sin(\nu \psi_{r'}) \quad (4.74)$$

$$\sum_{r'=1}^{R'} C_{r'n}^S \sin(\nu \psi_{r'}) = a_\nu \sum_{r'=1}^{R'} \cos(\nu \psi_{r'}) \sin(\nu \psi_{r'}) + b_\nu \sum_{r'=1}^{R'} \sin^2(\nu \psi_{r'}). \quad (4.75)$$

In the second step the correlation coefficient

$$\gamma_\nu = \frac{\sum_{r'=1}^{R'} \left\{ C_{r'n}^S [a_\nu \cos(\nu \psi_{r'}) + b_\nu \sin(\nu \psi_{r'})] \right\}^2}{\left[\sum_{r'=1}^{R'} (C_{r'n}^S)^2 \right] \left[\sum_{r'=1}^{R'} [a_\nu \cos(\nu \psi_{r'}) + b_\nu \sin(\nu \psi_{r'})]^2 \right]} \quad (4.76)$$

is calculated for each ν , $\nu = 1, 2, \dots, 12$. The specific value of ν which yields the maximum correlation coefficient γ_ν is specified as a circumferential order of the given n -th mode. The corresponding cosine curve, according to Eq. (4.70), is plotted together with the corresponding $C_{r'n}^S$ values in one plot.

5. Experimental results

All experiments performed in the test series V59 can be divided into four groups, depending on the fluid charge (reactor pressure vessel empty or filled with water kept at static pressure of 20 bar) and on the location of the snapback device (150 KN or 750 KN device) used to excite the system. For the extraction of eigenvalues $\lambda_j = \xi_j \omega_j + i\Omega_j$ and of the corresponding mode shapes one representative experiment of each group was completely evaluated; the test number and the most important parameters of these four experiments are summarized below in Table 1 (complete test matrix is given in [2]). The results of evaluation of these four tests are presented in the following two paragraphs of this section. Paragraph 5.1 refers to the tests performed with the empty system (no water charge in the reactor pressure vessel - test Nos. V59.1.4 and V59.3.4); paragraph 5.2 refer to those performed with the filled system (test Nos. V59.2.3 and V59.4.3). It is shown that the presence of the water charge in the reactor pressure vessel considerably reduces the natural frequencies in accordance with the theoretical predictions.

Test number	Fluid charge	Snapback device [KN]	Initial force [KN]	Initial displacement [mm]
V59.1.4	air	750	738	3.8
V59.2.3	water	750		
V59.3.4	air	150	140	1.1
V59.4.3	water	150		

Table 1: Parameters of four snapback tests evaluated.

5.1 Snapback tests V59.1.4 and V59.3.4

One typical acceleration input signal measured in each of these two snapback tests and its Fourier-transform are plotted in figs. 6 and 7. The corresponding accelerometer was positioned approximately in the center of the core barrel (KS 1206, $Z = 5004$ mm, $\psi = 110^\circ$). It follows from these diagrams that at least 20 modes participate in the acceleration response of the core barrel. To reduce the computer storage requirements, the eigenvalues and the corresponding mode shapes were extracted in two frequency intervals. In the first case the analysis was performed in the frequency

range 0-120 Hz; the frequency range of the second case was situated between 90 and 210 Hz. The corresponding computer storage requirement was 300 Mega-bytes, the CPU-time was approx. 13 minutes for each run. The evaluation yielded 44 identified eigenmodes. The most important characteristics of these modes are summarized in Table 2. The numeration of these modes (mode number in the first column) corresponds to the increasing value of the natural frequency extracted (second column). Further columns of Table 2 contain the following quantities: eigenfrequency f , critical damping ratio ξ , axial order μ of the given mode (defined as a number of half-waves on the generatrix of the core barrel in the case of shell modes or as a number of quarter-waves in the case of beam modes), circumferential order ν , γ_V^2 -value, phase angle ψ_{V_0} (the last three quantities were estimated with the subroutine MODPLT, described in paragraph 4.4), number of the test in which the given signal possessed the best signal/noise ratio and, finally, number of figure where the given mode is documented. The mode shapes of all 44 modes extracted are plotted in Figs. 8 through 15. The plots on the left illustrate the axial mode shape measured by the accelerometers placed at different vertical positions Z at the azimuthal coordinate $\psi = 110^\circ$ (see Fig. 1). The plots on the right side illustrate the circumferential mode shapes, measured at different azimuthal positions ψ on the vertical coordinate $Z = 8000$ mm. The dashed line in these diagrams is the auxiliary cosine curve calculated with the subroutine MODPLT.

Both diagrams in the first row of Fig. 8 illustrate the mode which has the lowest natural frequency $f = 12.36$ Hz (mode ①). They represent the lateral vibration of the nearly rigid core barrel in the direction perpendicular to the vertical axis - the axial mode shape is a straight line parallel to the vertical axis. The appearance of this mode which was not predicted theoretically was probably caused by the vibration of the reactor pressure vessel, supposed to be rigid in the corresponding mathematical model. The diagrams in the second and third rows illustrate two different variants of the fundamental beam mode. Mode ② has the natural frequency $f = 15.79$ Hz, the damping ratio $\xi = 1.48$ %, and the phase angle $\psi_0 = 176^\circ$; the corresponding values of mode ③ equal 16.2 Hz, 1.37 % and 120° . The appearance of two slightly different variants - called doublet in the following text - of one particular mode is probably caused by the unsymmetry of manufacturing of the core barrel. Modes ④ and ⑤ constitute another doublet belonging to the shell mode first axial and third circumferential order. These modes have slightly different natural frequency values, 39.03 and 39.16 Hz. Such

a small natural frequency difference poses high requirements on the resolution capability of the extraction subroutine. It turned out that such an extreme resolution requirement could be achieved only by the utilization of the subroutine EIGVAL, developed after the preliminary evaluations [2, 3]. The resolution capability of the subroutine EIGEST, used in the preliminary evaluation phase, was not sufficient to extract both versions of this mode. It follows from Table 2 that the majority of modes extracted constitute doublets. In 44 modes documented in Table 2 and Figs. 8 through 15, 18 doublets and 8 singlets participate.

The extracted natural frequencies are compared with the corresponding theoretical values (calculated with the computer code CYLDY3 [5]) in Fig. 16. The calculated natural frequencies are designated with the symbol \bullet , the extracted ones with the symbol \circ (in case of snapback test No. V59.1.4) or \diamond (snapback test No. V59.3.4). It follows from this diagram that the computed natural frequencies of the modes of low circumferential order are a little bit higher than the extracted values. This trend inverses with increasing circumferential order. An interesting phenomenon illustrated in Fig. 16 is the occurrence of two doublets of the shell mode first axial and second circumferential order (modes ⑥, ⑨, ⑫ and ⑭ in Table 2). However, it follows from Figs. 9 and 10 that the axial order of the modes ⑫ and ⑭ achieves a little bit more than pure order of one. It has a certain similarity to the beam mode and therefore, cannot be classified as a pure shell mode. The natural frequency of the mode ⑭ (80.77 Hz) is five times the value of the fundamental beam mode ③ (16.2 Hz). It is not excluded that the occurrence of this mode is caused by non-linear coupling between the fundamental beam mode and the shell mode first axial and second circumferential order.

Critical damping ratios ξ of extracted modes from Table 2 are plotted over the circumferential order V in Figs. 17 and 18. Fig. 17 illustrates the ξ -values of the fundamental beam mode and of the shell modes first axial order. The greatest ξ -value of 3.07 % is not included in Fig. 17 because the mode ① was not qualified as a core barrel mode. This maximal value is followed by the ξ -values of 1.42 and 1.37 of the two variants of the fundamental beam mode. Critical damping ratios of all four variants of the shell mode first axial and second circumferential order lay between 0.21 and 0.53 %. All seven ξ -values discussed above were obtained by the test No. V59.1.4 (symbol \circ). All remaining modes with $\xi \leq 0.22$ were extracted from

the signals of the test No. V59.3.4 (symbol \diamond). It is probable that the 7 modes discussed above induce flexural deformations of the upper core barrel flange, yielding a higher energy dissipation due to mutual rubbing of the flanges. This obviously does not take place in case of shell modes with $V > 2$, preferably excited at the core barrel shell with the upper deflection device (150 kN device). In case of modes extracted in both experiments, the ξ -values extracted in test No. V59.1.4 are generally slightly higher (approx. 20 %) than those extracted in test No. V59.3.4. The ξ -values of the shell modes second, third and fourth axial order ($\mu = 2, 3$ and 4) are plotted over V in Fig. 18. With few exceptions, they are all smaller than 0.2 %.

A comparison of the original with the reconstructed input signal - necessary for the quality assessment of the system identification achieved - is presented in Figs. 19 and 20. All diagrams refer to the accelerometer signals measured at the same position (KS 1206, $Z = 5004$ mm, $\psi = 110^\circ$). The diagram on the left of the first row shows the original filtered signal $X(t)$ used for the analysis, the diagram on the right shows the modulus $|\hat{X}(t)|$ of the corresponding Fourier transform. The diagrams in the second row illustrate the reconstructed signal, obtained from the extracted modal quantities by means of the subroutine REKON (see paragraph 4.4). The diagrams in Fig. 19 refer to the test No. V59.1.4 and contain substantial contributions from the fundamental beam mode. By contrast, the diagrams in Fig. 20 referring to the test No. V59.3.4 contain substantial contributions from the shell modes. The diagrams of $|\hat{X}(t)|$ on the right of Fig. 19 indicate the existence of one mode positioned near 106 Hz; which was not identified in the analysis. The omission of this mode was obviously caused by the poor signal/noise-ratio of the corresponding contribution. Such contributions at a low energy level play an insignificant role in the total response and therefore cannot be noticed in the corresponding time history plot. The comparison of the time history plots on the left side of Fig. 19 demonstrates that all modes with significant contributions to the total response were correctly identified. A similar conclusion can be drawn also from the comparison of the time history plots on the left side of Fig. 20.

5.2 Snapback tests V59.2.3 and V59.4.3

One typical acceleration input signal measured in each of these tests is plotted together with its Fourier transform in Figs. 21 and 22. The corresponding accelerometer position was the same as in Figs. 6 and 7, e.g. KS 1206. The plots indicate a remarkable shift of the natural frequencies to the lower values, caused by the presence of the water charge in the reactor pressure vessel. This frequency shift allowed to perform the analysis in only one frequency range 0 - 110 Hz. In this frequency range 32 vibration modes were identified whose most important characteristics are summarized in Table 3. The corresponding mode shapes are plotted in Figs. 23 through 28. Similar to the case before, several doublets, but not so many as in Figs. 8 through 15, can be identified. The reason for the non-occurrence of some doublets is the stabilizing effect of the water charge, reducing the relative distance of the natural frequencies in the energy spectrum. Likewise not identified was the lateral mode of the system reactor pressure vessel - core barrel, designated as mode (1) in Table 2. The reason for the non-occurrence of this mode was probably the inertia growth of the reactor pressure vessel, due to the presence of the water charge. An additional phenomenon is the occurrence of two new doublets belonging to the beam mode second (modes (6) and (7)) and third (modes (19) and (20)) axial order.

Extracted natural frequencies are compared with the corresponding calculated values in Fig. 29. The calculations were performed with the coupled computer code FLUX2-CYLDY3 [4-6]. A trend similar to that in Fig. 16 can be observed also in this case: the overestimation of the natural frequency values of the beam modes and of the shell modes of lower circumferential order as well as the underestimation of the natural frequency values of the shell modes of higher circumferential order.

Critical damping ratios ξ of extracted modes are plotted over the circumferential order ν in Figs. 30 and 31. The diagrams reveal trends similar to that in Figs. 17 and 18: a relatively high damping ratio of the beam modes and the decrease of ξ with increasing circumferential order. However, the comparison of the damping behaviour observed in both series (with or without the water charge in the reactor pressure vessel) reveals several substantial deviations. A first contradiction can be found by the comparison

of the damping values of the first doublet (fundamental beam mode first axial order) in Tables 2 and 3. Table 2 shows approximately equal values $\xi = 1.48$ and 1.37 %. By contrast, Table 3 gives the values $\xi = 1.53$ and 0.43, resulting in a ratio greater than 3.5. This contradiction can be explained only when the possibility of the vibration energy flow from one mode to another is admitted. Another hint in the same direction is supplied by the unsteadiness of the ξ -values of one mode during the response decay. This phenomenon is illustrated in Figs. 32 and 33.

Fig. 32 presents two time history plots. The upper one shows the time history of displacement, measured approximately at the lower third of the core barrel shell (KS = 1024, Z = 5550 mm, $\psi = 120^\circ$), the lower one shows the time history of acceleration, measured at the bottom of the core barrel (KS 1202, Z = 2750 mm, $\psi = 110^\circ$). The upper diagram is extraordinarily informative. It shows that in the first two seconds of the transient primarily the contribution of the fundamental beam mode can be observed (the frequency of approx. 6.5 Hz can be directly taken from the diagram). In the following time interval the energy dissipation rate of the fundamental mode changes and the contribution of another mode with the natural frequency of approx. 13 Hz develops. At the final stage of the transient the contribution of the 13 Hz-mode predominates which leads to a doubling of the frequency of the transient. The diagram which shows the acceleration signal of the same process is not so informative as the upper one, due to the overlapping of contributions of higher modes distorting the basic signal. To extract more information about the process above, an additional analysis of two displacement signals was performed in more detail; the results are shown in Fig. 33. The whole record of the displacement signals KS 1024 (specified above) and KS 1028 (Z = 4100 mm, $\psi = 120^\circ$) was divided into several subintervals, each 4 sec long, with variable starting points t_0 on the time axis, and the corresponding initial displacement amplitudes $S_{rn}(t_0)$ were plotted on semi-logarithmic coordinates over t_0 . For this evaluation the subroutines EIGEST and AMPLIT1 were used, yielding the simple $S_{rn}(t_0)$ values (no doublets). It was found that the primary contributions to the transient result from the fundamental beam mode with the natural frequency of 6.48 Hz and from the shell mode first axial and second circumferential order with the natural frequency of 12.98 Hz; the corresponding $S_{rn}(t_0)$ values are plotted in Fig. 33. The application of the basic equation (4.1) in this diagram requires that all individual $S_{rn}(t_0)$ -values referring to r and n fixed (one signal and one mode) can be approximated by

a straight line whose slope is directly proportional to the damping ratio ξ_n . Fig. 33 shows that this requirement is only partly satisfied. In the case of the fundamental beam mode (6.48 Hz) the requirement above is fulfilled in the time interval $1 < t_0 < 15$ sec; the points corresponding to the first second of the transient lay beneath the straight approximation line. In the case of the shell mode (12.98 Hz) the time interval where the requirement above is fulfilled is reduced to $8 < t_0 < 15$ sec. For $t_0 < 8$ sec the slope of the approximation line considerably changes with t_0 and for $t_0 < 5$ sec it reaches even negative values. This suggests that the shell mode first axial and second circumferential order in the time interval $0 < t_0 < 5$ sec accepts more energy than it dissipates. In other words, some excitation energy transfer mechanism must be present in the coupled fluid/structure system. One possible theoretical explanation of this phenomenon is described in [13].

The occurrence in the system of the mechanism of excitation energy transfer after initiation of the transient contradicts the linear theoretical model which is used as a basis for the computer code EVA (see Section 4). Nevertheless, the comparison of the original with the reconstructed input signals demonstrates the usefulness of the modal data extracted with this code. Two typical examples supporting this claim are presented in Figs. 34 and 35. These diagrams are laid out similar to those presented in Figs. 19 and 20. The diagrams of $|\hat{X}(t)|$ presented on the right side demonstrate the good agreement between moduli of the Fourier transform calculated from original and reconstructed signals, respectively. The corresponding diagrams in Fig. 34 show that in snapback test No V59.2.3 the maximal energy is concentrated in the shell mode first axial and second circumferential orders, participating in the nonlinear energy transfer postulated above. This circumstance makes the reconstructed signal very sensitive to possible inaccuracies obtained by the extraction of the modal characteristics of this particular mode. However, the fully acceptable agreement between the two time history plots on the left side of Fig. 34 demonstrates that the correct system identification was achieved also in this difficult case. In the less difficult case of the snapback test No V59.4.3, illustrated in Fig. 35, the quality of the system identification attained is comparable with those achieved in the case of a simple, non-coupled system without water charge (test No V59.3.4, Fig. 20).

6. Concluding remarks

The combined experimental-computational procedure described in this report provides means of extracting from transient decay signals the eigenfrequencies, the mode shapes, and the critical damping ratios of linear systems. Its application to the HDR-core barrel mockup yielded the identification of 76 eigenmodes (44 + 32). Several of them turned out to be multiple modes (preferable doublets) with equal axial and circumferential orders but different eigenfrequencies, damping ratios and orientations in space. The smallest identified eigenfrequency difference of one doublet illustrating the resolution capability of the procedure equals 1.5 ‰.

The procedure is based on the quasi-automatic evaluation of simultaneously measured free vibration response signals of the system studied; the nature of the transient excitation used is not subjected to any restrictions. It can therefore be applied in many practical tasks where conventional procedures of experimental modal analysis are not feasible, e.g. in hostile environments and poorly accessible systems. The experience obtained during evaluation of the snapback test No. V59.2.3 indicates that it is applicable also to slightly non-linear systems.

The snapback test series treated in this report provides no means of checking the limitations of applicability of the procedure, imposed by rather large nonlinearities. Some information on this feature is expected from another experimental series performed under laboratory conditions, where two conventional methods of modal analysis could be used as well. The evaluation of this laboratory test series is underway.

References

- [1] Wolf, L., Schumann, U., Scholl, K.H.: Experimental and analytical results of coupled fluid-structure-interactions during blowdown of the HDR-vessel. Trans. of the 6th SMIRT Conf., Paris, 17-21 August 1981, Paper B2/1
- [2] Eberle, F., Erb, E., Kadlec, J., Philipp, P., Wolf, E.: HDR snapback experiments. Trans. of the 6th SMIRT Conf., Paris, 17-21 August 1981, Paper B3/1
- [3] Eberle, F., Kadlec, J.: Erfahrungen aus der modalanalytischen Auswertung von Snapback-Versuchen. VDI-Bericht Nr. 419, 1981, Page 39-45
- [4] Ludwig, A., Schumann, U.: Fluid-structure analysis for the HDR blowdown and snapback experiments with FLUX. To be published in Nuclear Engineering and Design 1982
- [5] Ludwig, A., Krieg, R.: An analytical quasi-exact method for calculating eigenvibrations of thin circular cylindrical shells. Journal of Sound and Vibration 74, 2, 155-174, 1981
- [6] Schumann, U.: Fluid-structure interactions in a pressurized water reactor vessel. E. Absi et al. (Eds.): Numerical Methods for Engineering, Dunod Techn., Paris (1980), Page 123-135
- [7] Appelt, K.D., Eberle, F., Lang, G., Kadlec, J., Philipp, P.: Qualifizierung der Meßinstrumentierung für die Schwingungsuntersuchungen unter Blowdown-Bedingungen. KTG-Fachtagung Experimentiertechnik auf dem Gebiet der Thermo- und Fluidodynamik, Teil 3: Schwingungs- und Geräuschmeßtechnik, Garching, 6.-8.3.1979
- [8] Belytschko, T., Schumann, U.: Fluid-structure interaction in light water reactor systems. Nucl. Engng. Design, 60, 173-195, 1980

- [9] Mnev, E.N., Percev, A.K.: Gridrouprugost' oboloček. Sudostroenie, Leningrad, 1970. English translation: Hydroelasticity of shells, Foreign Technology Division, USAF, FTD-MT-24-119-71 (1971)
- [10] MacFarlane, A.G.J.: Analyse technischer Systeme, Bibliographisches Institut Mannheim, Hochschultaschenbücher-Verlag, 1967
- [11] Procedure Library-Mathematics (PL-Mth) Program Description, Program No. 5734-XM3, IBM Corp., Techn. Publ. Dept., NY, Sept. 1971
- [12] Strobel, H.: Experimentelle Systemanalyse. Akademie-Verlag, Berlin, 1975 (Kapitel 9)
- [13] Ludwig, A., et al.: HDR-Blowdown-Versuche zur dynamischen Beanspruchung von Reaktoreinbauten. Projekt Nukleare Sicherheit, Jahresbericht 1981, KfK 3250, Kernforschungszentrum Karlsruhe, Juni 1982

Appendix

A1. Derivation of the theoretical mean spectral density function $SD(\omega)$

For the derivation of the theoretical mean spectral density function $SD(\omega)$ intended to be set equal to the experimental mean spectral density function $SD(\omega_k)$ we shall use the equivalent of Eq. (4.7)

$$SD(\omega)R = \sum_{r=1}^R \hat{x}_r(\omega) \bar{\hat{x}}_r(\omega) g_r \quad (A1.1)$$

and the Fourier transform of the theoretical response signal $x(t)$ according to Eq. (4.4). The assumption $\exp[(\lambda_n - i\omega)T_m] = 0$ reduces Eq. (4.4) to the form

$$\hat{x}_r(\omega) = \sum_{n=1}^{2N} \frac{C_{rn}}{i\omega - \lambda_n} \quad (A1.2)$$

and

$$\bar{\hat{x}}_r(\omega) = \sum_{n=1}^{2N} \frac{-\bar{C}_{rn}}{i\omega + \bar{\lambda}_n} \quad (A1.3)$$

allowing to rewrite Eq. (A1.1) as

$$SD(\omega)R = \sum_{r=1}^R \sum_{n=1}^{2N} \sum_{m=1}^{2N} \frac{-C_{rn} \bar{C}_{rm} g_r}{(i\omega - \lambda_n)(i\omega + \bar{\lambda}_m)} \quad (A1.4)$$

Let us further suppose that $\alpha_n = -\alpha_0 - \xi_n \omega_n$ is always negative,

$$\alpha_n = -\alpha_0 - \xi_n \omega_n < 0 \quad (A1.5)$$

for $n = 1, 2, \dots, 2N$. This assumption leads to the automatic fulfillment of the condition

$$\lambda_n + \bar{\lambda}_m \neq 0 \quad (A1.6)$$

for all $n, m = 1, 2, \dots, 2N$ allowing us to expand Eq. (1.4) into the sum of partial fractions

$$\begin{aligned}
 SD(\omega)R &= \sum_{r=1}^R \sum_{n=1}^{2N} \sum_{m=1}^{2N} \left[\frac{-C_{rn} \bar{C}_{rm} g_r}{(i\omega - \lambda_n)(\lambda_n + \bar{\lambda}_m)} + \frac{C_{rn} \bar{C}_{rm} g_r}{(i\omega + \bar{\lambda}_m)(\lambda_n + \bar{\lambda}_m)} \right] = \\
 &= \sum_{n=1}^{2N} \sum_{r=1}^R \sum_{m=1}^{2N} \frac{-C_{rn} \bar{C}_{rm} g_r}{(i\omega - \lambda_n)(\lambda_n + \bar{\lambda}_m)} + \\
 &+ \sum_{m=1}^{2N} \sum_{r=1}^R \sum_{n=1}^{2N} \frac{\bar{C}_{rm} C_{rn} g_r}{(i\omega + \bar{\lambda}_m)(\lambda_n + \bar{\lambda}_m)} = \\
 &= \sum_{n=1}^{2N} \frac{-a_n}{i\omega - \lambda_n} + \sum_{m=1}^{2N} \frac{\bar{a}_m}{i\omega + \bar{\lambda}_m} = \sum_{n=1}^{2N} \left[\frac{-a_n}{i\omega - \lambda_n} + \frac{\bar{a}_n}{i\omega + \bar{\lambda}_n} \right] = \\
 &= \sum_{n=1}^{2N} \frac{-a_n(i\omega + \bar{\lambda}_n) + \bar{a}_n(i\omega - \lambda_n)}{(i\omega - \lambda_n)(i\omega + \bar{\lambda}_n)} \tag{A1.7}
 \end{aligned}$$

with

$$a_n = \sum_{r=1}^R \sum_{m=1}^{2N} \frac{C_{rn} \bar{C}_{rm} g_r}{\lambda_n + \bar{\lambda}_m} \tag{A1.8}$$

and

$$\bar{a}_m = \sum_{r=1}^R \sum_{n=1}^{2N} \frac{\bar{C}_{rm} C_{rn} g_r}{\lambda_n + \bar{\lambda}_m} \tag{A1.9}$$

The sum of $2N$ terms on the right side of Eq. (A1.7) can be rearranged into a sum of N double-terms using the conjugate complex features of eigenvalues λ_n defined by Eq. (4.2) and (4.3). From these two equations immediately follow the relations

$$\lambda_{N+n} = \alpha_n - i\Omega_n = \overline{\lambda_n} \quad (\text{A1.10})$$

and

$$\overline{\lambda_{N+n}} = \alpha_n + i\Omega_n = \lambda_n \quad (\text{A1.11})$$

for $n = 1, 2, \dots, N$. To simplify a little the derivations below, let us pick out the n -th and the $N + n$ -th terms from Eq. (A1.7) for any arbitrary, but fixed $n = 1, 2, \dots, N$. Let us further insert λ_{N+n} and $\overline{\lambda_{N+n}}$ from Eq. (A1.10) and (A1.11), respectively, into the second term. The sum of these two terms can be written as

$$\begin{aligned} & \frac{-a_n(i\omega + \overline{\lambda_n}) + \overline{a_n}(i\omega - \lambda_n)}{(i\omega - \lambda_n)(i\omega + \overline{\lambda_n})} + \frac{-a_{N+n}(i\omega + \lambda_n) + \overline{a_{N+n}}(i\omega - \overline{\lambda_n})}{(i\omega - \overline{\lambda_n})(i\omega + \lambda_n)} = \\ & \frac{-a_n i\omega - a_n \alpha_n + a_n i\Omega_n + \overline{a_n} i\omega - \overline{a_n} \alpha_n - \overline{a_n} i\Omega_n}{(i\omega - \alpha_n - i\Omega_n)(i\omega + \alpha_n - i\Omega_n)} + \\ & \frac{-a_{N+n} i\omega - a_{N+n} \alpha_n - a_{N+n} i\Omega_n + \overline{a_{N+n}} i\omega - \overline{a_{N+n}} \alpha_n + \overline{a_{N+n}} i\Omega_n}{(i\omega - \alpha_n + i\Omega_n)(i\omega + \alpha_n + i\Omega_n)} = \\ & \frac{\alpha_n(-a_n - \overline{a_n}) + i\omega(-a_n + \overline{a_n}) + i\Omega_n(a_n - \overline{a_n})}{[\alpha_n - i(\Omega_n - \omega)][-\alpha_n - i(\Omega_n - \omega)]} + \end{aligned}$$

$$\frac{\alpha_n (-a_{N+n} - \bar{a}_{N+n}) + i\omega (-a_{N+n} + \bar{a}_{N+n}) + i\Omega_n (-a_{N+n} + \bar{a}_{N+n})}{[-\alpha_n + i(\Omega_n + \omega)][\alpha_n + i(\Omega_n + \omega)]} =$$

$$\frac{\alpha_n (a_n + \bar{a}_n) - i(\Omega_n - \omega)(a_n - \bar{a}_n)}{(\Omega_n - \omega)^2 + \alpha_n^2} +$$

$$\frac{\alpha_n (a_{N+n} + \bar{a}_{N+n}) + i(\omega + \Omega_n)(a_{N+n} - \bar{a}_{N+n})}{(\Omega_n + \omega)^2 + \alpha_n^2} \quad (\text{A1.12})$$

When we indicate in Eq. (A1.12)

$$\alpha_n (a_n + \bar{a}_n) = 2\alpha_n \text{Re} \{a_n\} = A_n R,$$

$$\alpha_n (a_{N+n} + \bar{a}_{N+n}) = 2\alpha_n \text{Re} \{a_{N+n}\} = A_{N+n} R$$

and

$$-i(a_n - \bar{a}_n) = -2 \text{Im} \{a_n\} = B_n R$$

$$i(a_{N+n} - \bar{a}_{N+n}) = 2 \text{Im} \{a_{N+n}\} = B_{N+n} R$$

} (A1.13)

and introduce the corresponding double-term into Eq. (A1.7), we finally get the theoretical mean spectral density function as a sum of N double-terms

$$SD(\omega) = \sum_{n=1}^N \left[\frac{A_n + B_n (\Omega_n - \omega)}{(\Omega_n - \omega)^2 + \alpha_n^2} + \frac{A_{N+n} + B_{N+n} (\Omega_n + \omega)}{(\Omega_n + \omega)^2} \right] \quad (\text{A1.14})$$

Eq. (A1.14) is identical with Eq. (4.8) used in Paragraph 4.1. The first term in Eq. (A1.4) represents the contribution of the n-th mode, the second the contribution of the corresponding conjugate complex mode. It can be shown that the contributions to the mean spectral density function of the conjugate modes are very small and can therefore be neglected.

A2. Derivation of Eq. (4.44)

To derive the set of $6N'$ linear equations needed to estimate $3N'$ unknown complex coefficients $a_0, a_1, \dots, a_{N'}, b_1, \dots, b_0', b_1', \dots, b_{N'-1}'$ we shall use the integral square of the weighted error according to Eq. (4.42)

$$\begin{aligned} & \sum_{k=S-L}^{S+L} |g_{s,k}|^2 \left| \varepsilon_{s,k} \right|^2 = \sum_{k=S-L}^{S+L} |g_{s,k}|^2 \varepsilon_{s,k} \overline{\varepsilon_{s,k}} = \\ & = \sum_{k=S-L}^{S+L} |g_{s,k}|^2 \left[\underline{Y}_s^T \underline{V}_{s,k} - \underline{1} \right] \left[\overline{V}_{s,k}^T \overline{Y}_s - \underline{1} \right] \end{aligned} \quad (A2.1)$$

One set of linear equations can be obtained via partial differentiation of Eq. (A2.1) with respect to the real part of every element of the matrix

$$\sum_{k=S-L}^{S+L} |g_{s,k}|^2 \left\{ \underline{I} \underline{V}_{s,k} \left[\overline{V}_{s,k}^T \overline{Y}_s - \underline{1} \right] + \left[\underline{Y}_s^T \underline{V}_{s,k} - \underline{1} \right] \overline{V}_{s,k}^T \underline{I} \right\} = \underline{0} \quad (A2.2)$$

where \underline{I} designates $3N' \times 3N'$ unit matrix. Partial differentiation of Eq. (A2.1) with respect to the imaginary part of every element of the matrix \underline{Y}_s yields the second set of linear equations

$$\sum_{k=S-L}^{S+L} |g_{S,k}|^2 \left\{ \underline{\underline{I}} \underline{V}_{S,k} \left[\overline{V}_{S,k}^T \underline{Y}_S^{-1} \right] - \left[Y_S^T \underline{V}_{S,k}^{-1} \right] \overline{V}_{S,k}^T \underline{\underline{I}} \right\} = \underline{0} \quad (\text{A2.3})$$

addition to Eqs. (A2.2) and (A2.3) yields

$$\sum_{k=S-L}^{S+L} |g_{S,k}|^2 \underline{\underline{I}} \underline{V}_{S,k} \left[\overline{V}_{S,k}^T \underline{Y}_S^{-1} \right] = \underline{0} \quad (\text{A2.4})$$

leading to

$$\sum_{k=S-L}^{S+L} |g_{S,k}|^2 \underline{V}_{S,k} \overline{V}_{S,k}^H \underline{Y}_S = \sum_{k=S-L}^{S+L} |g_{S,k}|^2 \underline{V}_{S,k} \quad (\text{A2.5})$$

or

$$\sum_{k=S-L}^{S+L} |g_{S,k}|^2 \overline{\underline{V}_{S,k} \overline{V}_{S,k}^H \underline{Y}_S} = \sum_{k=S-L}^{S+L} |g_{S,k}|^2 \overline{\underline{V}_{S,k}} \quad (\text{A2.6})$$

Eq. (A2.6) is identical with Eq. (4.48).

Mode No.	f [Hz]	ζ [%]	μ	ν	χ_y^2 [%]	Ψ_{y0} [grad]	Test No. v59.	Fig. No.
1	12.36	3.1	0	1	98.4	118	1.4	8
2	15.79	1.48	1	1	83.1	176	1.4	8
3	16.20	1.37	1	1	98.3	120	1.4	8
4	39.03	0.087	1	3	99.2	97	3.4	8
5	39.16	0.050	1	3	99.1	129	3.4	8
6	48.27	0.39	1	2	98.4	133	1.4	3
7	51.76	0.088	1	4	97.8	91	3.4	9
8	52.01	0.087	1	4	98.6	115	3.4	9
9	54.36	0.53	1	2	98.7	134	1.4	9
10	72.53	0.066	2	4	98.2	90	3.4	9
11	72.80	0.081	2	4	99.8	115	3.4	9
12	77.43	0.21	1	2	81.3	137	1.4	9
13	78.92	0.067	1	5	96.5	112	3.4	10
14	80.77	0.21	1	2	94.4	97	1.4	10
15	83.59	0.087	2	3	97.6	102	3.4	10
16	83.99	0.058	2	3	98.2	129	3.4	10
17	88.43	0.095	2	5	97.1	113	3.4	10
18	109.97	0.12	3	5	91.0	110	3.4	10
19	111.15	0.220	3	4	92.0	105	3.4	11
20	113.64	0.055	1	6	96.2	118	3.4	11
21	114.05	0.14	1	6	97.0	106	3.4	11
22	119.22	0.055	2	6	95.1	120	3.4	11
23	119.54	0.069	2	6	99.3	106	3.4	11
24	128.39	0.064	2	2	99.4	104	3.4	12
25	130.01	0.086	2	2	99.0	91	3.4	12
26	132.08	0.051	3	6	95.1	121	3.4	12
27	132.61	0.066	3	6	98.5	106	3.4	12
28	135.03	0.200	2	2	92.4	98	3.4	12
29	135.69	0.150	2	2	98.2	142	3.4	12
30	140.29	0.050	4	5	99.3	96	3.4	13
31	140.74	0.043	4	5	97.5	114	3.4	13
32	146.37	0.14	3	3	98.2	95	3.4	13
33	147.36	0.10	3	3	99.0	123	3.4	13
34	151.26	0.043	4	6	95.8	119	3.4	13
35	151.49	0.035	4	6	96.9	105	3.4	13
36	155.76	0.056	1	7	89.0	111	3.4	14
37	156.41	0.089	1	7	83.5	105	3.4	14
38	157.35	0.19	4	4	98.4	112	3.4	14
39	159.73	0.059	2	7	93.6	116	3.4	14
40	160.02	0.052	2	7	97.7	102	3.4	14
41	168.71	0.045	3	7	95.9	116	3.4	15
42	169.11	0.05	3	7	98.5	102	3.4	15
43	181.56	0.068	4	7	95.7	110	3.4	15
44	202.03	0.11	2.5	2	98.4	93	3.4	15

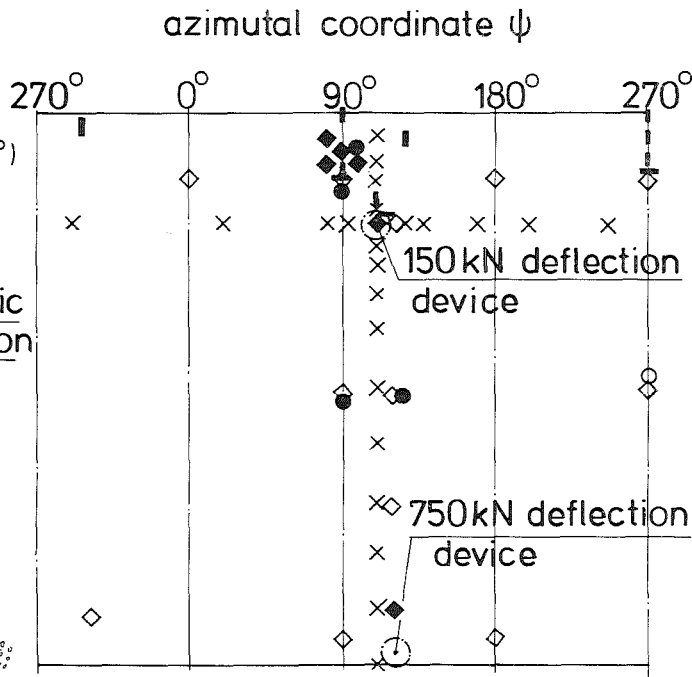
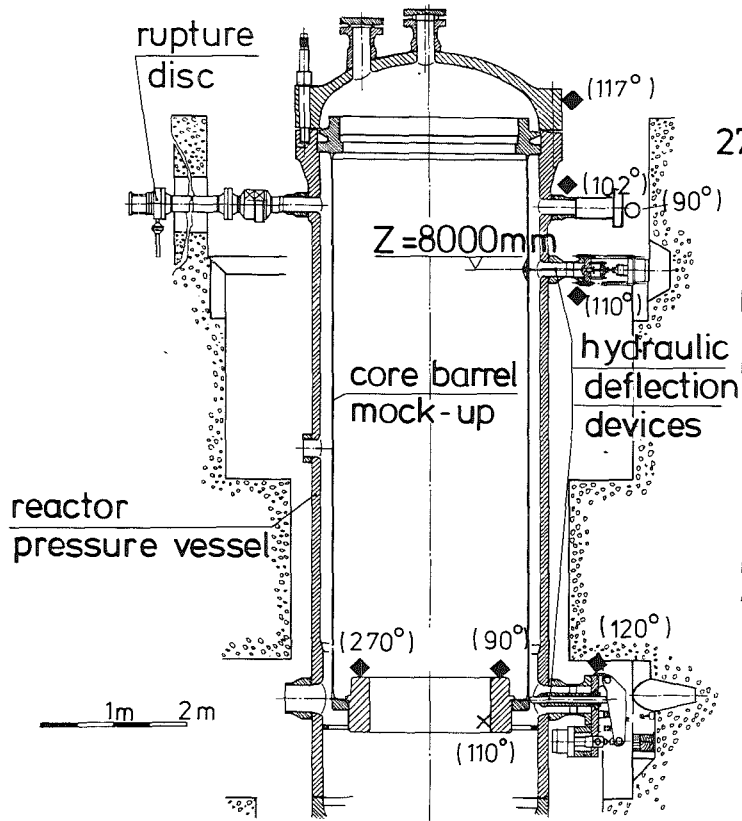
Table 2: Evaluated modal characteristics (reactor pressure vessel empty)

Mode No.	f [Hz]	ζ [%]	μ	ν	γ_y^2 [%]	Ψ_{vo} [grad]	Test No. V59.	Fig. No.
1	6.42	1.5	1	1	98.6	146	2.3	23
2	6.48	0.46	1	1	99.4	117	2.3	23
3	12.66	0.094	1	3	96.2	109	4.3	23
4	12.99	0.14	1	2	94.8	109	4.3	23
5	20.31	0.73	1	4	99.6	110	4.3	23
6	26.58	0.48	2	1	96.1	91	2.3	24
7	26.73	0.24	2	1	99.6	1	2.3	24
8	27.90	0.095	2	3	99.2	107	4.3	24
9	28.92	0.069	2	4	99.9	110	4.3	24
10	32.85	0.34	2	2	99.4	61	2.3	24
11	32.97	0.40	2	2	99.7	106	2.3	24
12	35.28	0.061	1	5	97.2	110	4.3	25
13	40.01	0.083	2	5	98.2	110	4.3	25
14	41.02	0.57	1	2	96.8	50	2.3	25
15	45.35	0.079	3	4	99.9	109	2.3	25
16	49.98	0.094	3	3	84.6	135	2.3	25
17	50.67	0.097	3	5	92.6	112	4.3	25
18	56.57	0.072	1	6	99.5	106	4.3	26
19	57.37	0.45	3	1	91.8	93	2.3	26
20	58.00	0.35	3	1	93.4	166	2.3	26
21	59.71	0.064	2	6	99.8	111	4.3	26
22	60.02	0.19	3	2	97.2	91	2.3	26
23	65.96	0.074	4	5	84.9	119	4.3	27
24	66.18	0.087	4	4	91.1	130	2.3	27
25	66.75	0.11	3	6	99.1	110	4.3	27
26	74.60	0.30	4	3	98.3	116	2.3	27
27	77.43	0.072	4	6	99.2	113	4.3	27
28	79.60	1.1	2	2	81.7	120	2.3	28
29	83.75	0.044	1	7	98.0	106	4.3	28
30	86.29	0.062	2	7	98.2	106	4.3	28
31	91.80	0.10	3	7	98.5	108	4.3	28
32	99.79	0.12	4	7	97.1	109	4.3	28

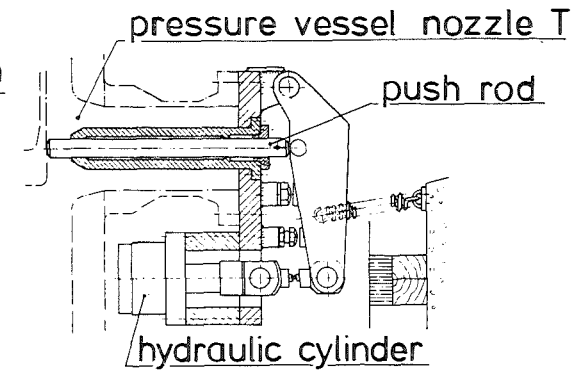
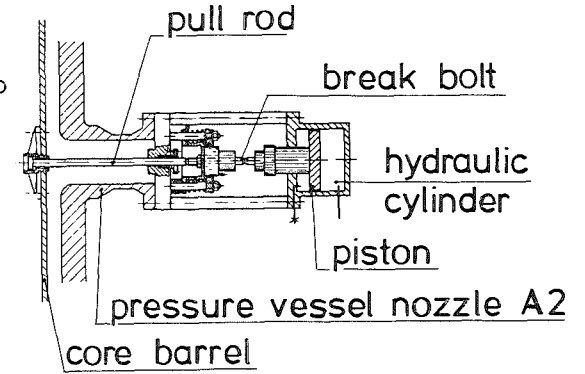
Table 3: Evaluated modal characteristics (reactor pressure vessel filled with water)

developed core barrel shell

150kN deflection device



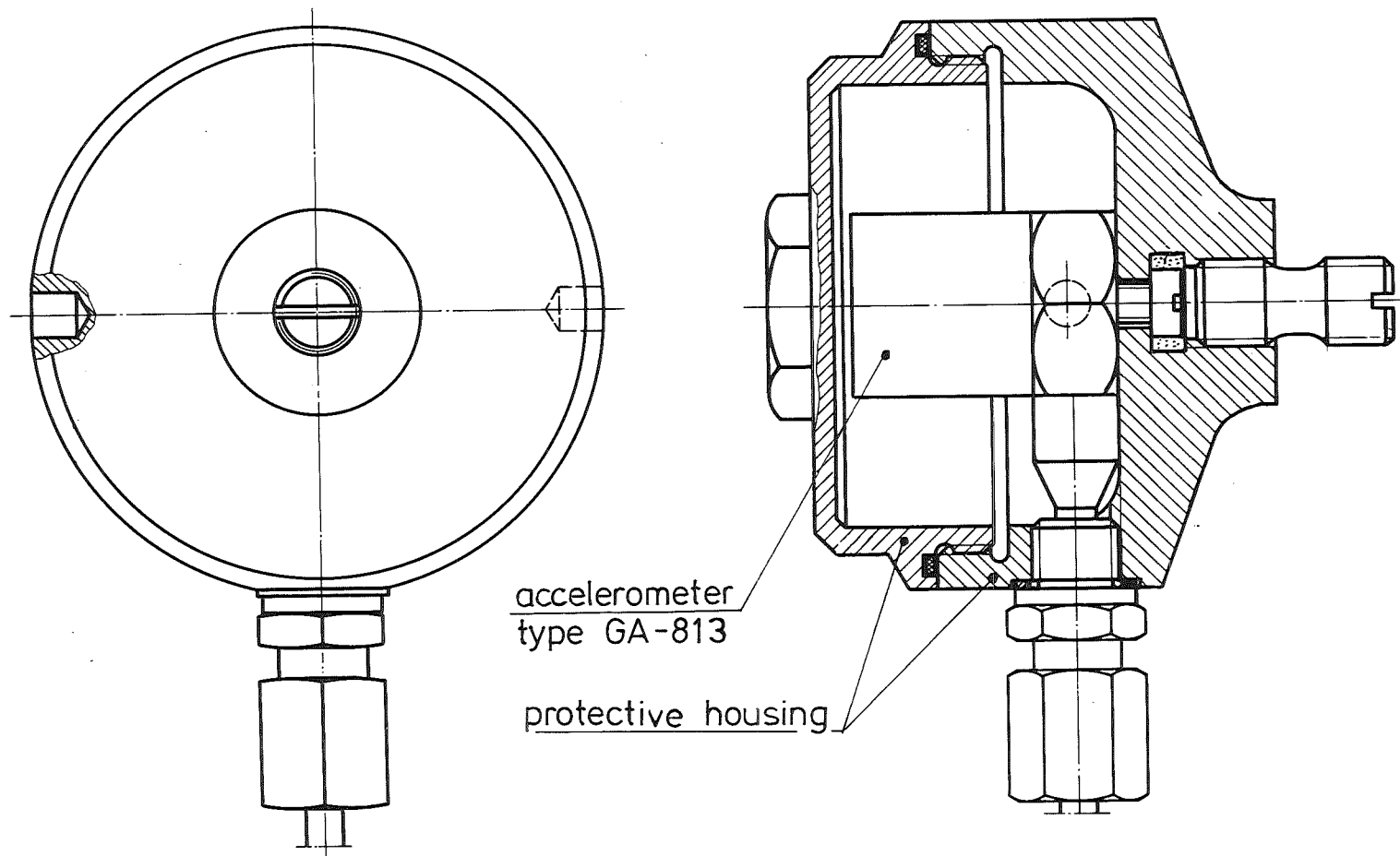
- X piezoresistive accelerometer
- ◆ piezoelectric accelerometer
- ◇ displacement transducer
- absolute pressure transducer
- difference pressure transducer
- I strain gauge vertical
- strain gauge horizontal



750kN deflection device

1
50
1

Fig. 1: Experimental set-up

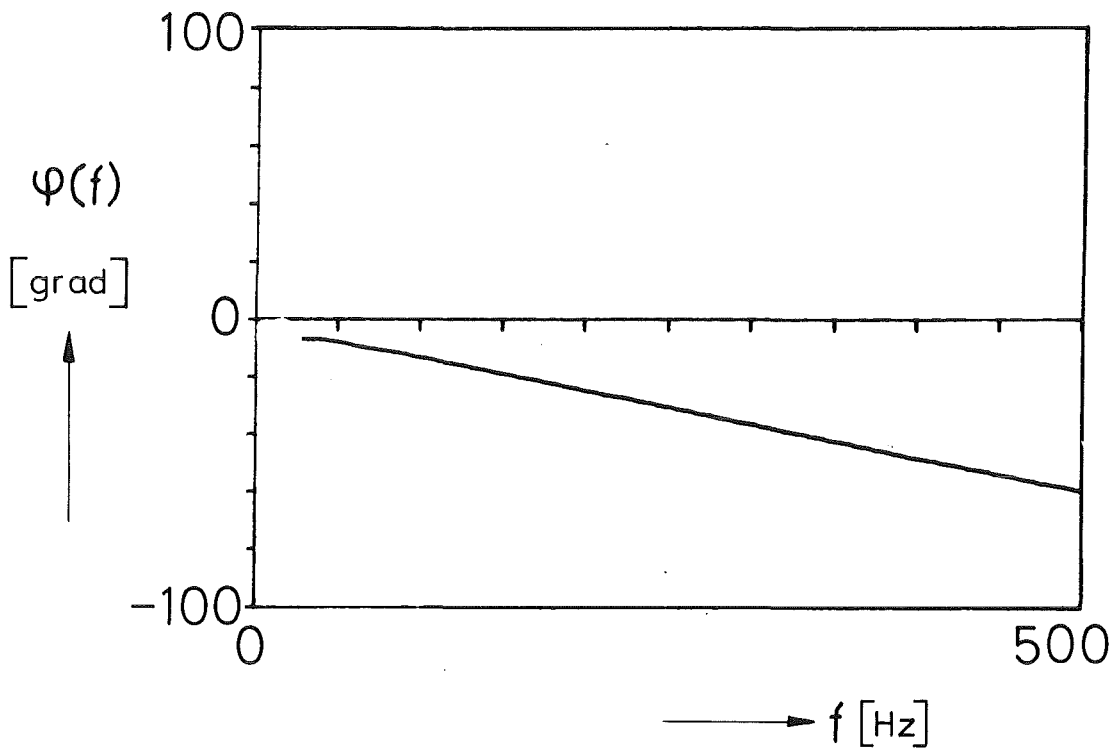
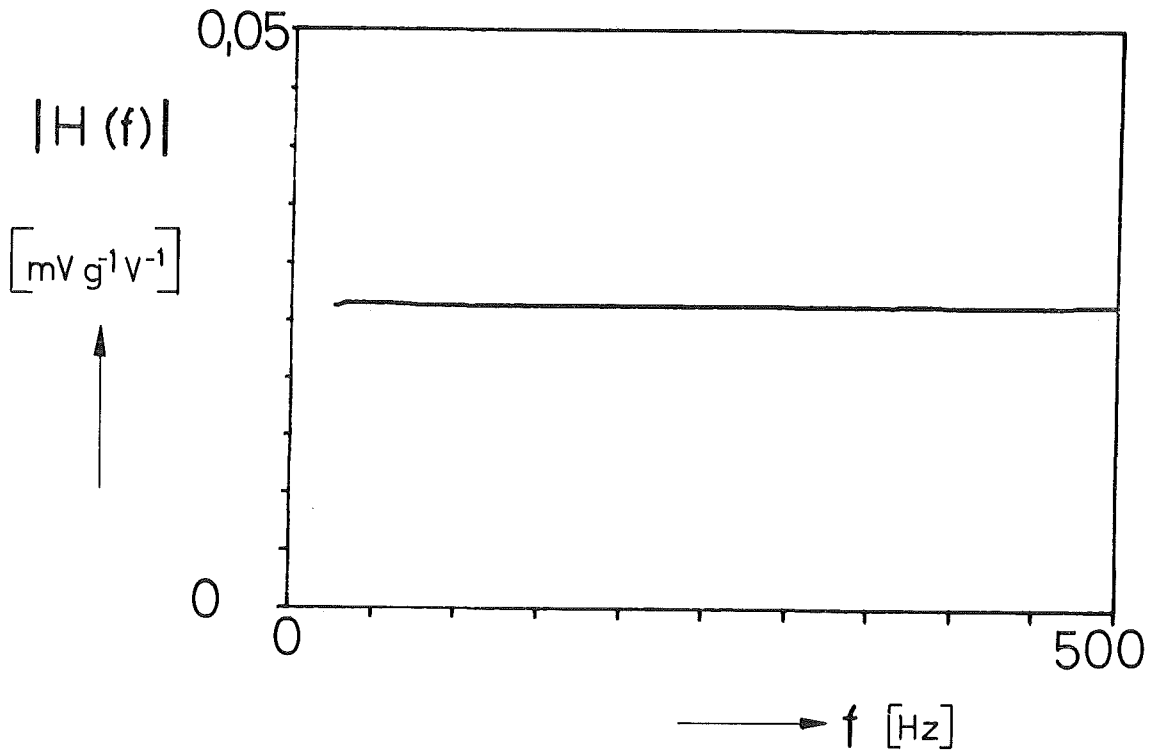


accelerometer
type GA-813

protective housing

KIK
IRE

Fig.2: Accelerometer type GA-813 in protective housing .



KIK
IRE

Fig.3: Frequency response function of the accelerometer type GA-813
(Serien-No. 4332)

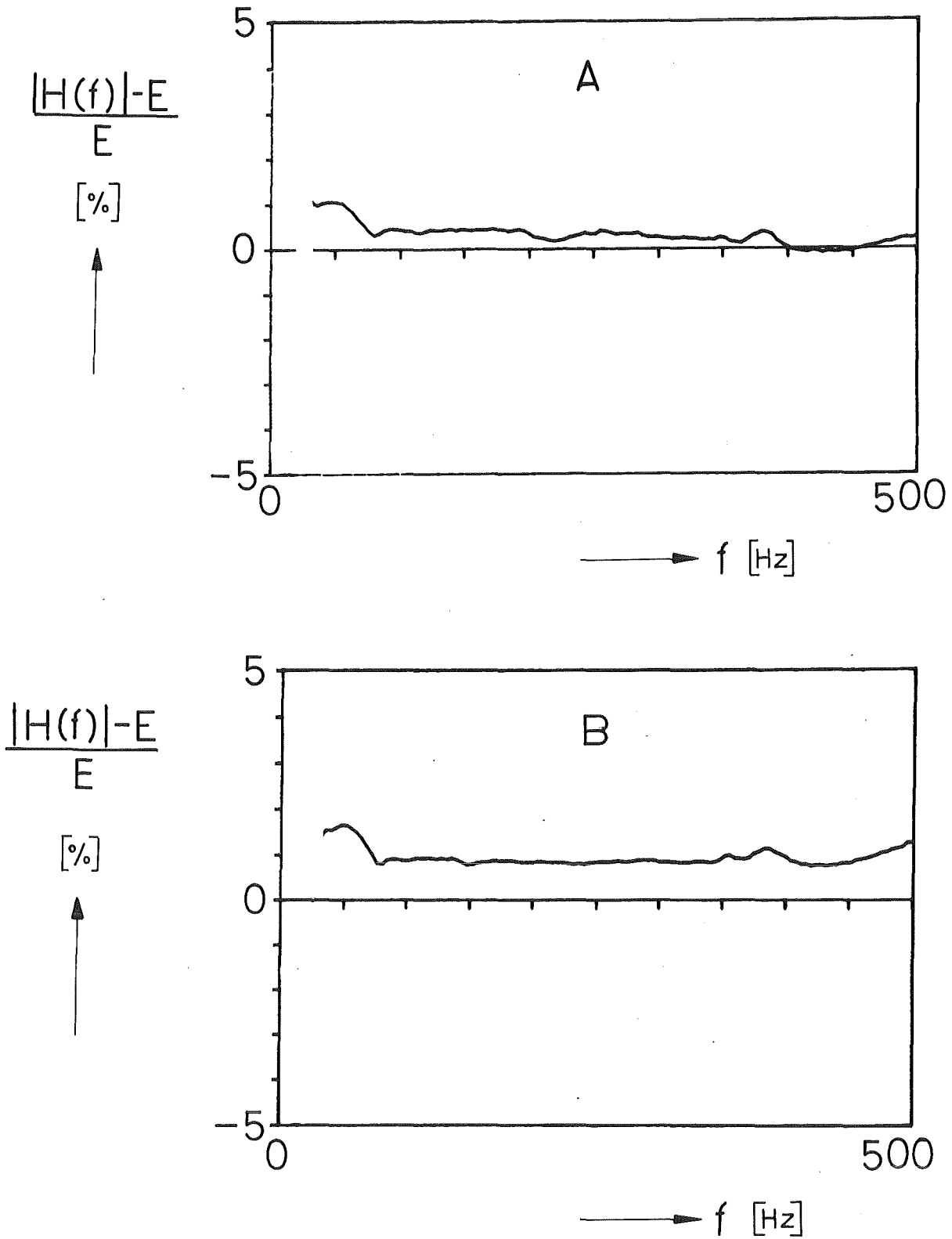


Fig. 4: Deviation of the frequency response function modulus of the accelerometer, serien-No. 4332, from the sensitivity E (B-transducer in the protective housing; A-transducer alone)

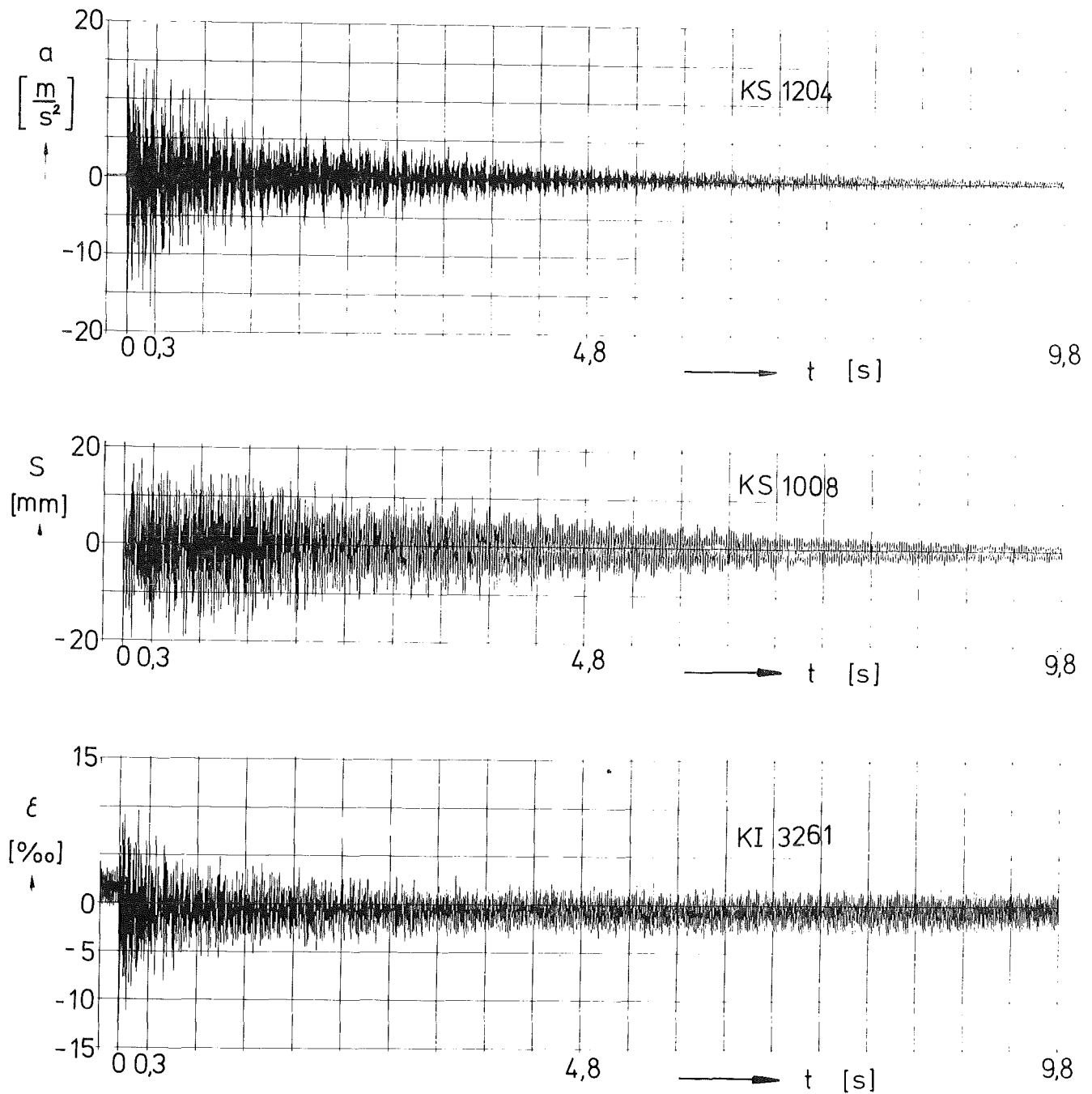


Fig.5: Typical time history plots of the transient acceleration $a(y)$ displacement $y(t)$, and strain $\epsilon(t)$, measured in test No. V59.3.4 (reactor pressure vessel filled with air; 150 kN deflection device).

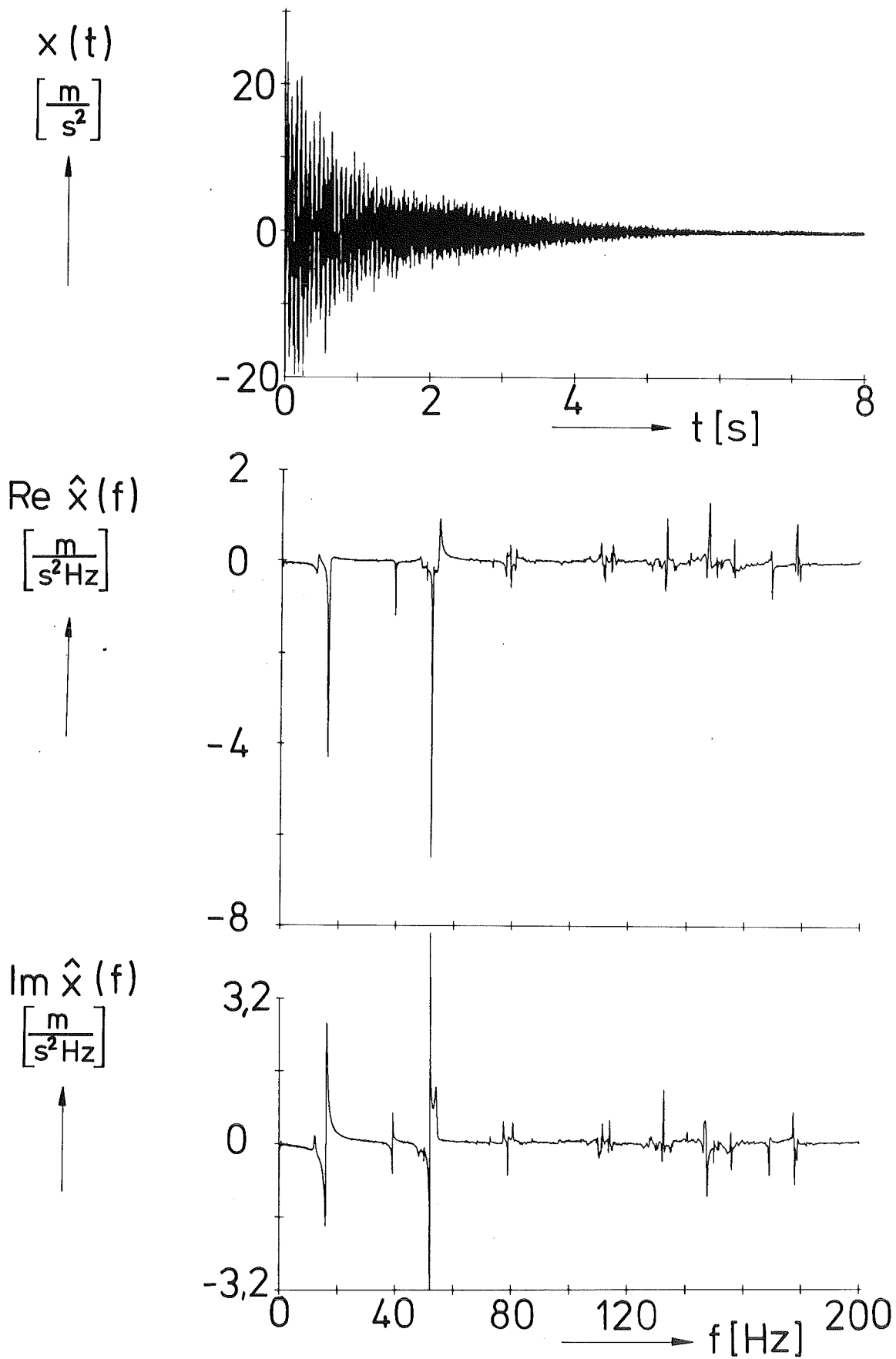


Fig. 6: Typical time history and Fourier-transform of the measured acceleration (KS1206 , test No.V59.1.4)

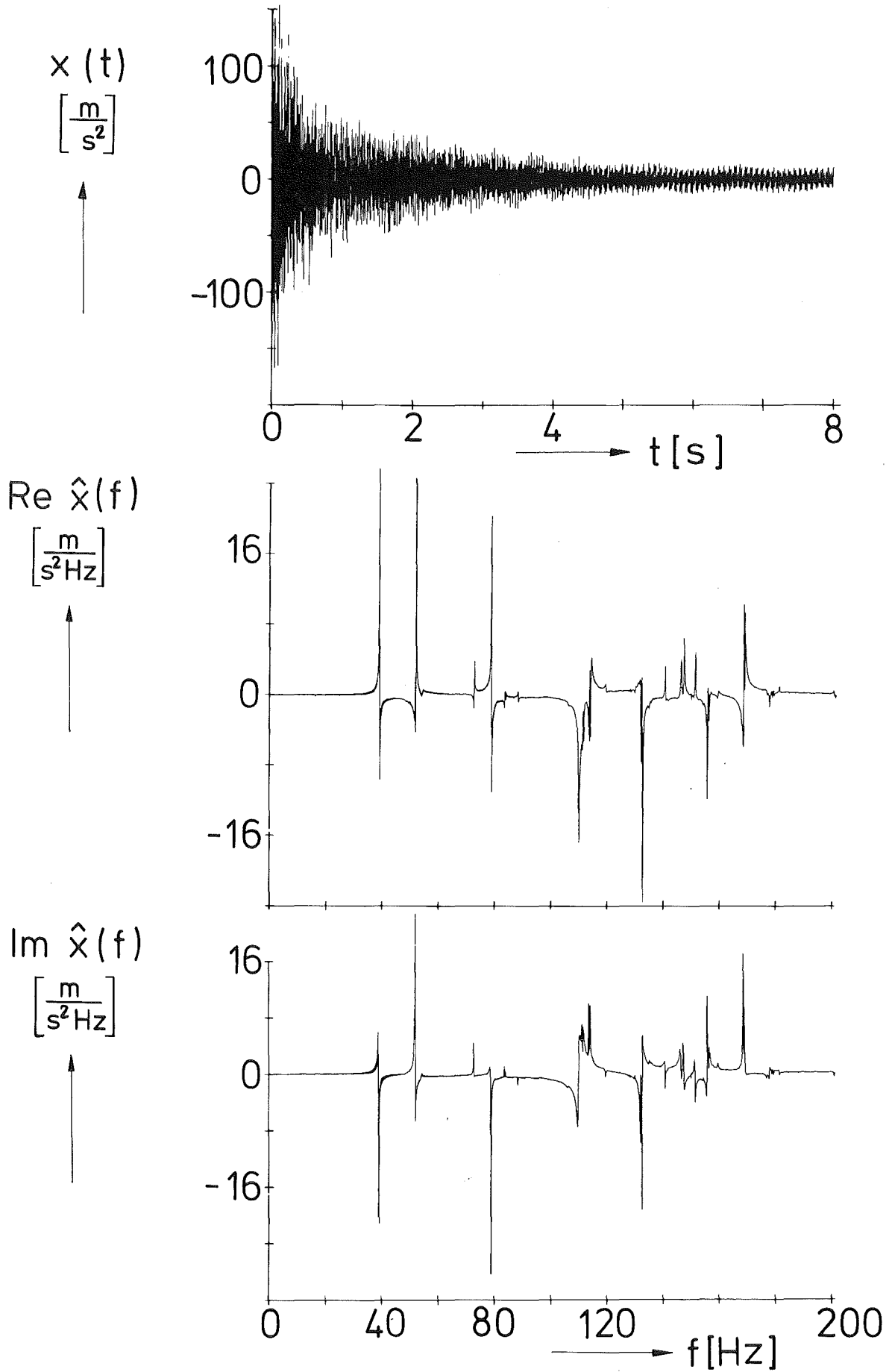


Fig. 7: Typical time history and Fourier-transform of the measured acceleration (KS 1206, test No. V59.3.4)

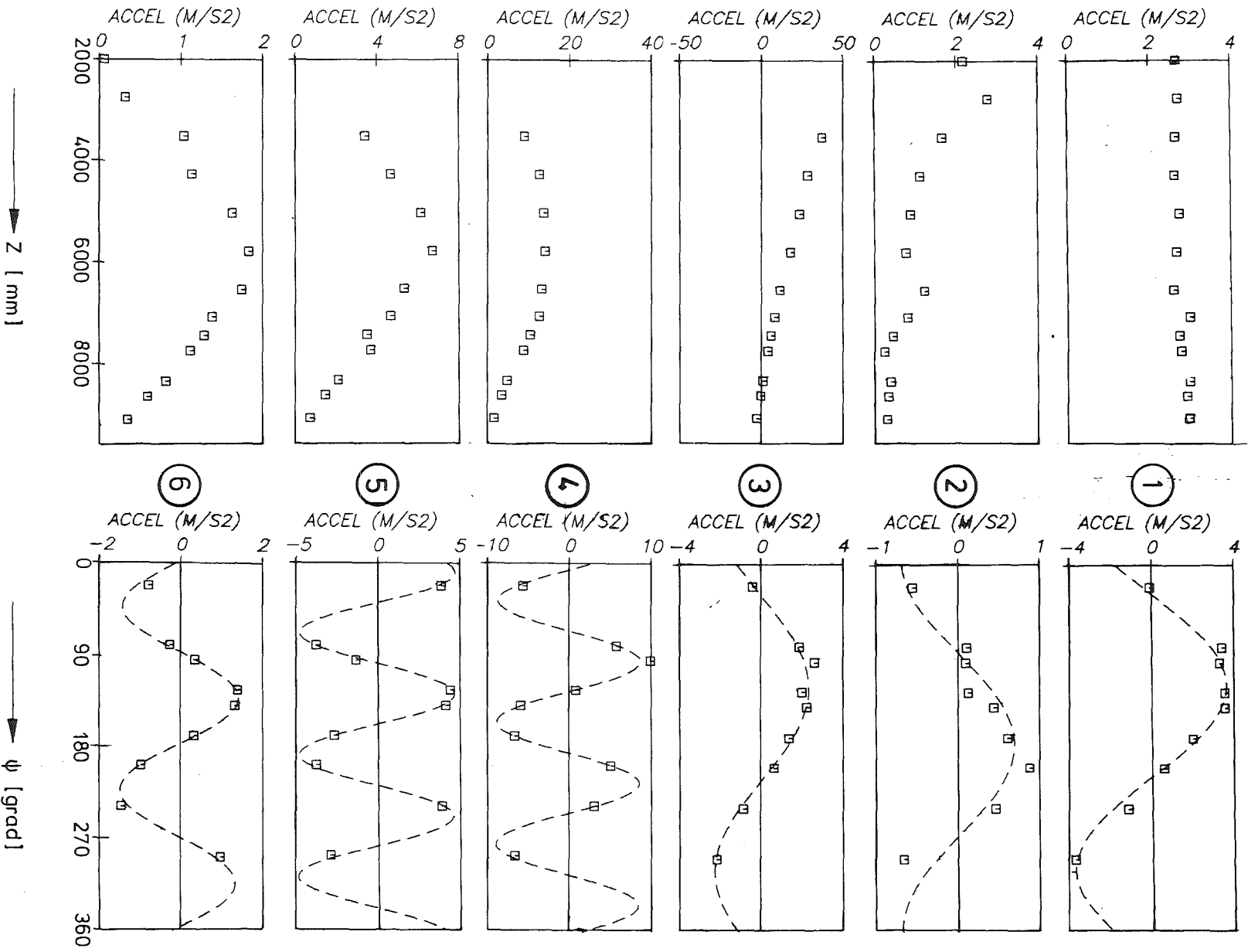


Fig. 8 : Extracted mode shapes of the core barrel mockup (reactor pressure vessel empty)

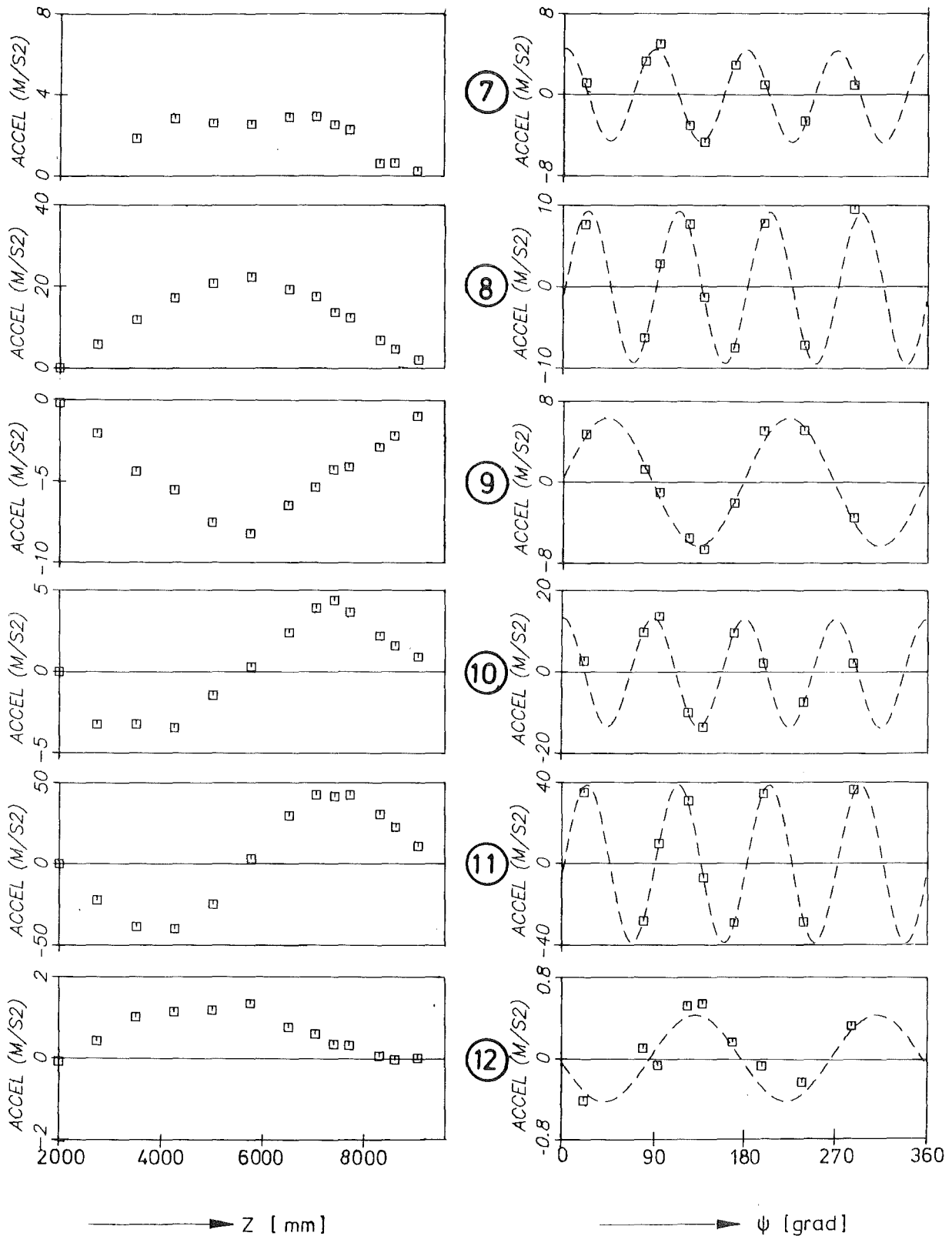


Fig. 9 : Extracted mode shapes of the core barrel mockup (reactor pressure vessel empty)

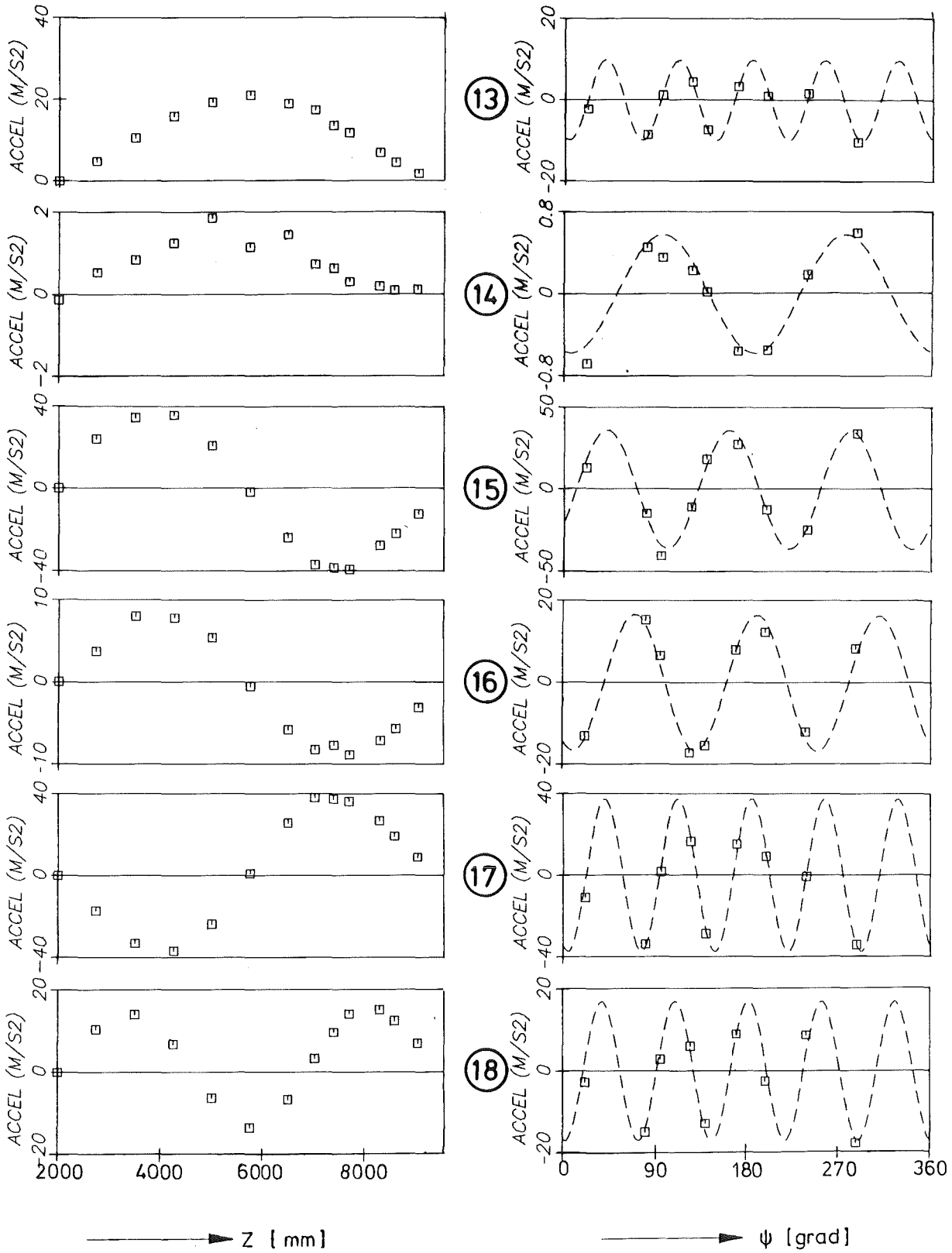


Fig.10: Extracted mode shapes of the core barrel mockup (reactor pressure vessel empty)

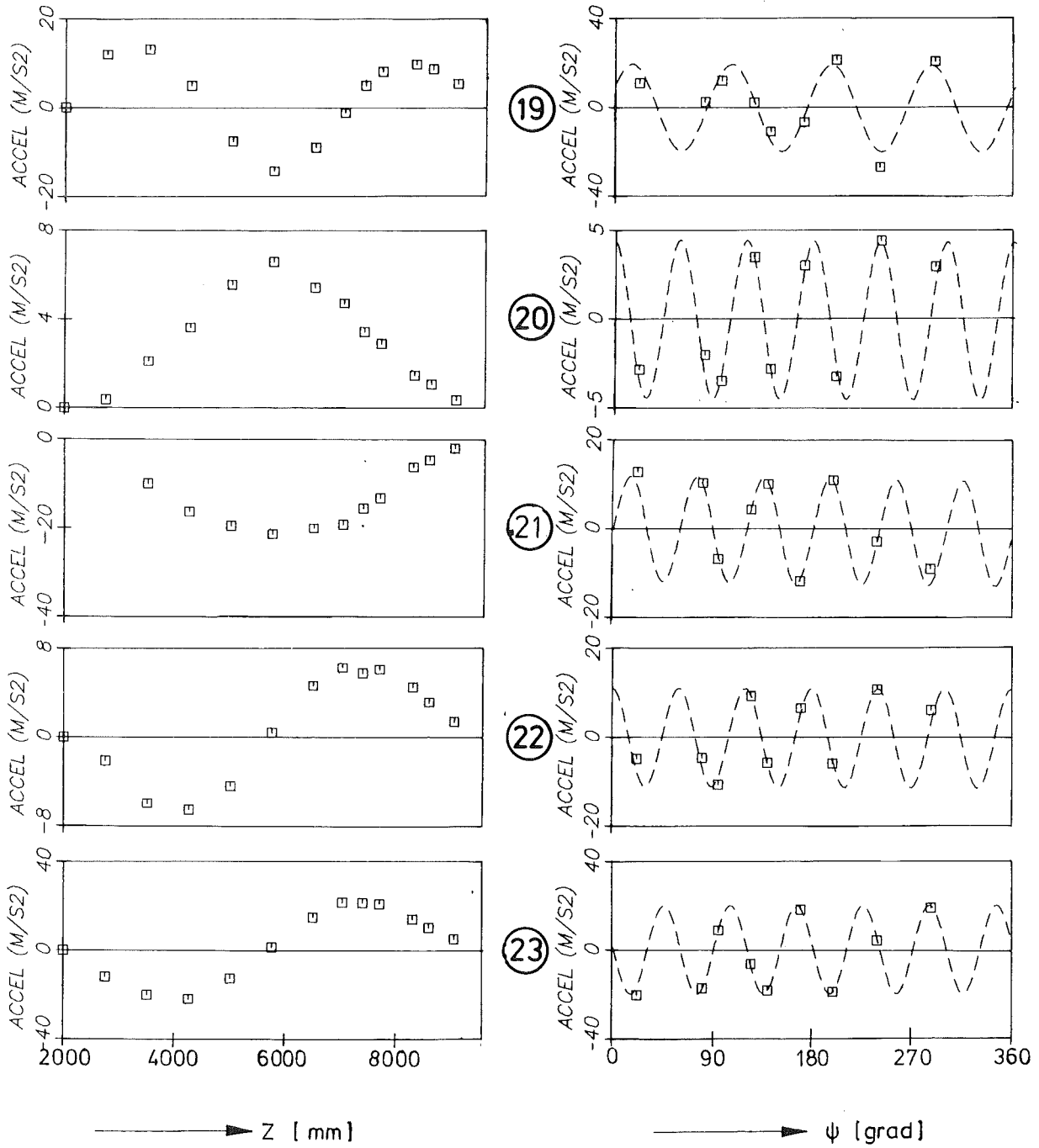


Fig.11: Extracted mode shapes of the core barrel mockup (reactor pressure vessel empty)

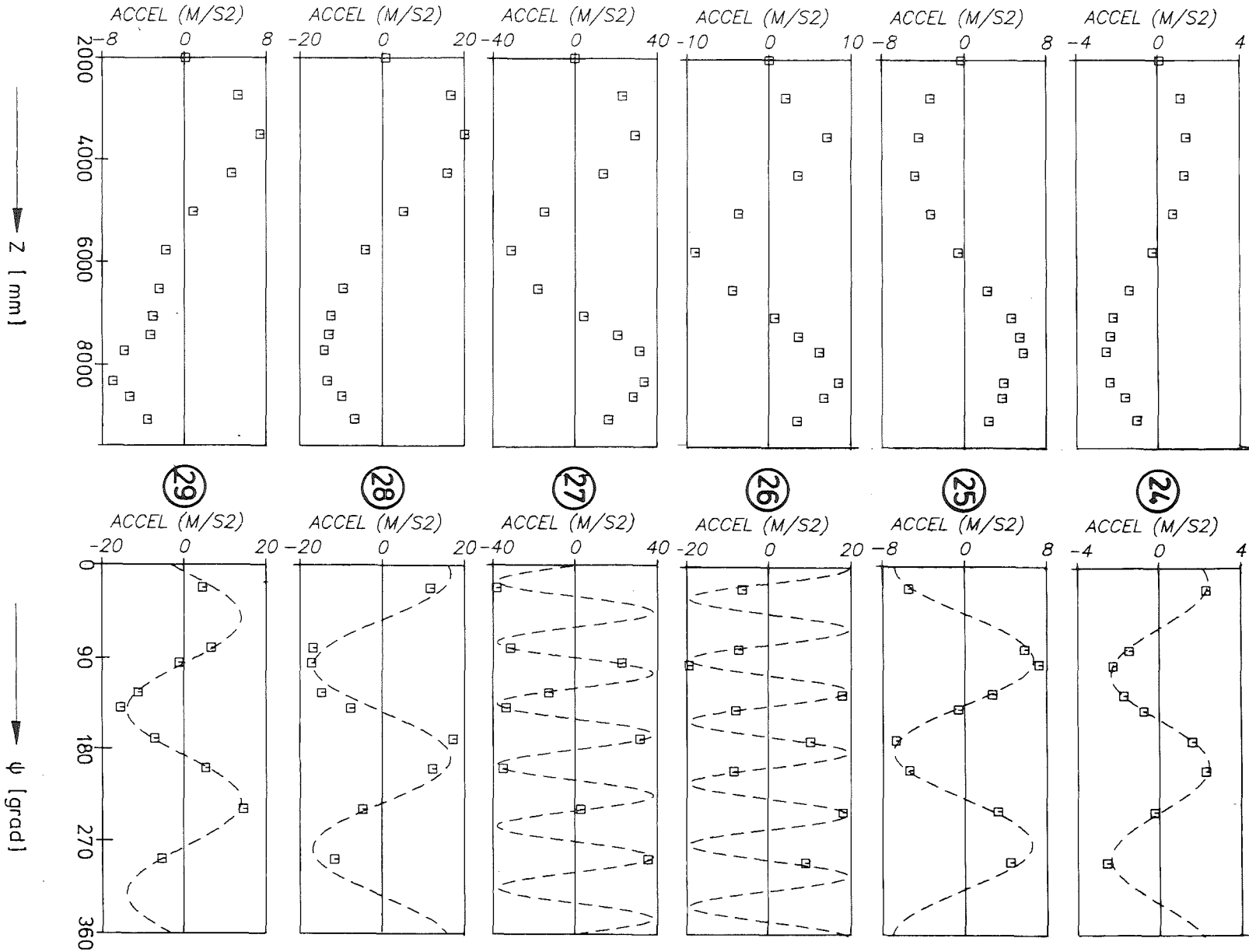


Fig.12: Extracted mode shapes of the core barrel mockup (reactor pressure vessel empty)



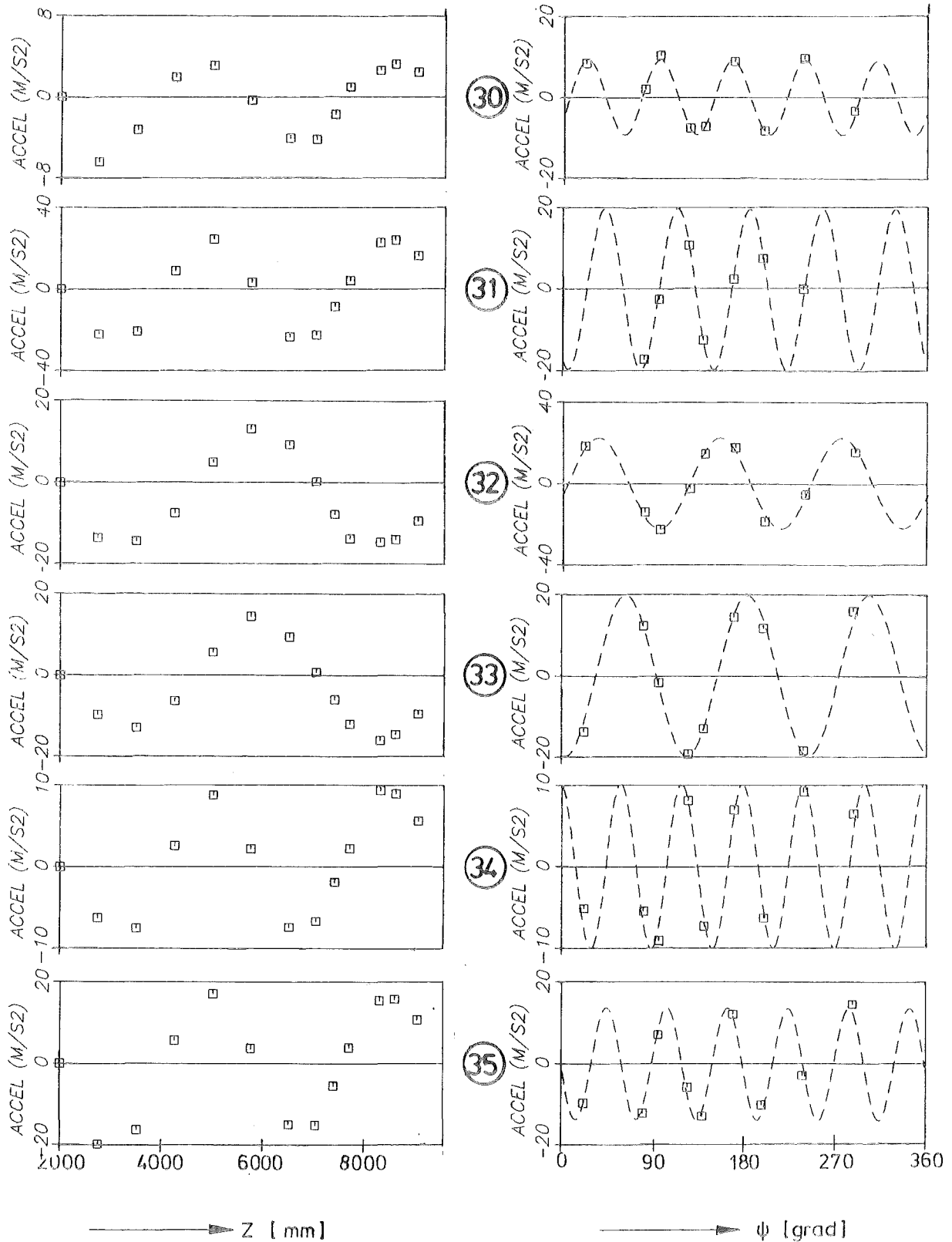


Fig.13: Extracted mode shapes of the core barrel mockup (reactor pressure vessel empty)

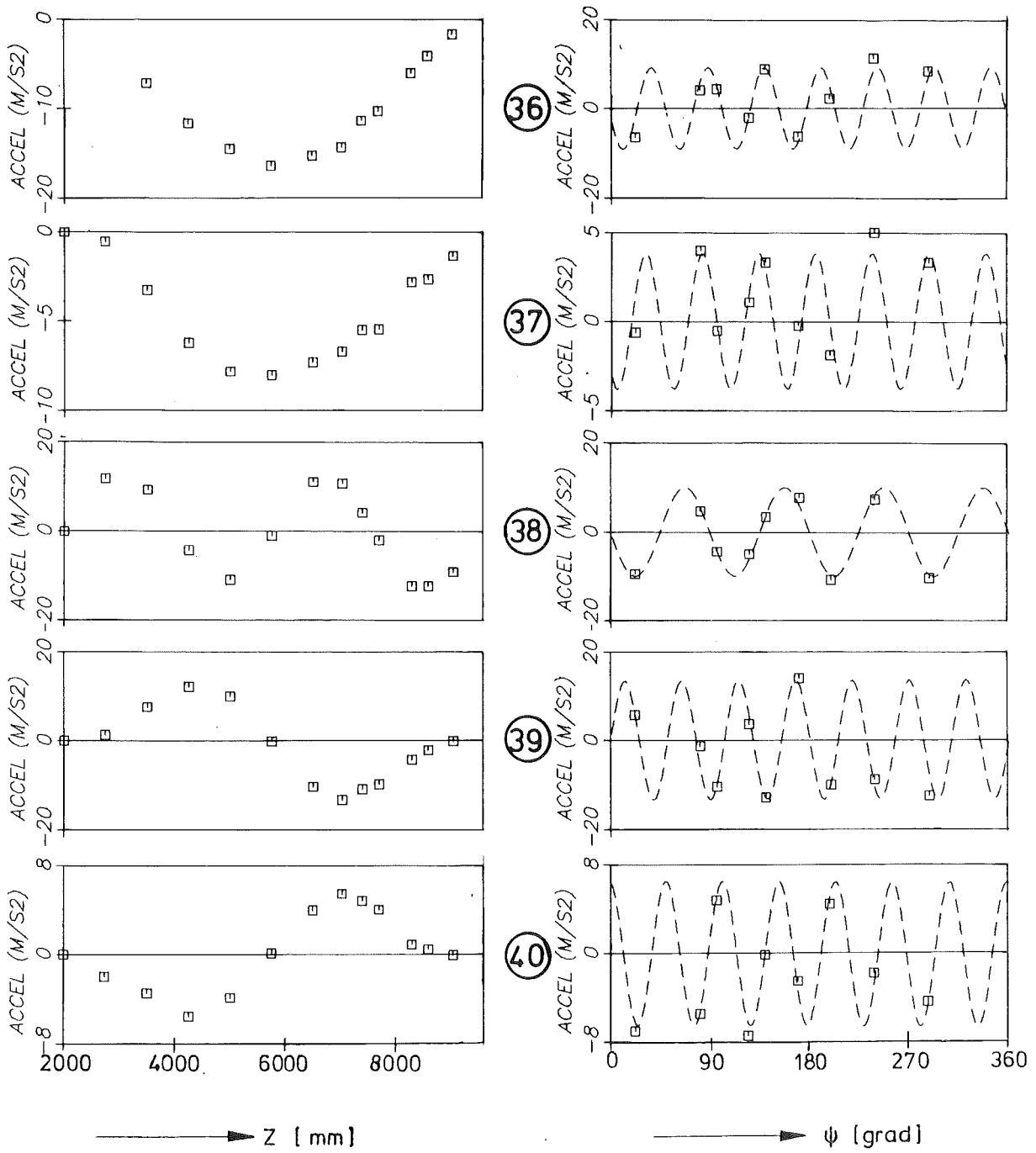


Fig.14: Extracted mode shapes of the core barrel mockup (reactor pressure vessel empty)

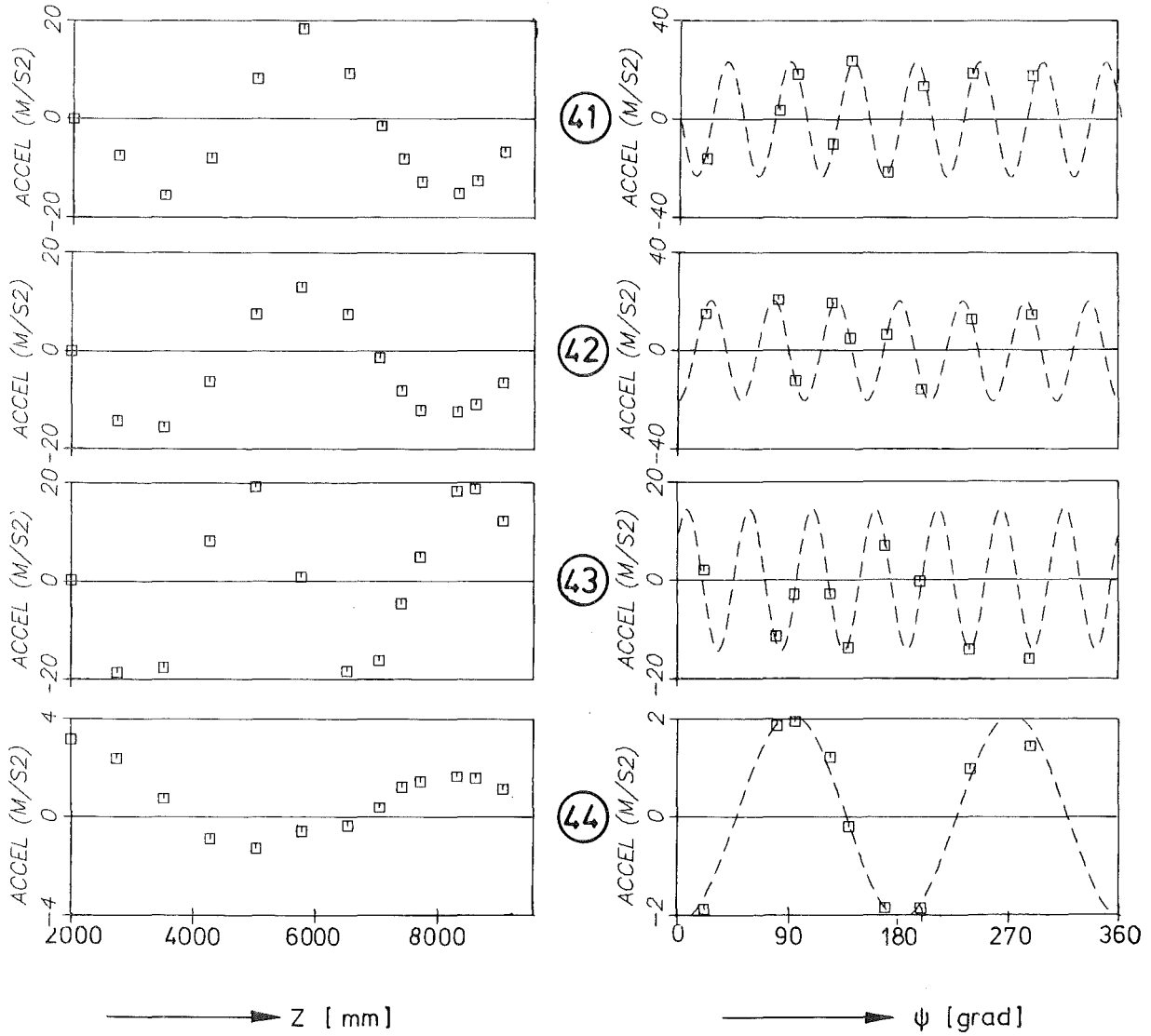


Fig.15: Extracted mode shapes of the core barrel mockup (reactor pressure vessel empty)

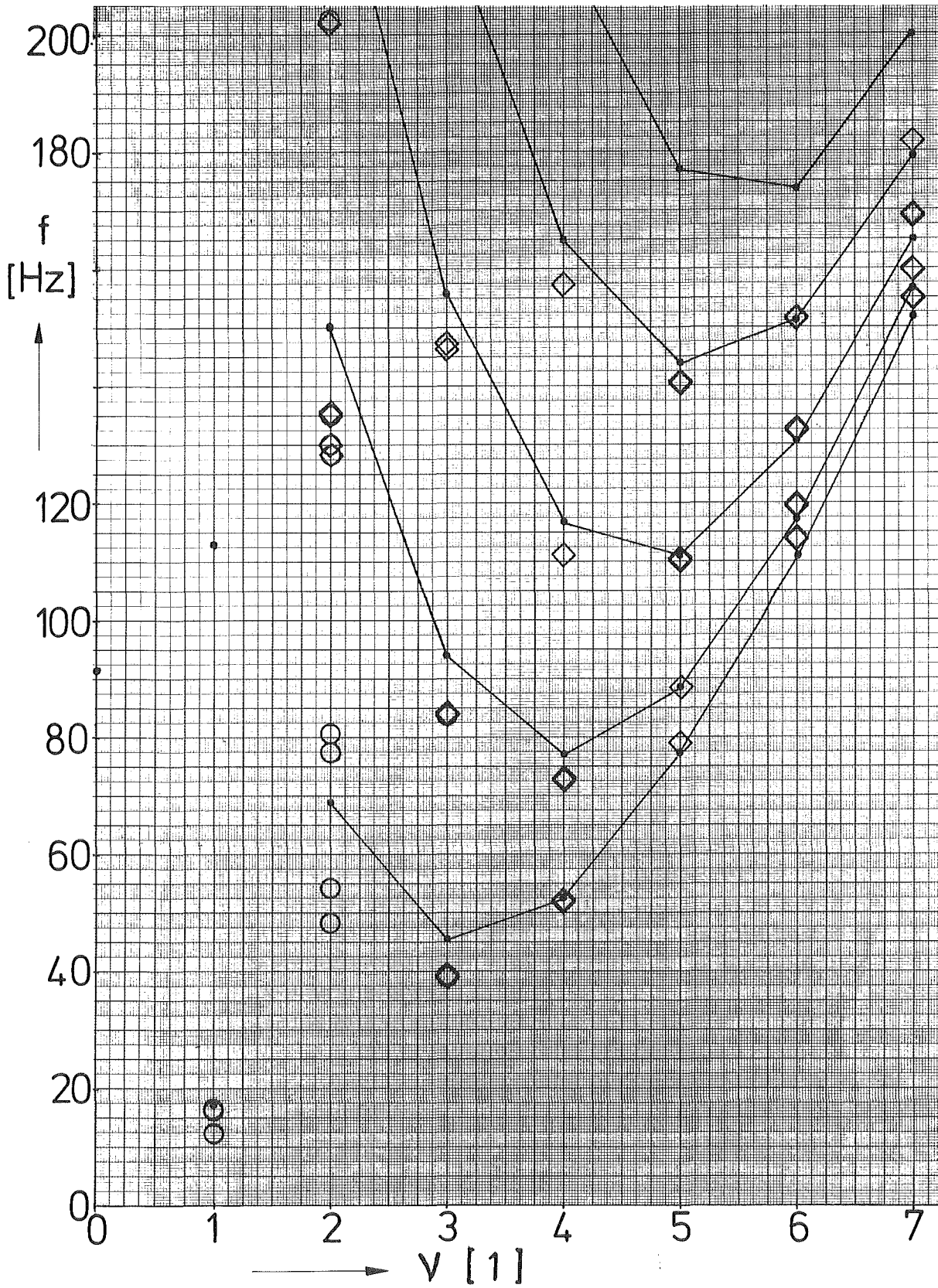
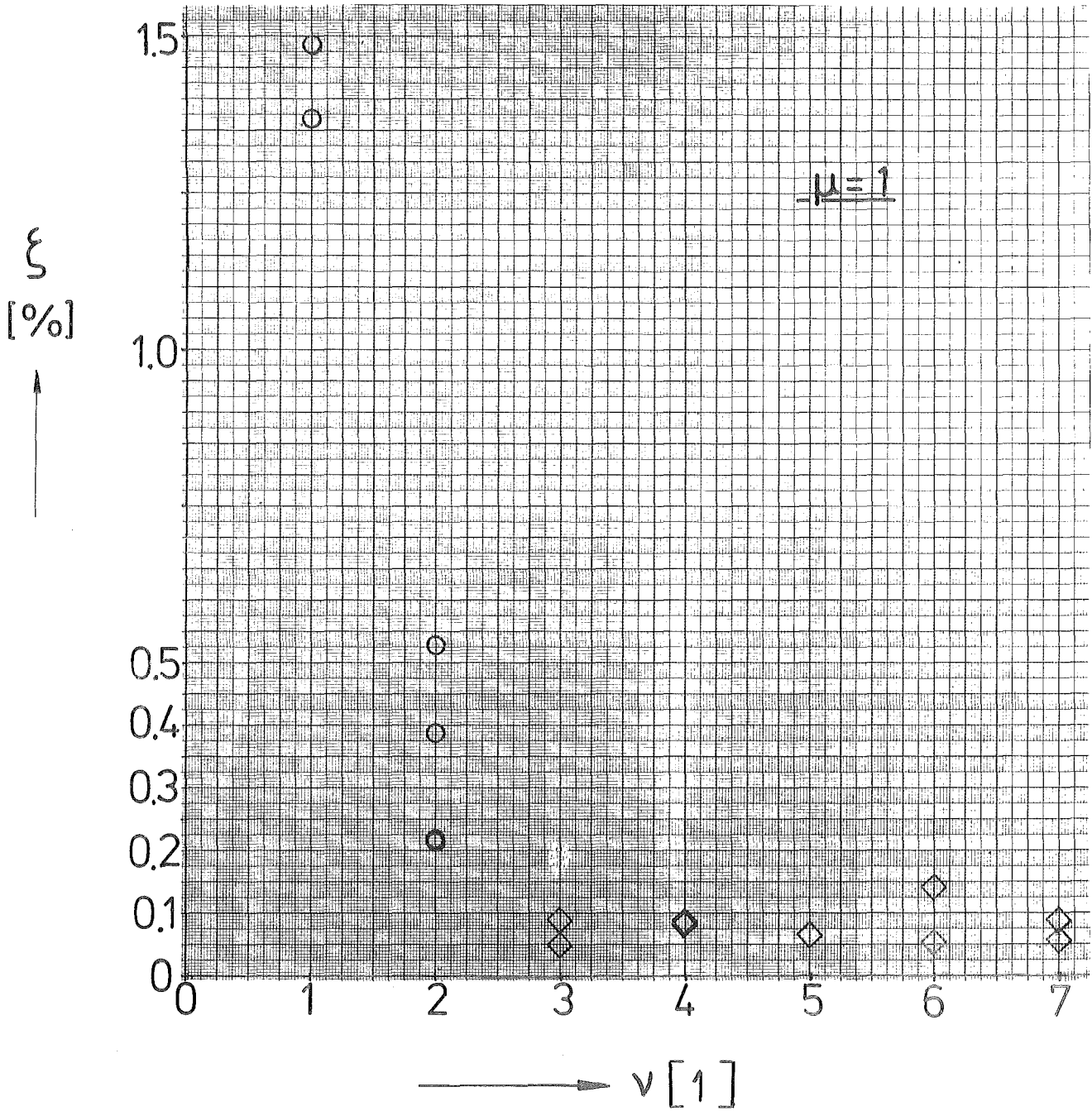


Fig. 16: Comparison of the calculated and measured natural frequencies (tests Nos. V59.1.4 and V59.3.4)



KIKIRE

Fig. 17: Critical damping ratio ξ of extracted modes ($\mu = 1$; tests Nos. V59.1.4 and V59.3.4).

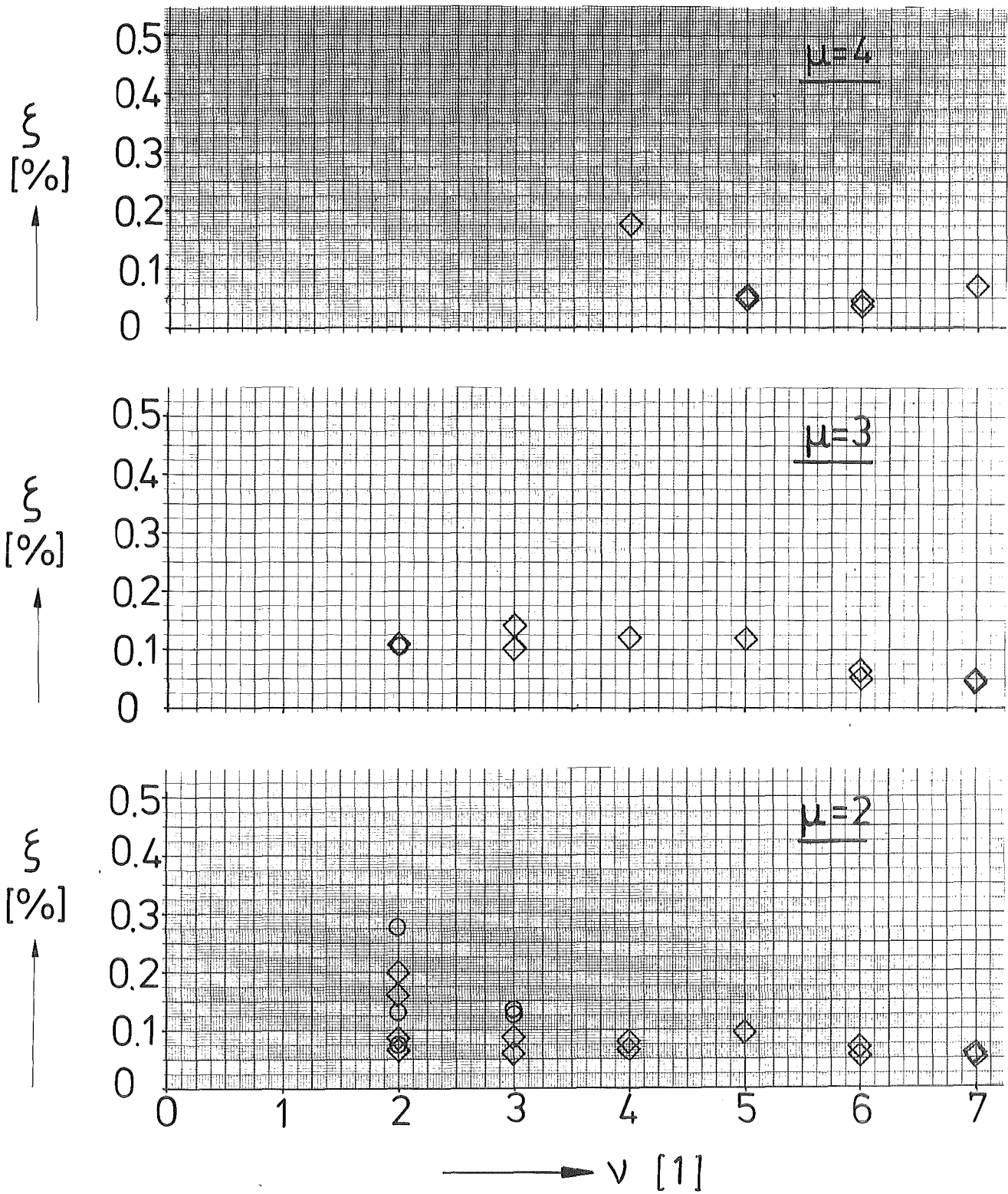


Fig.18: Critical damping ratio ξ of extracted modes ($\mu=2, 3$ and 4 ; tests Nos. V59.1.4 and V59.3.4)

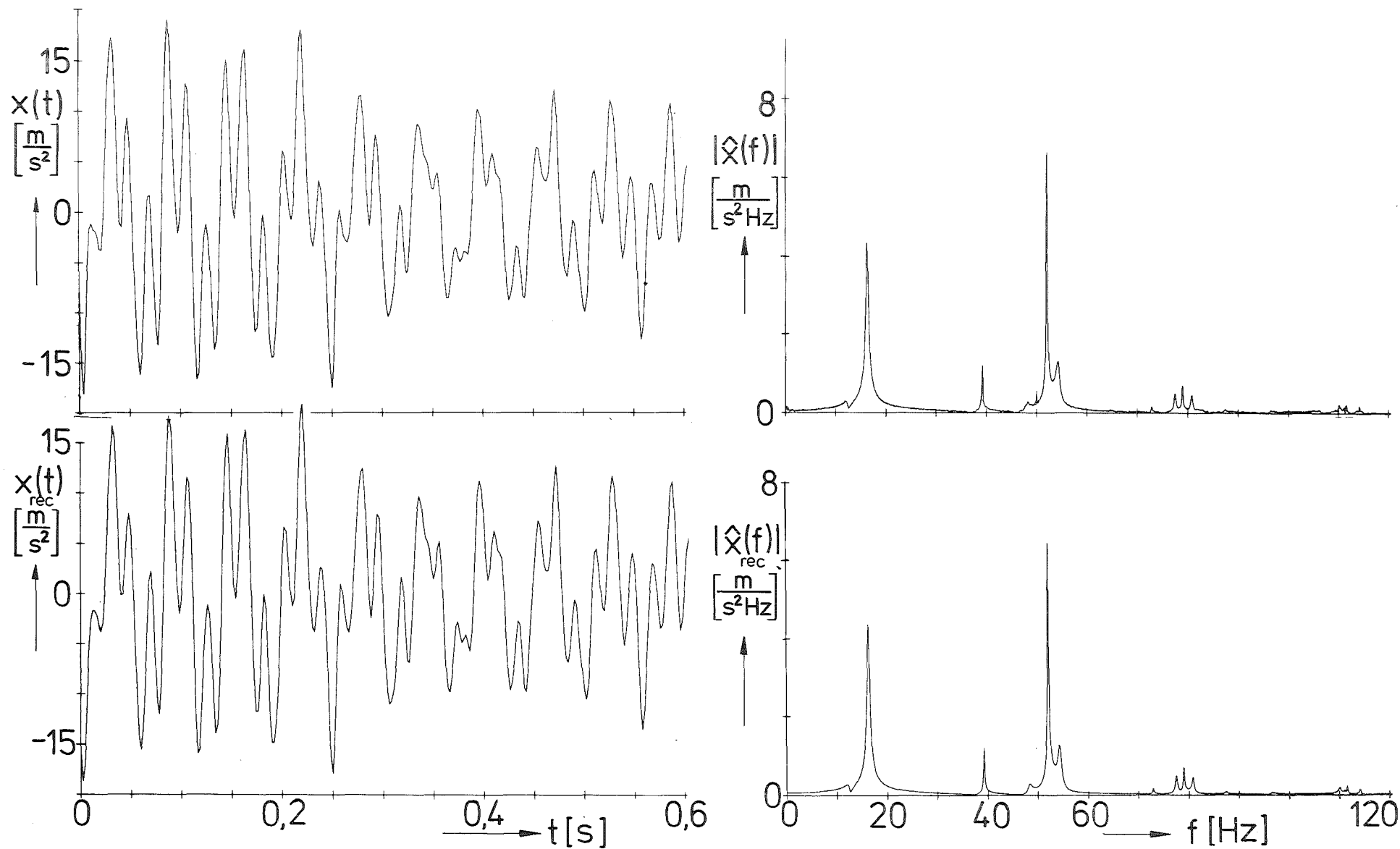


Fig.19 : Comparison of original with reconstructed input signals (test No. V59.1.4 ; accelerometer position KS1206).

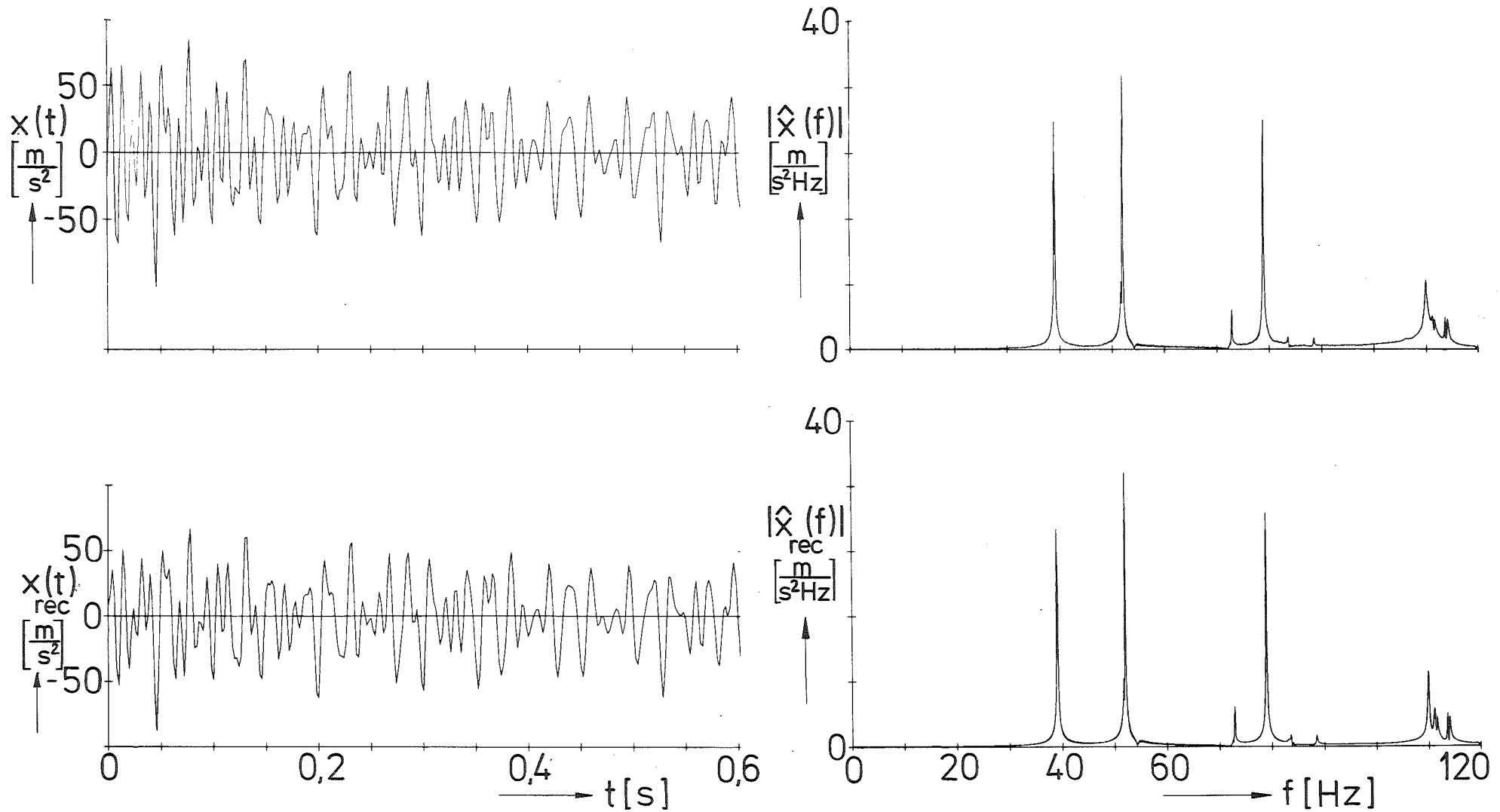


Fig. 20 : Comparison of original with reconstructed input signal (test No. V59.3.4 ; accelerometer position KS1206).

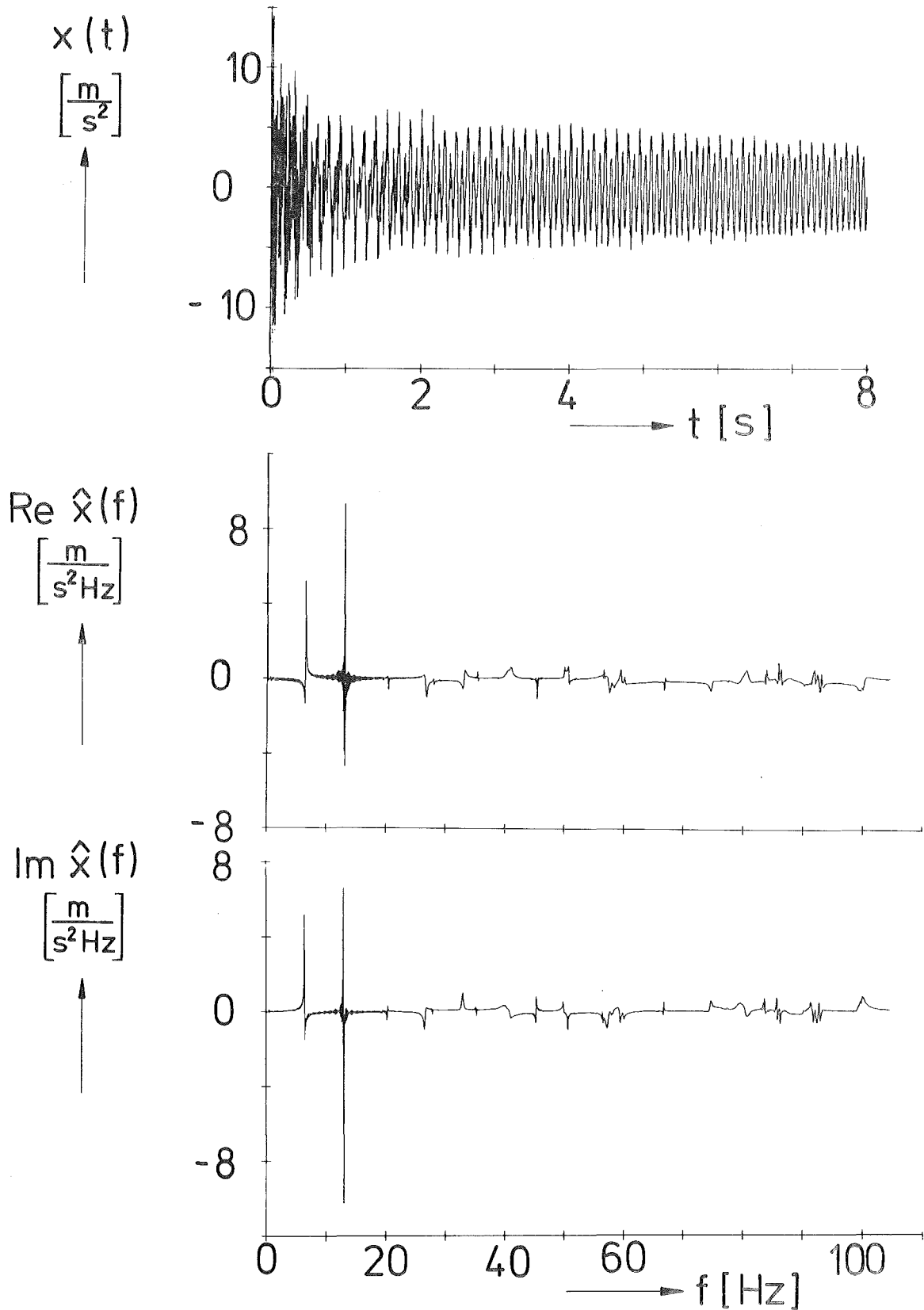


Fig. 21: Typical time history and Fourier-transform of the measured acceleration (KS1206; test No. V59.2.3)

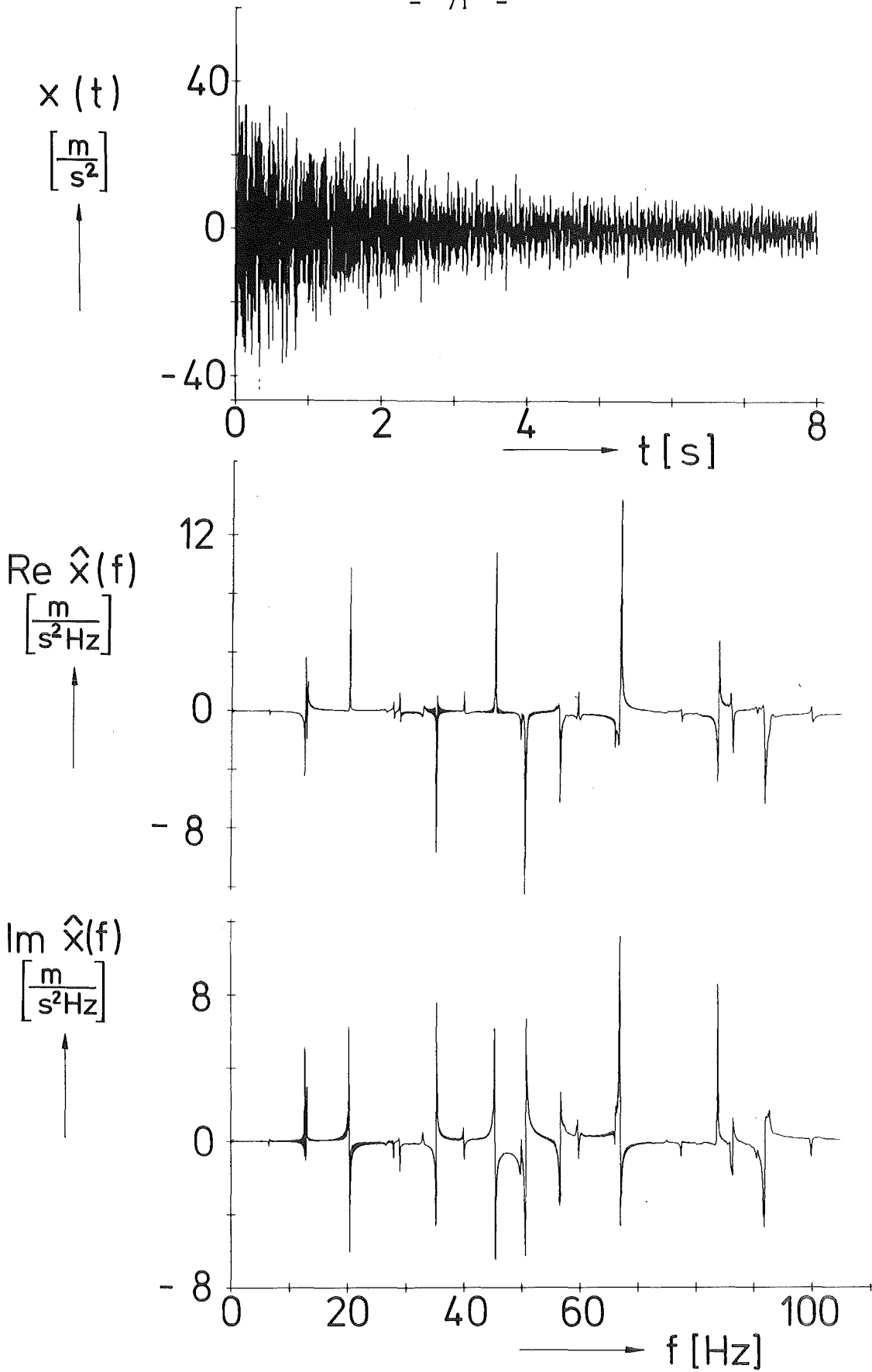


Fig. 22: Typical time history and Fourier-transform of the measured acceleration (KS1206 ; test No. V59.4.3).

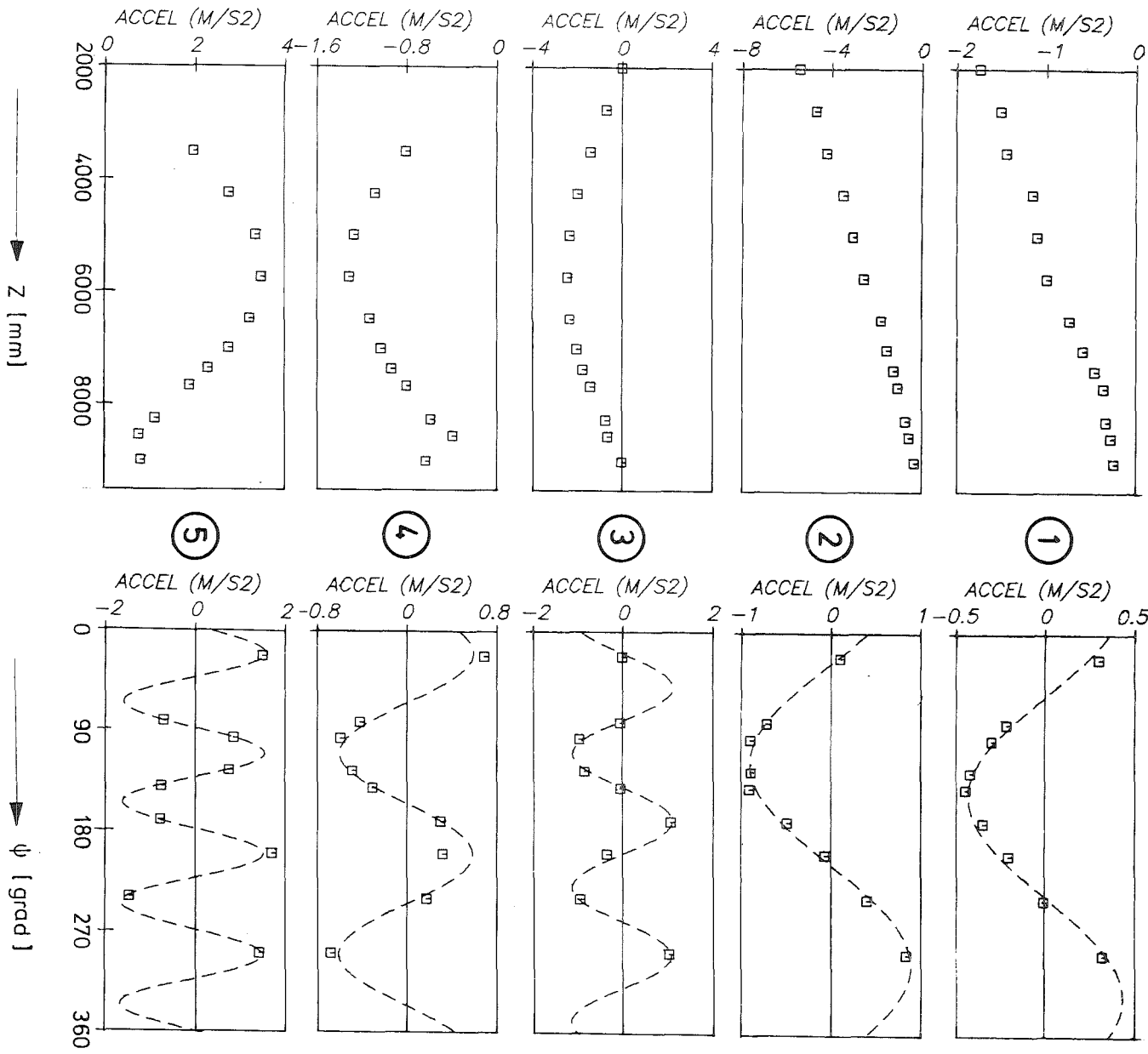


Fig.23: Extracted mode shapes of the core barrel mockup (reactor pressure vessel filled)

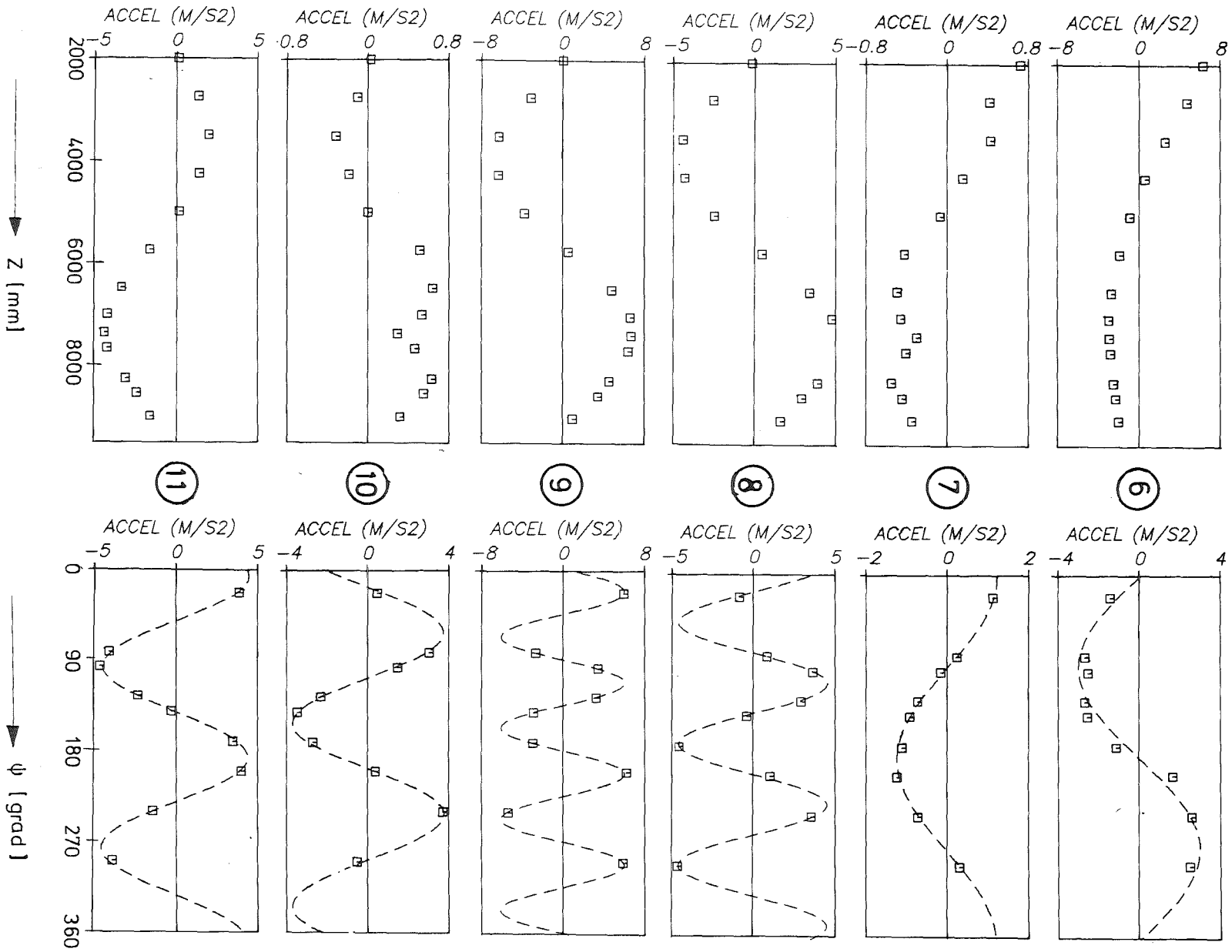


Fig.24: Extracted mode shapes of the core barrel mockup (reactor pressure vessel filled)

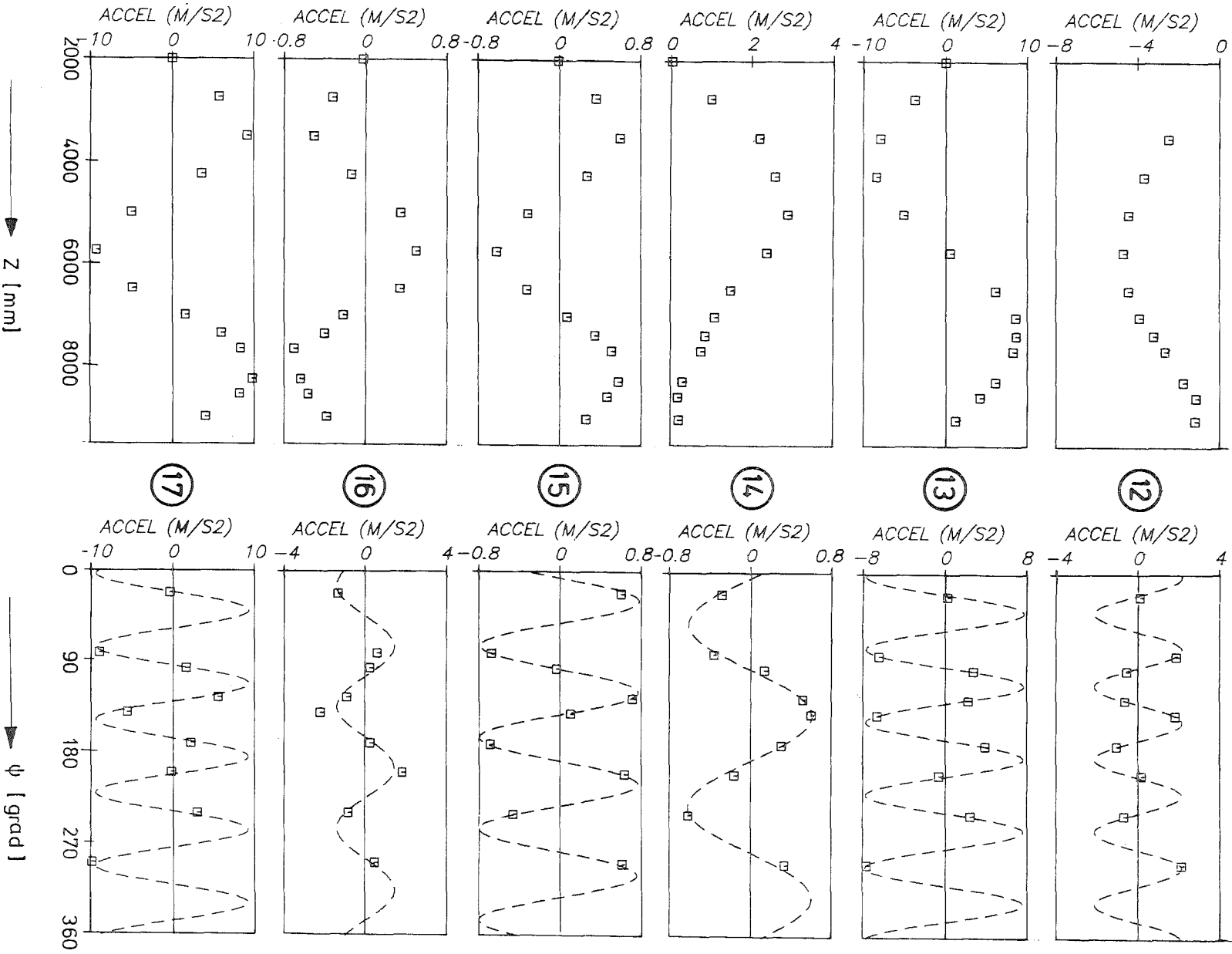


Fig. 25: Extracted mode shapes of the core barrel mockup (reactor pressure vessel filled)



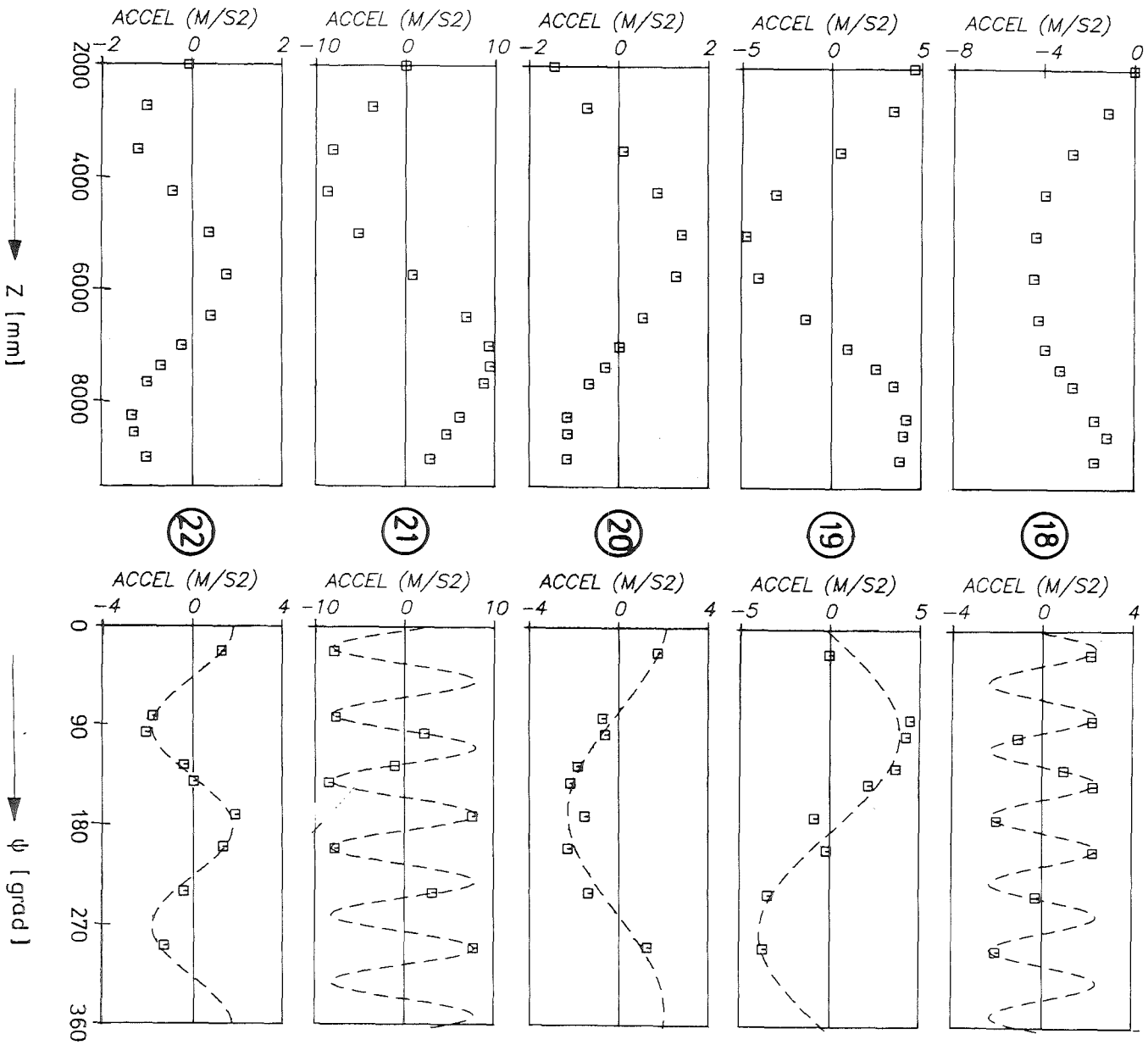


Fig.26: Extracted mode shapes of the core barrel mockup (reactor pressure vessel filled)

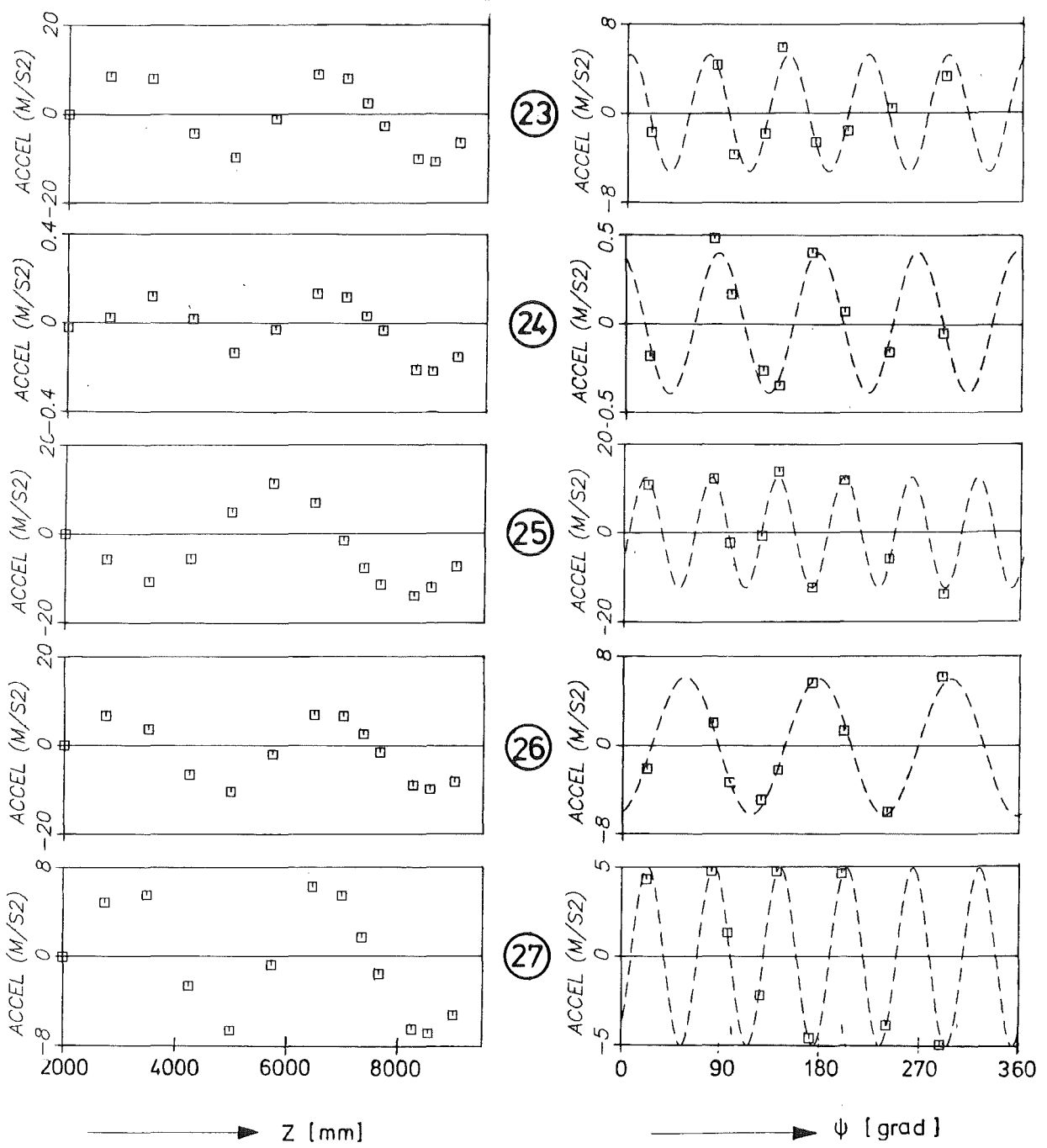


Fig.27: Extracted mode shapes of the core barrel mockup (reactor pressure vessel filled)

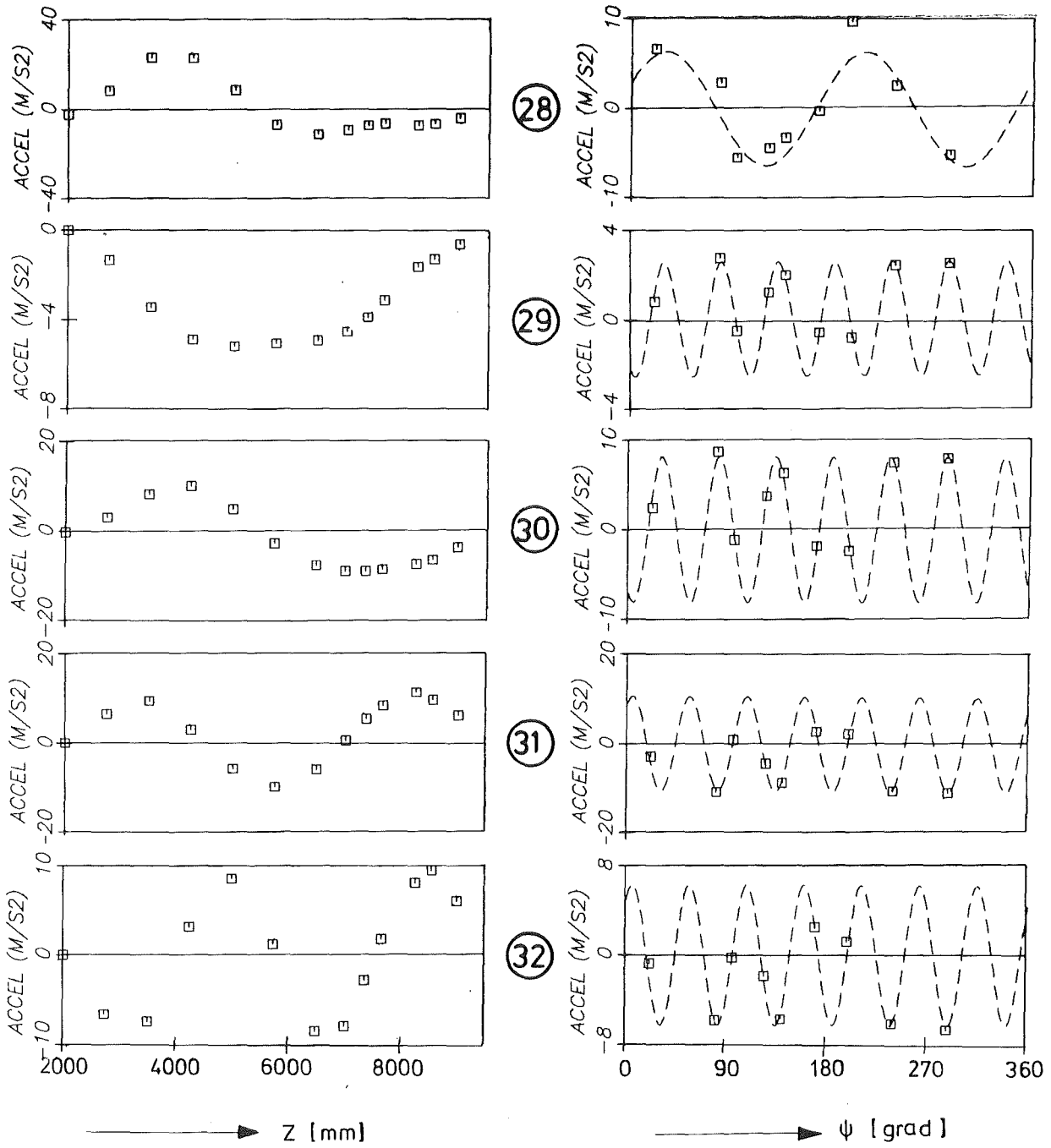


Fig.28: Extracted mode shapes of the core barrel mockup (reactor pressure vessel filled)

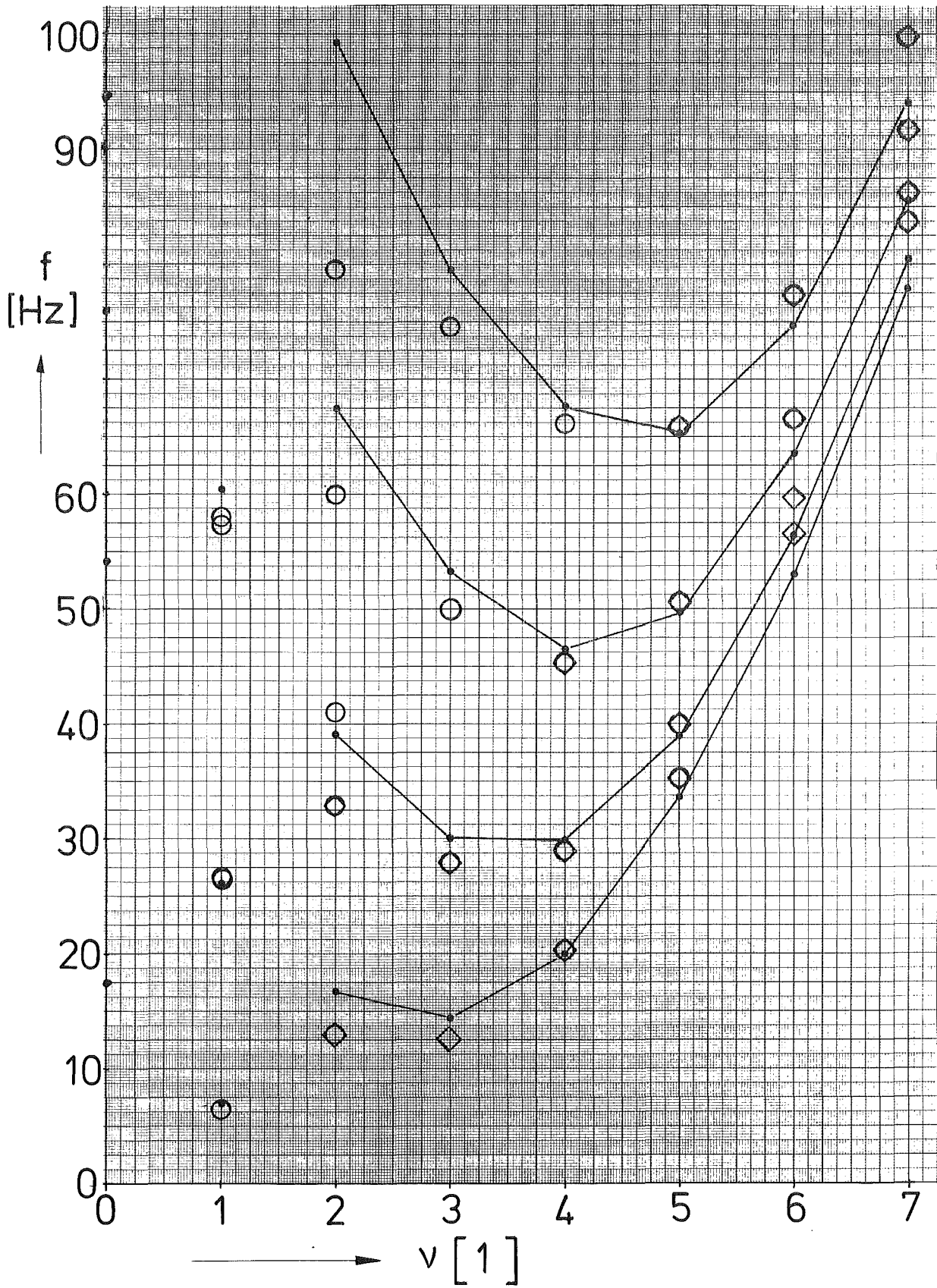


Fig. 29: Comparison of the calculated and measured natural frequencies (snapback tests V59.2.3 and V59.4.3)

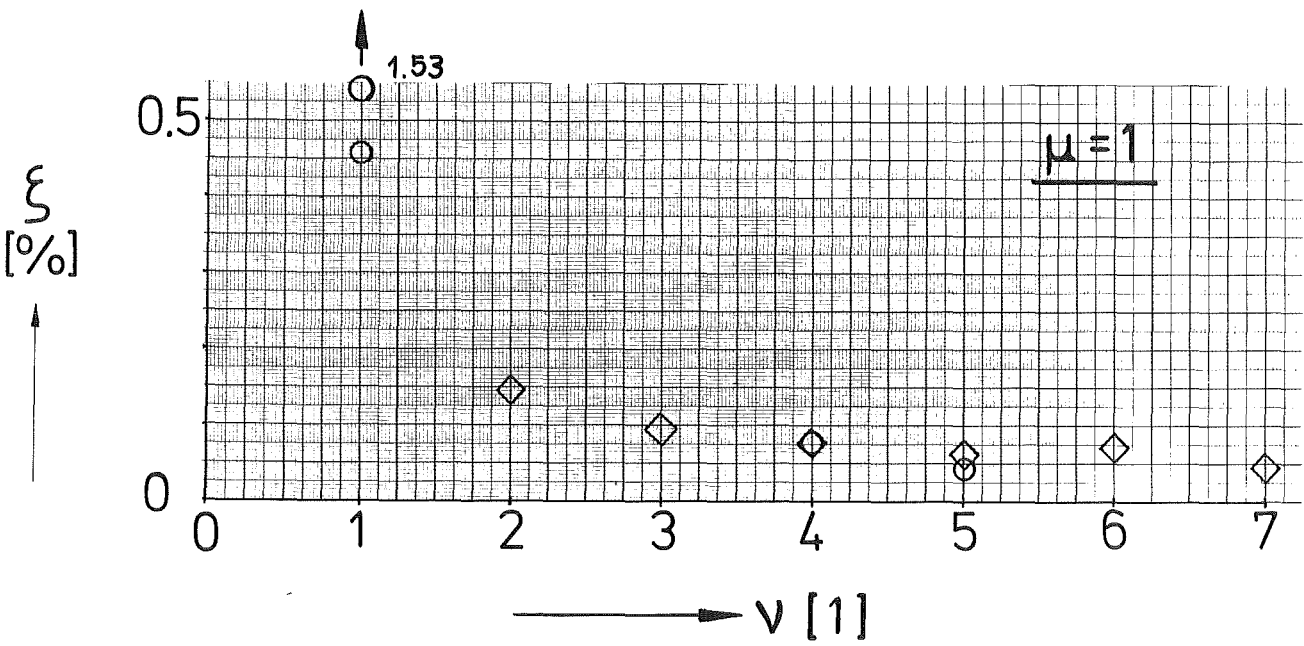
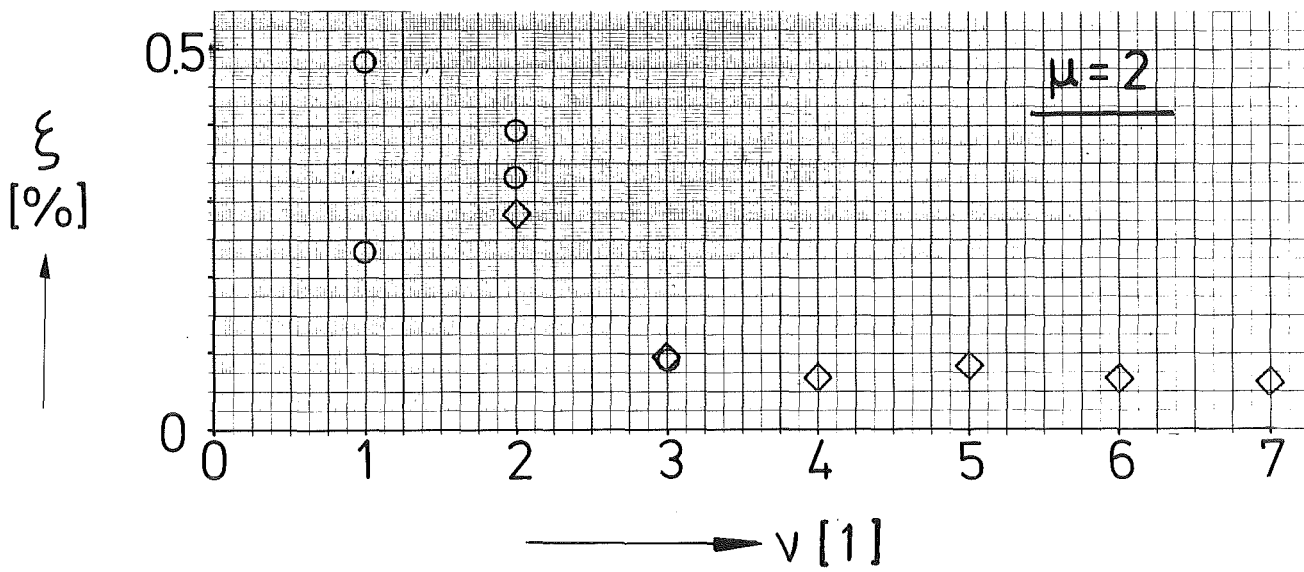


Fig. 30: Critical damping ratio ξ of extracted modes ($\mu=1$ and 2 ; tests Nos. V59.2.3 and V59.4.3)

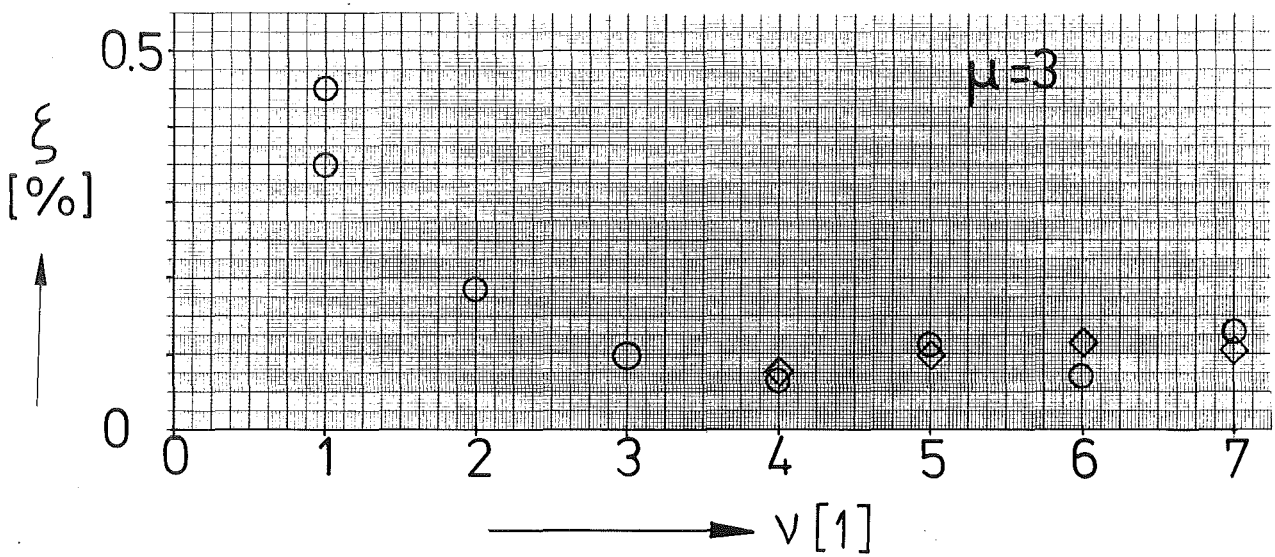
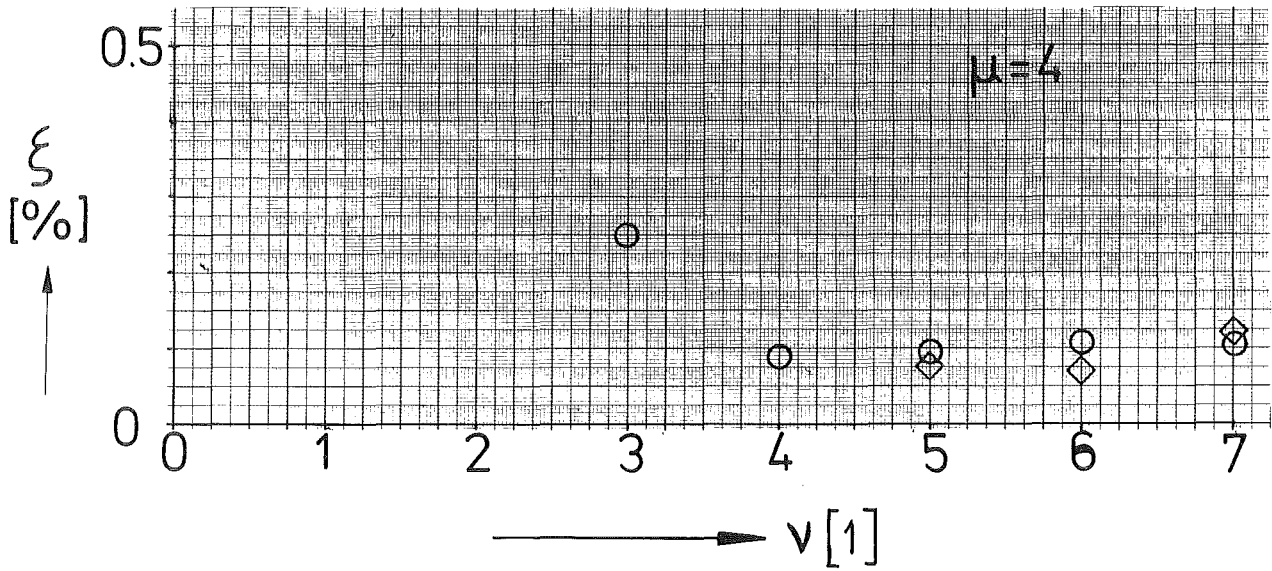


Fig. 31: Critical damping ratio ξ of extracted modes ($\mu = 3$ and 4 ; tests No. V59.2.3 and V59.4.3)

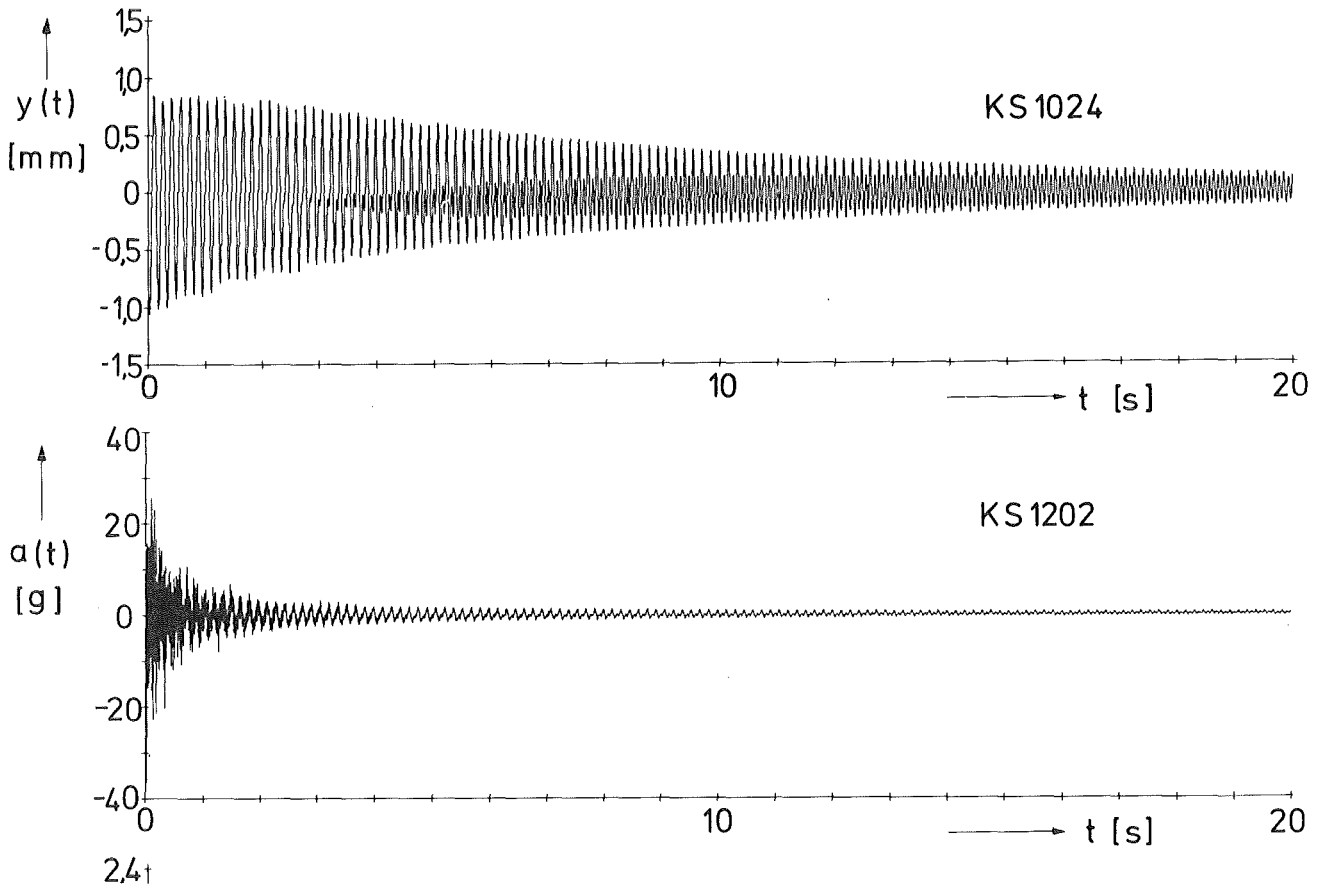
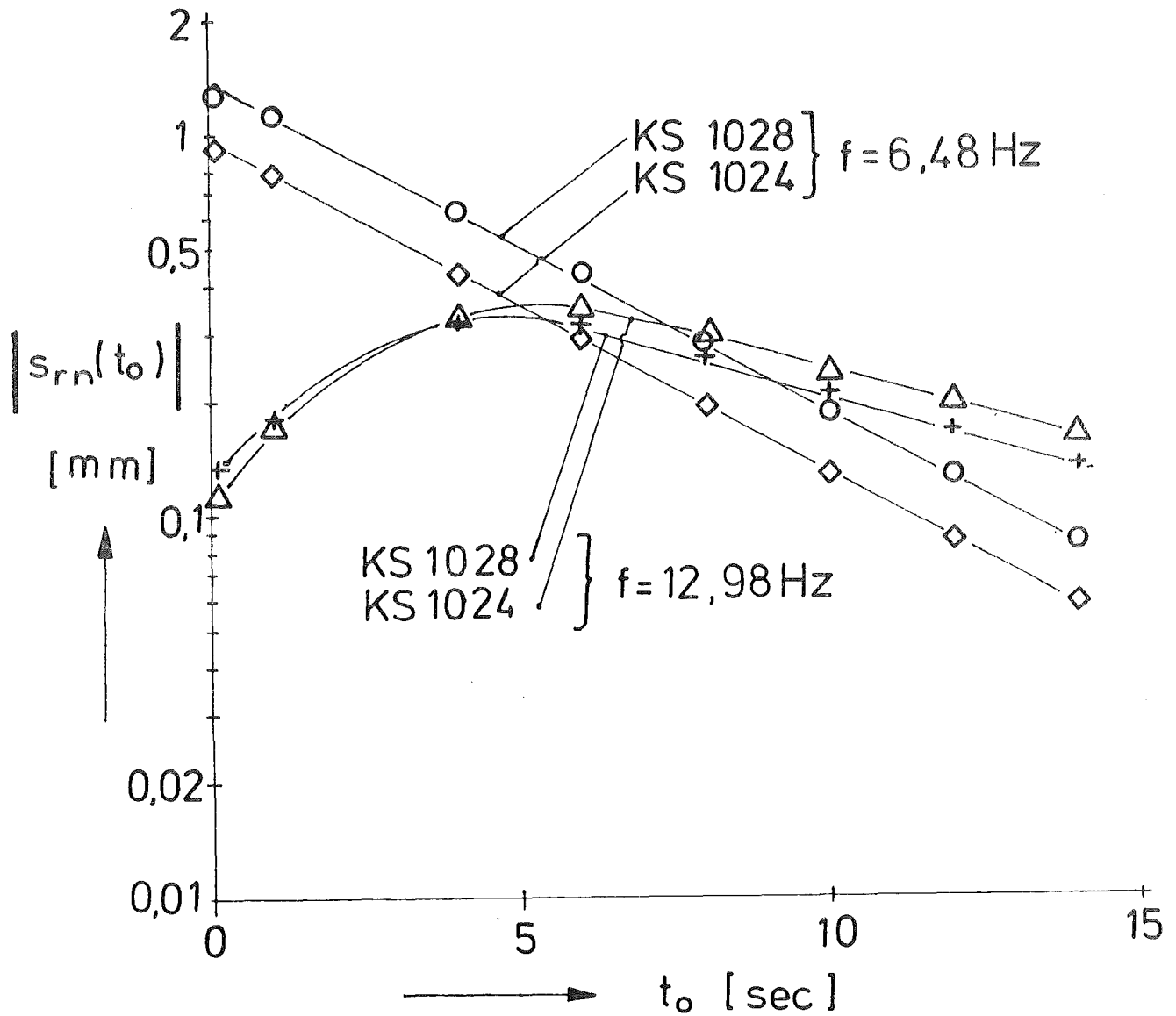


Fig.32: Typical time history plots of the measured displacement and acceleration (test No. V59.2.3 ; RPV filled with water 20 bar , 750 kN deflection device)



KfK

Fig.33: Initial displacement values $|s_{rn}(t_0)|$ (test No. V59.2.3 ; RPV filled with water 20bar, 750kN deflection device)

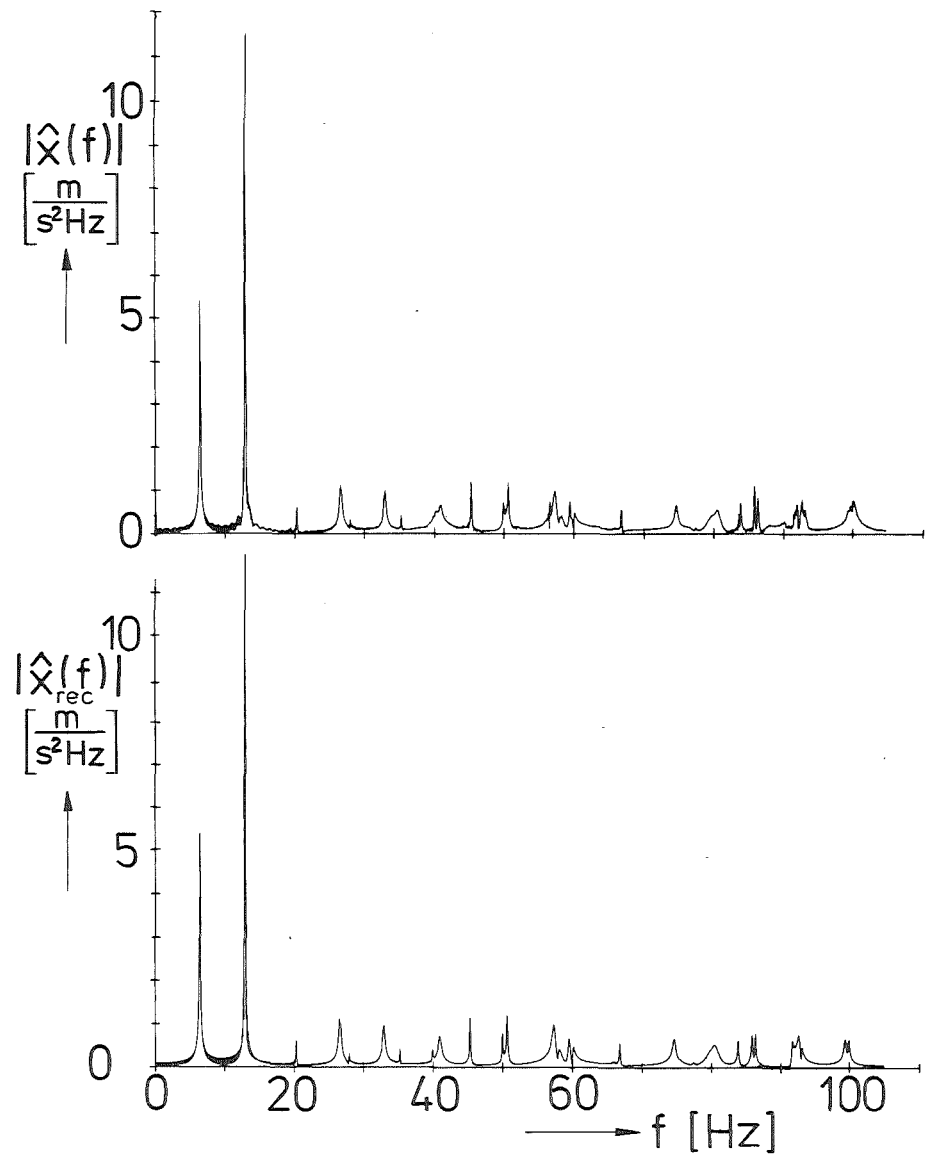
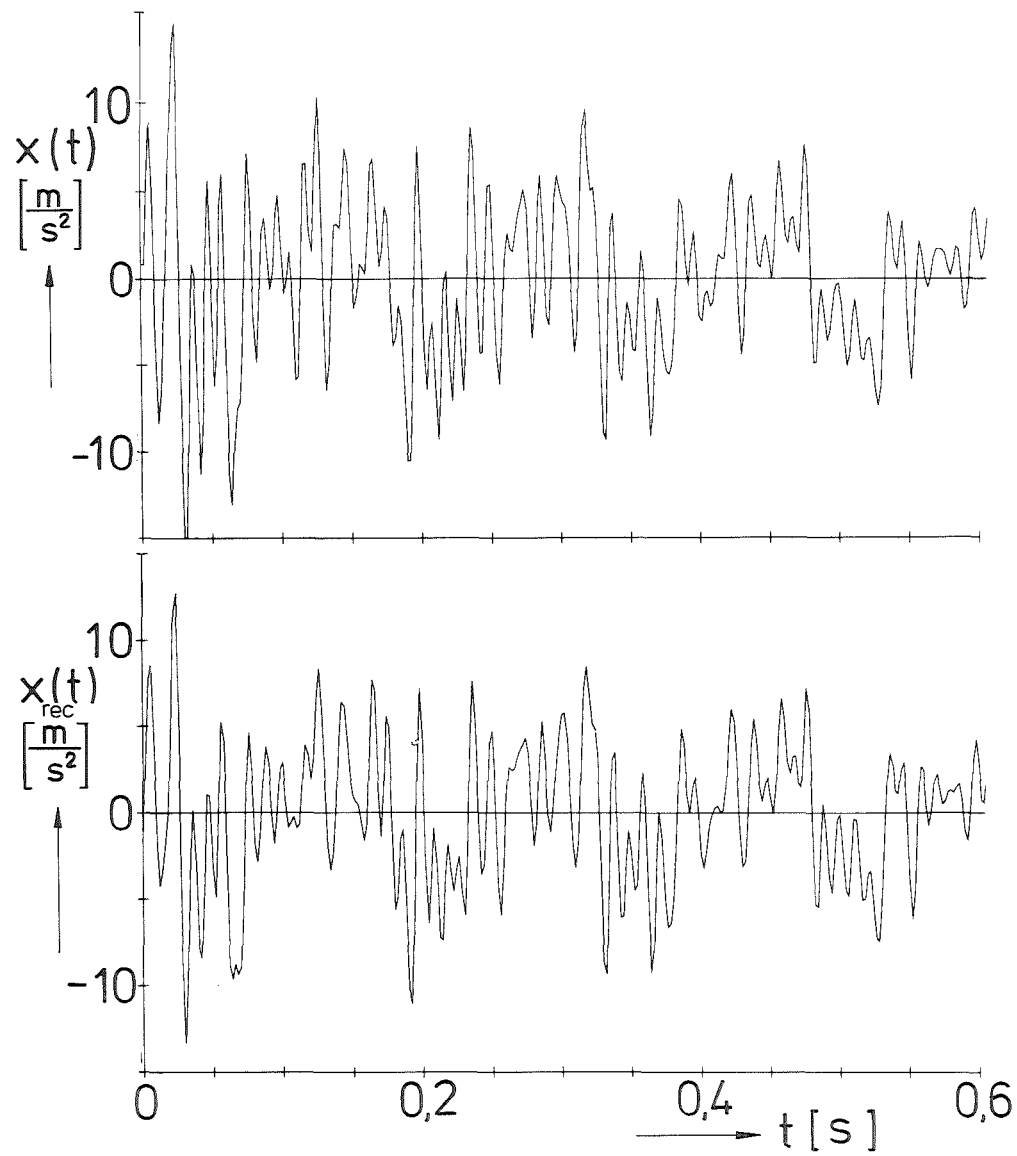
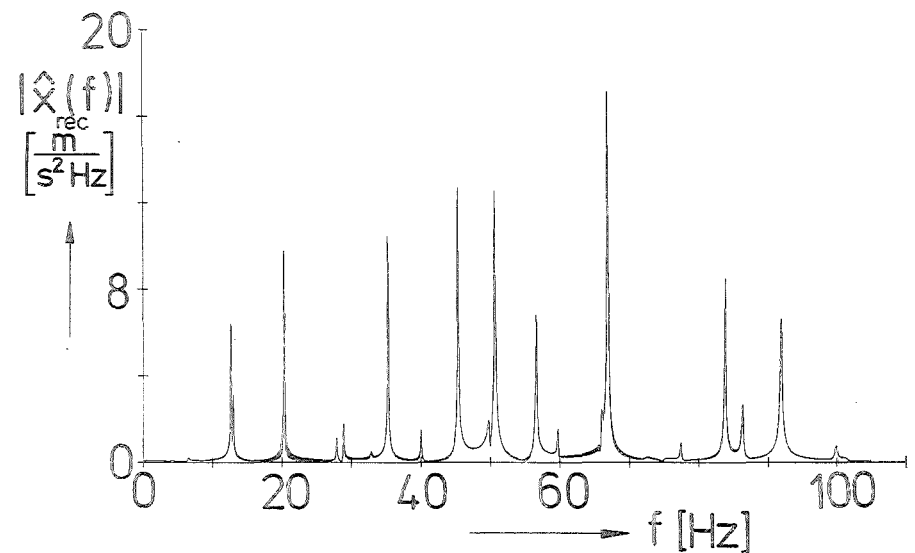
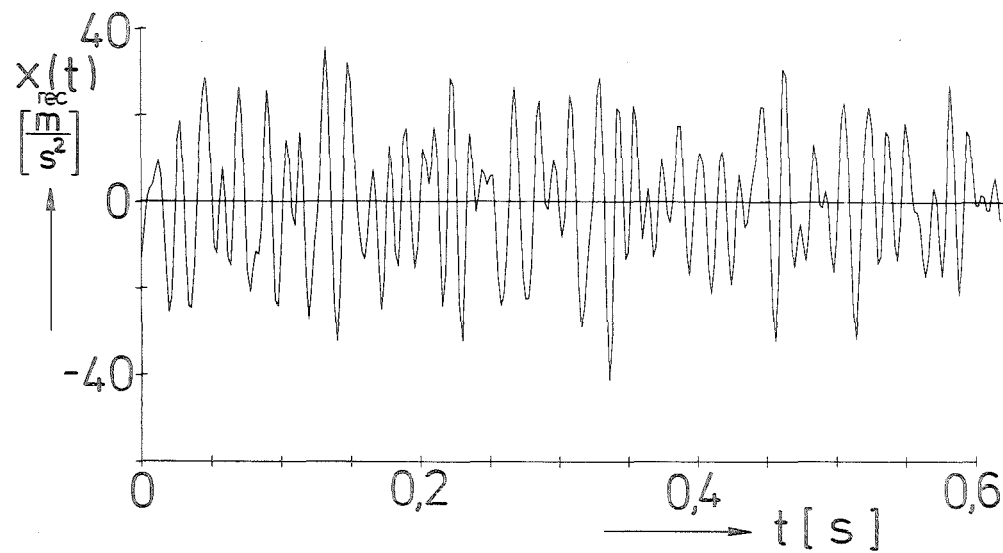
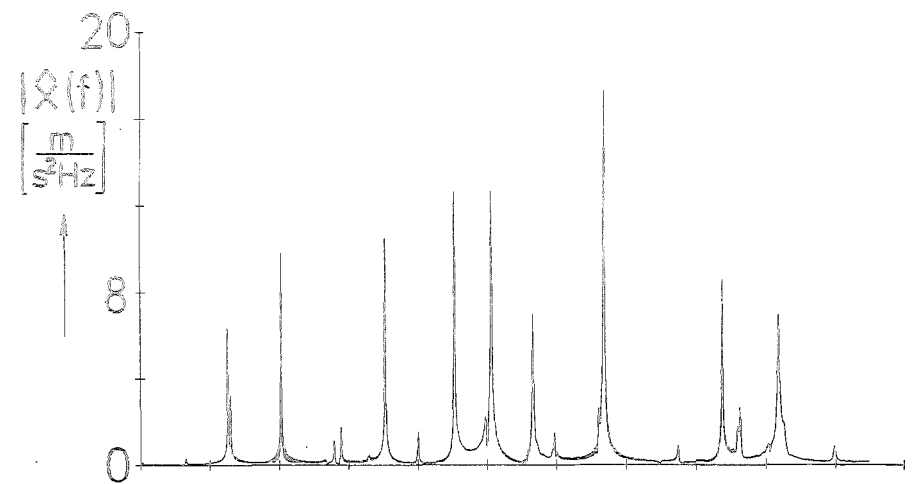
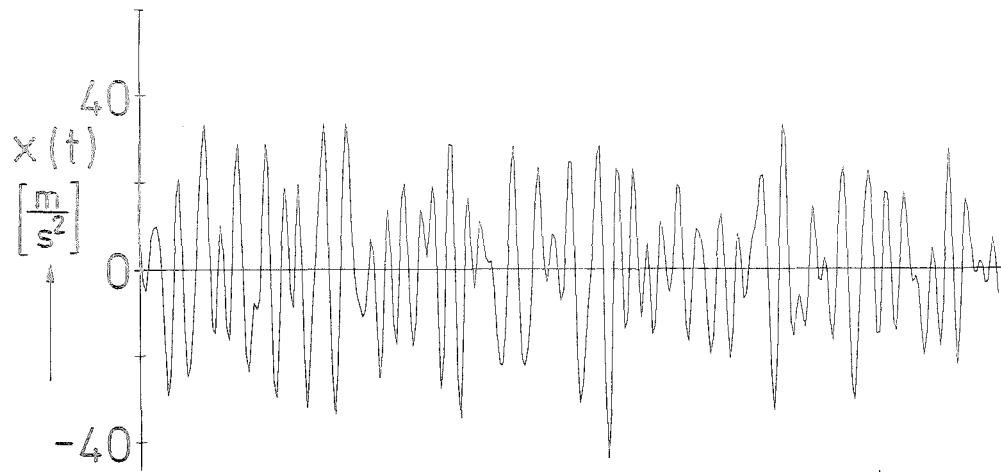


Fig.34: Comparison of original with reconstructed input signal (test No. V59.2.3 , accelerometer position KS1206)



KfK IRE

Fig. 35: Comparison of original with reconstructed input signal (test No. V59.4.3, accelerometer position KS1206)